Evolution of cellular diversity in primary motor cortex of human, marmoset monkey, and mouse

Trygve E. Bakken, Nikolas L. Jorstad, Qiwen Hu, Blue B. Lake, Wei Tian, Brian E. Kalmbach, Megan Crow, Rebecca D. Hodge, Fenna M. Krienen, Staci A. Sorensen, Jeroen Eggermont, Zizhen Yao, Brian D. Aevermann, Andrew I. Aldridge, Anna Bartlett, Darren Bertagnolli, Tamara Casper, Rosa G. Castanon, Kirsten Crichton, Tanya L. Daigle, Rachel Dalley, Nick Dee, Nikolai Dembrow, Dinh Diep, Song-Lin Ding, Weixiu Dong, Rongxin Fang, Stephan Fischer, Melissa Goldman, Jeff Goldy, Lucas T. Graybuck, Brian R. Herb, Xiaomeng Hou, Jayaram Kancherla, Matthew Kroll, Kanan Lathia, Baldur van Lew, Yang Eric Li, Christine S. Liu, Hanqing Liu, Jacinta D. Lucero, Anup Mahurkar, Delissa McMillen, Jeremy A. Miller, Marmar Moussa, Joseph R. Nery, Philip R. Nicovich, Joshua Orvis, Julia K. Osteen, Scott Owen, Carter R. Palmer, Thanh Pham, Nongluk Plongthongkum, Olivier Poirion, Nora M. Reed, Christine Rimorin, Angeline Rivkin, William J. Romanow, Adriana E. Sedeño-Cortés, Kimberly Siletti, Saroja Somasundaram, Josef Sulc, Michael Tieu, Amy Torkelson, Herman Tung, Xinxin Wang, Fangming Xie, Anna Marie Yanny, Renee Zhang, Seth A. Ament, M. Margarita Behrens, Hector Corrada Bravo, Jerold Chun, Alexander Dobin, Jesse Gillis, Ronna Hertzano, Patrick R. Hof, Thomas Höllt, Gregory D. Horwitz, C. Dirk Keene, Peter V. Kharchenko, Andrew L. Ko, Boudewijn P. Lelieveldt, Chongyuan Luo, Eran A. Mukamel, Sebastian Preissl, Aviv Regev, Bing Ren, Richard H. Scheuermann, Kimberly Smith, William J. Spain, Owen R. White, Christof Koch, Michael Hawrylycz, Bosiljka Tasic, Evan Z. Macosko, Steven A. McCarroll, Jonathan T. Ting, Hongkui Zeng, Kun Zhang, Guoping Feng, Joseph R. Ecker, Sten Linnarsson, Ed S. Lein

Correspondence: Ed S. Lein (edl@alleninstitute.org), Trygve E. Bakken (trygveb@alleninstitute.org)

Abstract

The primary motor cortex (M1) is essential for voluntary fine motor control and is functionally conserved across mammals. Using high-throughput transcriptomic and epigenomic profiling of over 450,000 single nuclei in human, marmoset monkey, and mouse, we demonstrate a broadly conserved cellular makeup of this region, whose similarity mirrors evolutionary distance and is consistent between the transcriptome and epigenome. The core conserved molecular identity of neuronal and non-neuronal types allowed the generation of a cross-species consensus cell type classification and inference of conserved cell type properties across species. Despite overall conservation, many species specializations were apparent, including differences in cell type proportions, gene expression, DNA methylation, and chromatin state. Few cell type marker genes were conserved across species, providing a short list of candidate genes and regulatory mechanisms responsible for conserved features of homologous cell types, such as the GABAergic chandelier cells. This consensus transcriptomic classification allowed the Patch-seq identification of layer 5 (L5) corticospinal Betz cells in non-human primate and human and characterization of their highly specialized physiology and anatomy. These findings highlight the robust molecular underpinnings of cell type diversity in M1 across mammals and point to the genes and regulatory pathways responsible for the functional identity of cell types and their species-specific adaptations.

Introduction

Single-cell transcriptomic and epigenomic methods provide a powerful lens on understanding the cellular makeup of highly complex brain tissues based on distinct patterns of gene expression and underlying regulatory mechanisms [1–7]. Applied to mouse and human neocortex, single-cell or single-nucleus transcriptomic analysis has yielded a complex but finite classification of cell types with approximately 100 discriminable neuronal and non-neuronal types in any given neocortical region [1,2,6,8]. Similar analyses using epigenomic methods have shown that many cortical cell types can be

49 distinguished on the basis of regions of open chromatin or DNA methylation [5,9,10]. Furthermore, several
50 recent studies have shown that transcriptomically-defined cell types can be aligned across species [2,11–
51 13], indicating that these methods provide a path to quantitatively study evolutionary conservation and
52 divergence at the level of cell types. However, application of these methods has been highly
53 fragmented to date. Human and mouse comparisons have been performed in different cortical regions,
54 using single-cell (with biases in cell proportions) versus single-nucleus (with biases in transcript
55 makeup) analysis, and most single-cell transcriptomic and epigenomic studies have been performed
56 independently.
57
58 The primary motor cortex (MOp in mouse, M1 in human and non-human primates, all referred to as M1
59 herein) provides an ideal cortical region to address questions about cellular evolution in rodents and
60 primates by integrating these approaches. Unlike the primary visual cortex (V1), which is highly
61 specialized in primates, or frontal and temporal association areas, whose homologues in rodents
62 remain poorly defined, M1 is essential for fine motor control and is functionally conserved across
63 placental mammals. M1 is an agranular cortex, lacking a defined L4, although neurons with L4-like
64 properties have been described [14]. L5 of carnivore and primate M1 contains exceptionally large
65 “giganto-cellular” corticospinal neurons (Betz cells in primates [15,16] that contribute to the pyramidal tract
66 and are highly specialized for their unusually large size with distinctive “taproot”-style dendrites [17,18].
67 Extracellular recordings from macaque corticospinal neurons reveal distinctive action potential
68 properties supportive of a high conduction velocity and similar, unique properties have been reported
69 during intracellular recordings from giganto-cellular neurons in cats[19–21]. Additionally, some primate Betz
70 cells directly synapse onto alpha motor neurons, whereas in cats and rodents these neurons synapse
71 instead onto spinal interneurons [22,23]. These observations suggest that Betz cells possess specialized
72 intrinsic mechanisms to support rapid communication, some of which are primate specific.
73

Conservation of cellular features across species is strong evidence for evolutionary constraints on important cellular function. To explore evolutionary conservation and divergence of the M1 cellular makeup and its underlying molecular and gene regulatory mechanisms, we combined saturation coverage single-nucleus transcriptome analysis, DNA methylation, and combined open chromatin and transcriptome analysis of mouse, marmoset, and human M1 and transcriptomic profiling of macaque M1 L5. We describe a robust classification of neuronal and non-neuronal cell types in each species that is highly consistent between the transcriptome and epigenome. Cell type alignment accuracy and similarity varied as a function of evolutionary distance, with human more similar to non-human primate than to mouse. We derived a consensus mammalian classification with globally similar cellular diversity, varying proportions, and species specializations in gene expression between conserved cell classes. Few genes had conserved cell type-specific expression across species and likely contribute to other conserved cellular properties, such as the unique morphology of chandelier GABAergic neurons. Conversely, these data also allow a targeted search for genes responsible for species specializations such as the distinctive anatomy, physiology and axonal projections of Betz cells, large corticospinal neurons in primates that are responsible for voluntary fine motor control. Together these findings highlight the strength of a comparative approach to understand cortical cellular diversity and identify conserved and specialized gene and gene regulatory mechanisms underlying cellular identity and function.

We made all primary and analyzed data publicly available. Raw sequence data are available for download from the Neuroscience Multi-omics Archive (nemoarchive.org) and the Brain Cell Data Center (biccn.org/data). Visualization and analysis tools are available at NeMO Analytics (nemoanalytics.org) and Cytosplore Viewer (viewer.cytosplore.org). These tools allow users to compare cross-species datasets and consensus clusters via genome and cell browsers and calculate differential expression within and among species. A semantic representation of the cell types defined through

these studies is available in the provisional Cell Ontology (https://bioportal.bioontology.org/ontologies/PCL; Supplementary Table 1).

Results

Multi-omic cell type taxonomies

To characterize the molecular diversity of M1 neurons and non-neuronal cells, we applied multiple single-nucleus transcriptomic (plate-based SMART-seq v4, SSv4, and droplet-based Chromium v3, Cv3, RNA-sequencing) and epigenomic (single-nucleus methylcytosine sequencing 2, snmC-seq2; single-nucleus chromatin accessibility and mRNA expression sequencing, SNARE-seq2) assays on isolated M1 samples from human (Extended Data Fig. 1a), marmoset, and mouse brain. Cellular diversity was also profiled selectively in M1 L5 from macaque monkeys using Cv3 (Fig. 1b) to allow Patch-seq mapping in physiology experiments. M1 was identified in each species based on its stereotyped location in the caudal portion of frontal cortex and histological features such as the presence of exceptionally large pyramidal neurons in L5 of M1, classically known as Betz cells in human, other primates, and carnivores (Fig. 1a; [17]). Single nuclei were dissociated, sorted, and transcripts were quantified with Cv3 for deep sampling in all four species, and additionally using SSv4 in human and mouse for full-length transcript information. For human and a subset of mouse nuclei, individual layers of M1 were profiled independently using SSv4. Whole-genome DNA methylation, and open chromatin combined with transcriptome measurements, were quantified in single nuclei from a subset of species (Fig. 1b). Mouse datasets are also reported in a companion paper [6]. Median neuronal gene detection was higher in human using SSv4 (7296 genes) than Cv3 (5657), partially due to 20-fold greater read depth, and detection was lower in marmoset (4211) and mouse (5046) using Cv3 (Extended Data Fig. 1b-i).

123 For each species, a diverse set of neuronal and non-neuronal cell type clusters were defined based on
124 unsupervised clustering of snRNA-seq datasets (cluster metadata in Supplementary Table 2). Human
125 SSv4 and Cv3 data were integrated based on shared co-expression using Seurat [24], and 127 clusters
126 were identified that included nuclei from both RNA-seq platforms (Extended Data Fig. j-l). Marmoset
127 clusters (94) were determined based on independent clustering of Cv3 data using a similar analysis
128 pipeline. Mouse clusters (116) were defined in a companion paper [6] using seven integrated
129 transcriptomics datasets. These differences in the number of clusters are likely due to a combination of
130 statistical methodological differences as well as sampling and data quality differences rather than true
131 biological differences in cell diversity. For example, more non-neuronal nuclei were sampled in mouse
132 (58,098) and marmoset (21,189) compared to human (4,005), resulting in greater non-neuronal
133 resolution in those species. t-SNE visualizations of transcriptomic similarities across nuclei revealed
134 well-separated clusters in all species and mixing among donors, with some donor-specific technical
135 effects in marmoset (Extended Data Fig. 1m,n).
136
137 Post-clustering, cell types were organized into taxonomies based on transcriptomic similarities and
138 given a standardized nomenclature (Supplementary Table 3). As described previously for a different
139 cortical region [2], taxonomies were broadly conserved across species and reflected different
140 developmental origins of major non-neuronal and neuronal classes (e.g. GABAergic neurons from
141 ganglionic eminences (GEs) versus glutamatergic neurons from the cortical plate) and subclasses (e.g.
142 GABAergic CGE-derived *Lamp5/Sncg* and *Vip* versus MGE-derived *Pvalb* and *Sst*), allowing
143 identification and naming of these subclasses across species. Consequently, cardinal cell subclass
144 properties can be inferred, such as intratelencephalic (IT) projection patterns. Greater species variation
145 was seen at the highest level of resolution (cell types) that are named based on transcription data in
146 each species including the layer (if available), major class, subclass marker gene, and most specific
147 marker gene (e.g. L3 Exc *RORB OTOGL* in human; additional markers in Supplementary Tables 4-6).
148 GABAergic types were uniformly rare (< 4.5% of neurons), whereas more variable frequencies were

149 found for glutamatergic types (0.01 to 18.4% of neurons) and non-neuronal types (0.15% to 56.2% of
150 non-neuronal cells).
151
152 Laminar dissections in human M1 further allowed the estimation of laminar distributions of cell types
153 based on the proportions of nuclei dissected from each layer (Fig. 1c). As expected and previously
154 reported in middle temporal gyrus (MTG) of human neocortex [2], glutamatergic neuron types were
155 specific to layers. A subset of CGE-derived *Lamp5/Sncg* GABAergic neurons were restricted to L1, and
156 MGE-derived GABAergic types (*Sst* and *Pvalb*) displayed laminar patterning, with transcriptomically
157 similar types showing proximal laminar distributions, whereas *Vip* GABAergic neuron types displayed
158 the least laminar specificity. Three astrocyte subtypes had frequencies and layer distributions that
159 correlated with known morphologically-defined astrocyte types [25], including a common type in all layers
160 (protoplasmic), a rare type in L1 (interlaminar) [26], and a rare type in L6 (fibrous).
161
162 Single-nucleus sampling provides a relatively unbiased survey of cellular diversity [2,27] and enables
163 comparison of cell subclass proportions across species. For each donor, we estimated the proportion of
164 GABAergic and glutamatergic cells among all neurons and compared the proportions across species.
165 Consistent with previously reported differences in GABAergic neuron frequencies in primate versus
166 rodent somato-motor cortex based on histological measurements (reviewed in [28]), we found twice as
167 many GABAergic neurons in human (33%) compared to mouse M1 (16%) an intermediate proportion
168 (23%) in marmoset (Fig. 1f). Despite these differences, the relative proportions of GABAergic neuron
169 subclasses were similar. Exceptions to this included an increased proportion of *Vip* and *Sncg* cells and
170 decreased proportion of *Pvalb* cells in marmoset. Among glutamatergic neurons, there were
171 significantly more L2 and L3 IT neurons in human than marmoset and mouse (Fig. 1f), consistent with
172 the dramatic expansion of supragranular cortical layers in human (Fig. 1a) [29]. The L5
173 extratelencephalic-projecting (ET) types (also known as pyramidal tract, PT, or subcerebral types),
174 including corticospinal neurons and Betz cells in primate M1, comprised a significantly smaller

175 proportion of glutamatergic neurons in primates than mouse. This species difference was also reported
176 in MTG [2], possibly reflecting the spatial dilution of these cells with the expansion of neocortex in
177 primates. Similarly, the L6 cortico-thalamic (CT) neuron populations were less than half as frequent in
178 primates compared to mouse, whereas the L6 *Car3* type was rare in all species and relatively more
179 abundant in marmoset.
180
181 Individual nuclei were isolated from M1 of the same donors for each species and molecular profiles
182 were derived for DNA methylation (snmC-seq2) and open chromatin combined with mRNA (SNARE-
183 seq2). Independent unsupervised clustering of epigenomic data also resulted in diverse clusters (see
184 below, Figs. 4 and 5) that were mapped back to RNA clusters based on shared (directly measured or
185 inferred) marker gene expression. Cell epigenomes were highly correlated with transcriptomes, and all
186 epigenomic clusters mapped to one or more transcriptomic clusters. The epigenome data generally had
187 lower cell type resolution (Fig. 1c-e), although this may be due to sampling fewer cells or sparse
188 genomic coverage. Interestingly, snmC-seq2 and SNARE-seq2 resolved different granularities of cell
189 types. For example, more GABAergic *Vip* neuron types were identified in human M1 based on DNA-
190 methylation than open chromatin, despite profiling only 5% as many nuclei with snmC-seq2 (Fig. 1c).
191
192 **Consensus cellular M1 taxonomy across species**
193 A consensus cell type classification identifies conserved molecular makeup and allows direct cross-
194 species comparisons. The snRNA-seq Cv3 datasets were integrated using Seurat [24] that aligns nuclei
195 across species based on shared co-expression of a subset of orthologous genes with variable
196 expression. We repeated this analysis for three cell classes: GABAergic neurons (Fig. 2), glutamatergic
197 neurons (Extended Data Fig. 3) and non-neuronal cells (Extended Data Fig. 4). As represented in a
198 reduced dimension UMAP space (Fig.2a), GABAergic neuronal nuclei were well-mixed across species.
199 Eight well-defined populations formed distinct islands populated by cells from all three species,
200 including CGE-derived (*Lamp5*, *Sncg*, *Vip*) and MGE-derived (*Pvalb*, *Sst*, *Sst Chodl*) subclasses, and

201 *Lamp5 Lhx6* and chandelier cell (ChC) types. To identify conserved molecular expression for each
202 subclass across species, we first identified genes that were enriched in each subclass ("markers")
203 compared to all GABAergic neurons in each species (ROC test; AUC > 0.7). Then, we looked for
204 overlap among these genes across species. Each subclass had a core set of conserved markers (Fig.
205 2b, markers listed in Supplementary Table 7), and many subclass markers were species-specific. The
206 contrast between a minority of conserved and majority of species-specific marker genes enriched in
207 subclasses is particularly clear in the heatmap in Figure 2c (Supplementary Table 8). As expected
208 based on their closer evolutionary distance, human and marmoset shared more subclass markers with
209 each other than with mouse (Fig. 2b).
210
211 Cell types remained distinct within species and aligned across species in the integrated transcriptomic
212 space (Fig. 2d). To establish a consensus taxonomy of cross-species clusters, we used unsupervised
213 clustering to split the integrated space into more than 500 small clusters ('metacells') and built a
214 dendrogram and quantified branch stability by subsampling metacells and reclustering (Extended Data
215 Fig. 2a). Metacells were merged with nearest neighbors until all branches were stable and included
216 nuclei from the three species (see Methods). We used cluster overlap heatmaps to visualize the
217 alignment of cell types across species based on membership in merged metacells (Fig. 2e). 24
218 GABAergic consensus clusters displayed consistent overlap of clusters among the three species and
219 are highlighted as blue boxes in the heatmaps (Fig. 2e).
220
221 We next constructed a consensus taxonomy by pruning the metacell dendrogram (Extended Data Fig.
222 2a), and demonstrated that all types were well mixed across species (Fig. 2f, grey branches). The
223 robustness of consensus types was bolstered by a conserved set of marker genes (Extended Data Fig.
224 2d) and high classification accuracy of subclasses (Extended Data Fig. 2e, data in Supplementary
225 Table 9) and types (Extended Data Fig. 2f, data in Supplementary Table 9) compared to nearest
226 neighbors within and among species using a MetaNeighbor analysis [30]. Distinct consensus types (ChC,

227 *Sst Chodl*) were the most robust (mean AUROC = 0.99 within-species and 0.88 cross-species), while
228 *Sncg* and *Sst* types could not be as reliably differentiated from closely related types (mean AUROC =
229 0.84 within-species and 0.50 cross-species). Most consensus GABAergic types were enriched in the
230 same layers in human and mouse (Fig. 2f), although there were also notable species differences. For
231 example, ChCs were enriched in L2/3 in mouse and distributed across all layers in human as was seen
232 in temporal cortex (MTG) based on RNA ISH [2]. *Sst Chodl* was restricted to L6 in mouse and also found
233 in L1 and L2 in human, consistent with previous observations of sparse expression of *SST* in L1 in
234 human not mouse cortex [31].
235
236 More consensus clusters could be resolved by pairwise alignment of human and marmoset than
237 primates and mouse, particularly *Vip* subtypes (Fig. 2g, Extended Data Fig. 2b). Higher resolution
238 integration of cell types was also apparent in cluster overlap plots between human and marmoset
239 clusters (Fig. 2e, Extended Data Fig. 2c). We quantified the expression conservation of functionally
240 annotated sets of genes by testing the ability of gene sets to discriminate GABAergic consensus types.
241 This analysis was framed as a supervised learning task, both within- and between-species [30]. Within-
242 species, gene sets related to neuronal connectivity and signaling were most informative for cell type
243 identity (Extended Data Fig. 2g), as reported in human and mouse cortex [2,32]. All gene sets had
244 remarkably similar consensus type classification performance across species ($r > 0.95$; Fig. 2h),
245 pointing to strong evolutionary constraints on the cell type specificity of gene expression central to
246 neuronal function. Gene set classification performance was systematically reduced when training and
247 testing between primates (44% reduction) and between primates and mouse (65% reduction; Fig. 2h).
248 Therefore, many cell type marker genes were expressed in different consensus types between species.
249 Future comparative work can compare reductions in classification performance to evolutionary
250 distances between species to estimate rates of expression change across phylogenies.
251

252 Cross-species consensus types were defined for glutamatergic neurons using an identical approach as
253 for GABAergic neurons (Extended Data Fig. 3). In general, glutamatergic subclasses aligned well
254 across species and had a core set of conserved markers as well as many species-specific markers
255 (Extended Data Fig. 3a-c, genes listed in Supplementary Tables 10-11). 13 consensus types were
256 defined across species. Glutamatergic types had fewer conserved markers than GABAergic types
257 (Extended Data Fig. 3d-f,j), although subclasses and types were similarly robust (mean within-species
258 AUROC = 0.86 for GABAergic types and 0.85 for glutamatergic types) based on classification
259 performance (Extended Data Fig. 3k,l and Supplementary Table 9). Human and marmoset had
260 consistently more conserved marker genes than primates and mouse (Extended Data Fig. 3i) and could
261 be aligned at somewhat higher resolution (Extended Data Fig. 3g,h) for L5/6 NP and L5 IT subclasses.
262
263 Integration of non-neuronal cells was performed similarly to neurons (Extended Data Fig. 4a).
264 Consensus clusters (blue boxes in Extended Data Fig. 4c) that shared many marker genes were
265 identified across species (Extended Data Fig. 4d), and there was also evidence for the evolutionary
266 divergence of gene expression in consensus types. For example, the Astro_1 type had 560 DEGs
267 (Wilcox test; FDR < 0.01, log-fold change > 2) between human and mouse and only 221 DEGs
268 between human and marmoset (Extended Data Fig. 4e). The human cortex contains several
269 morphologically distinct astrocyte types [33]: interlaminar (ILA) in L1, protoplasmic in all layers, varicose
270 projection in deep layers, and fibrous in white matter (WM). We previously reported two transcriptomic
271 clusters in human MTG that corresponded to protoplasmic astrocytes and ILAs [2], and we validated
272 these types in M1 (Extended Data Fig. 4g,h). We identified a third type, Astro L1-6 *FGFR3 AQP1*, that
273 expresses *APQ4* and *TNC* and corresponds to fibrous astrocytes in WM (Extended Data Fig. 4g, left
274 ISH). A putative varicose projection astrocyte did not express human astrocyte markers (Extended Data
275 Fig. 4g, middle and right ISH), and this rare type may not have been sampled or is not
276 transcriptomically distinct.
277

278 Species comparison of non-neuronal cell types was more challenging than for neurons due to variable
279 sampling across species and more immature non-neuronal cells in mouse. 5- to 15-fold lower sampling
280 of non-neuronal cells in human impacted detection of rare types. For example, pericytes, smooth
281 muscle cells (SMCs), and some subtypes of vascular and leptomeningeal cells (VLMCs) were present
282 in marmoset and mouse and not human datasets (Extended Data Fig. 4c, right plot, blue arrows),
283 although these cells are clearly present in human cortex (for example, see [34]). A maturation lineage
284 between oligodendrocyte precursor cells (OPCs) and oligodendrocytes based on reported marker
285 genes [35] that was present in mouse and not primates (Extended Data Fig. 4b) likely represents the
286 younger age of mouse tissues used. Mitotic astrocytes (Astro_*Top2a*) were also only present in mouse
287 (Extended Data Fig. 4a,c) and represented 0.1% of non-neuronal cells. Primates had a unique
288 oligodendrocyte population (Oligo *SLC1A3 LOC103793418* in marmoset and Oligo L2-6 *OPALIN*
289 *MAP6D1* in human) that was not a distinct cluster in mouse (Extended Data Fig. 4c, left plot, blue
290 arrow). Surprisingly this oligodendrocyte clustered with glutamatergic types (Fig. 1c,d) and was
291 associated with neuronal transcripts such as *NPTX1*, *OLFM3*, and *GRIA1* (Extended Data Fig. 4i). This
292 was not an artifact, as FISH for markers of this type (*SOX10*, *ST18*) co-localized with neuronal markers
293 in the nuclei of cells that were sparsely distributed across all layers of human and marmoset M1
294 (Extended Data Fig. 4j). This may represent an oligodendrocyte type that expresses neuronal genes or
295 could represent phagocytosis of parts of neurons and accompanying transcripts that are sequestered in
296 phagolysosomes adjacent to nuclei.
297
298 To assess differential isoform usage between human and mouse, we used SSv4 data with full transcript
299 coverage and estimated isoform abundance in cell subclasses. Remarkably, 25% of moderately
300 expressed (> 10 transcripts per million) isoforms showed a large change (>9-fold) in usage between
301 species, and isoform switching was 30-60% more common in non-neuronal than neuronal cells
302 (Extended Data Fig. 2h,i, Supplementary Table 12). For example, β2-Chimaerin (*CHN2*), a gene shown
303 to mediate axonal pruning in the hippocampus [36], was highly expressed in human and mouse L5/6 NP

304 neurons. In mouse, the short isoform was almost exclusively expressed, while in human, longer
305 isoforms were also expressed (Extended Data Fig. 2j).
306
307 **Open chromatin profiling reveals distinct cell type gene regulation**
308 To directly match accessible chromatin profiles to RNA-defined cell populations, we used SNARE-Seq
309 [37], now modified for highly multiplexed combinatorial barcoding (SNARE-Seq2) [38]. We generated
310 84,178 and 9,946 dual-omic single-nucleus RNA and accessible chromatin (AC) datasets from human
311 (n = 2) and marmoset (n = 2) M1, respectively (Extended Data Fig. 5a-b, Supplementary Table 13). On
312 average, 2,242 genes (5,764 unique transcripts) were detected per nucleus for human and 3,858 genes
313 (12,400 unique transcripts) per nucleus for marmoset, due to more than 4-fold greater sequencing
314 depth for marmoset (average 17,576 reads per nucleus for human and 77,816 reads per nucleus for
315 marmoset).
316
317 To define consensus clusters, SNARE-seq2 single-nucleus RNA expression data were mapped to
318 human and marmoset transcriptomic clusters (Fig. 1c,d) based on correlated expression of cell type
319 marker genes. SNARE-seq2 transcriptomes were also independently clustered, with both approaches
320 giving consistent results (Extended Data Fig. 5c-f). Consensus clusters were more highly resolved in
321 transcriptomic compared to AC data (Extended Data Fig. 5g), and so an integrative approach was used
322 to achieve best matched AC-level cluster annotations (Extended Data Fig. 5h-k). AC peak calling at
323 multiple levels of cellular identity (for RNA consensus clusters, resolved AC clusters, subclasses and
324 classes) yielded a combined total of 273,103 (human) and 134,769 (marmoset) accessible sites, with
325 an average of 1527 or 1322 unique accessible peak fragment counts per nucleus, respectively. Gene
326 activity estimates based on cis-regulatory interactions predicted from co-accessible promoter and distal
327 peak regions using Cicero [39] were highly correlated with RNA expression values. This highlights the
328 ability of SNARE-Seq2 to meaningfully characterize AC at RNA-defined cellular resolution that cannot
329 be achieved using only AC data (Extended Data Fig. 6a-b). The AC-level clusters (Fig. 3a,b) that

330 showed similar coverage across individual samples (Extended Data Fig. 6c-f) revealed regions of open
331 chromatin that are extremely cell type specific (Fig. 3c). These regulatory regions were relatively more
332 abundant in glutamatergic compared to GABAergic neuron subpopulations (Fig. 3c-d, Supplementary
333 Table 14).
334
335 To better understand the interplay of gene regulation and expression, we compared transcript counts
336 and open chromatin measured in the same nuclei. For example, the GABAergic neuron marker *GAD2*
337 and the L2/3 glutamatergic neuron marker *CUX2* showed cell-type specific chromatin profiles for co-
338 accessible sites that were consistent with their corresponding transcript abundances (Fig. 3e-g).
339 Transcription factor binding site (TFBS) activities were calculated using chromVAR [40], permitting
340 discovery of differentially active TFBSs between cell types. To investigate the regulatory factors that
341 may contribute to marker gene expression, we evaluated active TFBSs for their enrichment within
342 marker gene co-accessible sites. This permitted direct cell type mapping of gene expression and
343 activity levels with the expression and activity of associated regulatory factors (Fig. 3g). Using this
344 strategy, we identified TFBS activities associated with subclass (Fig. 3h-i) and AC-cluster level
345 differentially expressed genes (DEGs) in human and marmoset (Supplementary Table 15). DEG
346 transcript levels and AC-inferred gene activity scores showed high correspondence (Fig. 3h). While
347 most subclasses also showed distinct TFBS activities, correspondence between human and marmoset
348 was higher for glutamatergic rather than GABAergic neurons (Fig. 3h,j). For GABAergic neuron
349 subclasses, gene expression profiles were more conserved than TFBS activities, consistent with fewer
350 differences between GABAergic subpopulations based on AC sites (Fig. 3a,b). This observation is also
351 consistent with fewer distinct TFBS activities among some inhibitory neuron subclasses (*Lamp5*, *Sncg*)
352 in human compared to marmoset (Fig. 3h), despite these cell types having a similar number of AC peak
353 counts (Extended Data Fig. 6d-f). Interestingly, glutamatergic neurons in L5 and L6 showed higher
354 correspondence between primates based on TFBS activities compared to average expression,

355 suggesting that gene regulatory processes are more highly conserved in these subclasses than target
356 gene expression.
357
358 **Methylomic profiling reveals conserved gene regulation**
359 We used snmC-seq2 [41] to profile the DNA methylome from individual cells in M1. Single-nuclei were
360 labeled with an anti-NeuN antibody and isolated by fluorescence-activated cell sorting (FACS), and
361 neurons were enriched (90% NeuN+ nuclei) to increase detection of rare types. Using snmC-seq2, we
362 generated single-nucleus methylcytosine datasets from M1 of human (n = 2 donors, 6,095 nuclei),
363 marmoset (n = 2, 6,090), and mouse (9,876) (Liu et al. companion paper) (Supplementary Table 16).
364 On average, 5.5 ± 2.7% (mean ± s.d.) of human, 5.6 ± 2.9% of marmoset and 6.2 ± 2.6% of mouse
365 genomes were covered by stringently filtered reads per cell, with 3.4×10^4 (56%), 1.8×10^4 (62%) and
366 4.5×10^4 (81%) genes detected per cell in the three species, respectively. Based on the DNA
367 methylome profiles in both CpG sites (CG methylation or mCG) and non-CpG sites (CH methylation or
368 mCH), we clustered nuclei (Methods) to group cell populations into 31 cell types in human, 36 cell types
369 in marmoset, and 42 cell types in mouse (Fig. 4a and Extended Data Fig. 7a,b). For each species, cell
370 type clusters could be robustly discriminated using a supervised classification model and had distinct
371 marker genes based on DNA methylation signatures for neurons (mCH) or non-neuronal cells (mCG)
372 (Methods). Differentially methylated regions (DMR) were determined for each cell type versus all other
373 cell types and yielded 9.8×10^5 DMRs in human, 1.0×10^6 in marmoset, and 1.8×10^6 in mouse.
374
375 We determined a consensus molecular classification of cell types in each species by integrating single-
376 nucleus methylomic data with the Cv3 transcriptomic data described above using measurements of
377 gene body differential methylation (CH-DMG) to approximate expression levels. Nuclei from the two
378 data modalities mixed well as visualized in ensemble UMAPs (Fig. 4b,c). Methylation clusters have
379 one-to-one, one-to-many, or many-to-many mapping relation to transcriptomic clusters (Fig. 1c-e and
380 Extended Data Fig. 7d-f). DMRs were quantified for each subclass versus all other subclasses (Fig.

381 4d), and glutamatergic neurons had more hypo-methylated DMRs compared to GABAergic neurons.
382 Methylome tracks at subclass level can be found at http://neomorph.salk.edu/aj2/pages/cross-species-
383 M1/. To identify enriched transcription factor binding sites (TFBS) in each species and subclass, we
384 performed motif enrichment analysis with hypo-methylated DMRs from one subclass against other
385 DMRs of the same species, and identified 102 ± 57 (mean ± s.d.) TFBS in each subclass (Extended
386 Data Fig. 8 and Supplementary Table 17). We repeated the enrichment analysis using TFBS motif
387 clusters [42] and found similarly distinct subclass signatures (Supplementary Table 18). Although
388 subclasses had unique marker genes (Fig. 2c, genes listed in Supplementary Table 8) and CH-DMG
389 across species, they had remarkably conserved TFBS motif enrichment (Fig. 4e,f and Extended Data
390 Fig. 8). For example, *TCF4* is robustly expressed in L5 IT neurons across species and shows
391 significant TFBS enrichment in hypo-methylated DMRs and AC sites. DMRs and AC sites provide
392 independent epigenomic information (Extended Data Fig. 7f,g) and can identify different TFBS
393 enrichment, such as for *ZNF148* in L5 IT neurons. These results are consistent with previous
394 observations of conserved TF network architectures in neural cell types between human and mouse
395 (Stergachis et al. 2014). Conserved sets of TFs have the potential to determine conserved and
396 divergent expression in consensus types based on shared or altered genomic locations of TFBS motifs
397 across species.
398
399 **Layer 4-like neurons in human M1**
400 M1 lacks a L4 defined by a thin band of densely packed "granular" neurons that is present in other
401 cortical areas, such as MTG (Fig. 5a), although prior studies have identified neurons with L4-like
402 synaptic properties in mice [14] and expression of *RORB*, a L4 marker, in non-human primate M1 [43]. To
403 address the potential existence of L4-like neurons in human M1 from a transcriptomic perspective, we
404 integrated snRNA-seq data from M1 and the granular MTG, where we previously described multiple L4
405 glutamatergic neuron types [2]. This alignment revealed a broadly conserved cellular architecture
406 between M1 and MTG (Fig. 5b,c, Extended Data Fig. 9) including M1 neuron types Exc L3 *RORB*

407 *OTOGL* (here, *OTOGL*) and Exc L3-5 *RORB LINC01202* (here, *LINC01202*) that map closely to MTG
408 neurons in deep L3 to L4 (Fig. 5c, red outlines). Interestingly, four MTG L2/3 IT types (*LTK*, *GLP2R*,
409 *FREM3*, and *CARM1P1*) whose distinct physiology and morphology are reported in a companion paper
410 [44] had less clear homology in M1 than other types (Extended Data Fig. 9a-c), pointing to more
411 variability across cortical areas of superficial as compared to deep glutamatergic neurons. To compare
412 laminar positioning in M1 and MTG, the relative cortical depth from pia for each neuron was estimated
413 based on the layer dissection and average layer thickness [45]. Transcriptomically similar cell types were
414 found at similar cortical depths in M1 and MTG, and the *OTOGL* and *LINC01202* types were located in
415 deep L3 and superficial L5 in M1 (Fig. 5d).
416
417 MTG contains three main transcriptomically-defined L4 glutamatergic neuron types (*FILIP1L*, *TWIST2*
418 and *ESR1*) and a deep L3 type (*COL22A1*) that is found on the border of L3 and L4 (Fig. 5e-g). The M1
419 types *OTOGL* and *LINC01202* matched one-to-one with MTG *COL22A1* and *ESR1*, whereas there
420 were no matches for the other two MTG L4 types (Fig. 5f). Based on snRNA-seq proportions, the L4-
421 like *OTOGL* type was much sparser in M1 than the *ESR1* type in MTG (Fig. 5e). Multiplex fluorescent in
422 situ hybridization (mFISH) with probes to cell type marker genes confirmed these findings. The MTG
423 *ESR1* type was highly enriched in L4, [2], and the homologous M1 *LINC01202* type was sparser and
424 more widely distributed across L3 and L5 (Fig. 5g). The MTG *COL22A1* type was tightly restricted to
425 the L3/4 border [2], and the M1 *OTOGL* type was similarly found at the L3/5 border. Quantification of
426 labeled cells as a fraction of DAPI+ cells in L3-5 showed similar frequencies of M1 *OTOGL* and MTG
427 *COL22A1* types and 4-fold sparser M1 *LINC01202* type versus MTG *ESR1* type (Fig. 5h). These data
428 indicate a conservation of deep L3 glutamatergic types and proportions across human cortical areas,
429 but with reduced diversity and sparsification of L4-like neurons to a single (ESR1) type in M1,
430 distributed more broadly where L4 would be if tightly aggregated.
431
432 **Chandelier cells share a core molecular identity across species**

433 Conserved transcriptomic and epigenomic features of consensus types likely contribute to cell function
434 and generate hypotheses about the gene regulatory mechanisms underlying cell type identity. Focused
435 analysis of *Pvalb*-expressing GABAergic neurons illustrates the power of these data to predict such
436 gene-function relationships. Cortical *Pvalb*-expressing neurons comprise two major types — basket
437 cells (BCs) and ChCs — that have fast-spiking electrical properties and distinctive cellular
438 morphologies. BCs selectively synapse onto the perisomatic region of glutamatergic pyramidal
439 neurons. ChCs, also called axo-axonic cells [46], selectively innervate the axon initial segment (AIS) of
440 pyramidal cells and have unique synaptic specializations called axon cartridges. These cartridges run
441 perpendicular to their post-synaptic target axon, giving a characteristic morphological appearance of
442 candlesticks on a chandelier. This highly conserved feature is shown with biocytin-filled cells from
443 mouse, rhesus macaque, and human (Fig. 6a). To reveal evolutionarily conserved transcriptomic
444 hallmarks of ChCs, we identified DEGs in ChCs versus BCs in each species using an ROC test. 357
445 DEGs were identified in at least one species, and marmoset ChCs shared more DEGs with human (61
446 genes) than mouse (29; Fig. 6b, Supplementary Table 19). Remarkably, only 25 DEGs were conserved
447 across all three species. One conserved gene, *UNC5B* (Fig. 6c), is a netrin receptor involved in axon
448 guidance and may help target ChC to pyramidal neuron AIS. Three transcription factors (*RORA*,
449 *TRPS1*, and *NFIB*) were conserved markers and may contribute to gene regulatory networks that
450 determine the unique attributes of ChCs.
451
452 To determine if ChCs had enriched epigenomic signatures for *RORA* and *NFIB* (*TRPS1* lacked motif
453 data), we compared DMRs between ChCs and BCs. In all species, *RORA* and *NFIB* had significant
454 CH-DMGs in ChCs not BCs (Fig. 6d), consistent with differential expression. To discern if these TFs
455 may preferentially bind to DNA in ChCs, we tested for TF motif enrichment in hypo-methylated (mCG)
456 DMRs and AC sites genome-wide. We found that the RORA motif was significantly enriched in DMRs
457 in primates (Fig. 6d) and in AC sites of ChCs in all species (Fig. 6e, Supplementary Table 14). The
458 NFIB binding motif was only significantly enriched in AC sites of mouse ChCs, possibly because

459 enrichment was transient during development or NFIB specificity is due to expression alone. Three
460 independent genomic assays converge to implicate *RORA* as a ChC-specific TF among *Pvalb*-
461 expression neurons. Notably, 60 of 357 DEGs contained a ROR-motif in DMRs and AC regions in at
462 least one species, further implicating *RORA* in defining ChC identity.
463
464 **Primate Betz cell specialization**
465 In mouse cortex, L5 glutamatergic neurons have distinct long-range projection targets (ET versus IT)
466 and transcriptomes [1]. L5 ET and IT neuron subclasses clearly align between human and mouse using
467 snRNA-seq in M1 (Extended Data Fig. 3) and in temporal [2] and fronto-insular cortex [12]. Betz cells in L5
468 of primate M1 connect to spinal motor-neurons via the pyramidal tracts and are predicted to be L5 ET
469 neurons. The species aligned transcriptomic types allow for the identification of genes whose
470 expression may contribute to conserved ET versus IT features and primate-specific physiology,
471 anatomy, and connectivity. Furthermore, Patch-seq methods that jointly measure the transcriptome,
472 physiological properties and morphology of cells, allow the direct identification and characterization of
473 L5 ET and IT neurons across mouse, non-human primate, and human. As primate physiology
474 experiments are largely restricted to macaque, we also profiled L5 of macaque M1 with snRNA-seq
475 (Cv3) to allow accurate Patch-seq mapping.
476
477 L5 ET neurons had many DEGs compared to L5 IT neurons in all 4 species. Approximately 50 DEGs
478 were conserved across all species and similarity to human varied as a function of evolutionary distance
479 (Fig. 7a, Supplementary Table 20). Several genes encoding ion channel subunits were enriched in ET
480 versus IT neurons in all species, potentially mediating conserved ET physiological properties (Fig. 7b).
481 A number of additional potassium and calcium channels were primate-enriched (Fig. 7c), potentially
482 underlying primate-specific ET or Betz cell physiology. Interestingly, many of these primate-specific ET-
483 enriched genes showed gradually increasing ET specificity in species more closely related to human.
484 To explore this idea of gradual evolutionary change further, we identified genes with increasing L5 ET

485 versus IT specificity as a function of evolutionary distance from human (Fig. 7d, Supplementary Table
486 21). Interestingly, this gene set was highly enriched for genes associated with axon guidance including
487 members of the Robo, Slit and Ephrin gene families. These genes are potential candidates for
488 regulating the cortico-motoneuronal connections associated with increasingly dexterous fine motor
489 control across these species [23].
490
491 To investigate if transcriptomically defined L5 ET types contain anatomically-defined Betz cells, FISH
492 for L5 ET neurons was combined with immunolabeling against SMI-32, a protein enriched in Betz cells
493 and other long-range projecting neurons in macaque [47–49] (Fig. 7e). Cells consistent with the size and
494 shape of Betz cells were identified in two L5 ET clusters (Exc L5 *FEZF2 ASGR2* and Exc L5 *FEZF2*
495 *CSN1S1*). Similar to previous reports on von Economo neurons in the insular cortex [12], ET clusters in
496 M1 also included neurons with non-Betz morphologies.
497
498 To facilitate cross-species comparisons of Betz cells and mouse ET neurons we made patch clamp
499 recordings from L5 neurons in acute and cultured slice preparations of mouse and macaque M1. For a
500 subset of recordings, Patch-seq analysis was applied for transcriptomic cell type identification
501 (Extended Data Fig. 10h). To permit visualization of cells in heavily myelinated macaque M1, we used
502 AAV viruses to drive fluorophore expression in glutamatergic neurons in macaque slice culture
503 (Extended Data Fig. 10g). As shown in Figure 7f, Patch-seq neurons mapping to the macaque Betz/ET
504 cluster (Exc L5 *FEZF2 LOC114676463*) had large somata (diameter > 65 μm) and long “tap root” basal
505 dendrites, canonical hallmarks of Betz cell morphology [17,50]. A unique opportunity to record from
506 neurosurgical tissue excised from human premotor cortex (near the confluence of the precentral and
507 superior frontal gyri) during an epilepsy treatment surgery using the same methods as for macaque
508 yielded multiple neurons that mapped transcriptomically to one of the Betz-containing cell types and
509 had canonical Betz cell morphology (Fig. 7g). Macaque and human ET neurons were grouped for

510 physiological analysis because intrinsic properties were not significantly different, and many
511 corticospinal axons originate from premotor cortex[23].
512
513 Shared transcriptomic profiles of mouse, primate, and human L5 ET neurons predicted conservation of
514 some physiological properties of rodent and primate neurons. Transcriptomically-defined ET neurons
515 across species expressed high levels of genes encoding an HCN channel-subunit and a regulatory
516 protein (*HCN1* and *PEX5L;* Fig. 7b). We hypothesized that HCN-dependent membrane properties,
517 which are used to distinguish rodent ET from IT neurons [51], would similarly separate cell types in
518 primates. Some primate L5 neurons possessed distinctive HCN-related properties such as a lower
519 input resistance (R_N) and a peak resonance (f_R) in voltage response around 3-9 Hz (Fig. 7h,i), similar to
520 rodent ET neurons. To determine whether HCN-related physiology is a conserved feature of L5
521 neurons, we grouped all neurons into physiologically defined ET and non-ET neurons based on their R_N
522 and f_R. We asked whether these physiologically-defined neurons corresponded to genetically-defined
523 ET/Betz or non-ET neurons using Patch-seq and cell-type specific mouse lines. For mouse M1, the ET-
524 specific *Thy1*-YFP[21,52] and IT specific *Etv1*-EGFP[53] mouse lines preferentially labeled physiologically
525 defined ET and non-ET neurons, respectively (Fig. 7j). For primates, transcriptomically-defined Betz
526 cells were physiologically defined ET neurons, whereas transcriptomically defined non-ET neurons
527 were physiologically defined non-ET neurons (Fig. 7k). Thus, there was broad correspondence
528 between physiologically-defined and genetically-defined ET neurons in both mouse and primate M1.
529 There were notable differences in physiology between mouse and primate ET neurons, however. A
530 greater fraction of primate ET neurons exhibited an exceptionally low R_N compared to mouse (Fig. 7l).
531 Additional differences in action potential properties across cell types and species may be explained in
532 part by differences in the expression of ion channel-related genes (Fig. 7c, Extended Data Fig. 10).
533
534 Most strikingly, primate Betz/ET neurons displayed a distinctive biphasic-firing pattern during long spike
535 trains. The firing rate of both primate and mouse non-ET neurons decreased to a steady state within

536 the first second of a 10 second depolarizing current injection, whereas the firing rate of mouse ET
537 neurons increased moderately over the same time period (Fig. 7m,n; Extended Data Fig. 10m,n). The
538 acceleration in rodent ET neurons has been attributed to the expression of Kv1-containing voltage-
539 gated K^+ channels that are encoded by genes like the conserved ET gene *KCNA1*. In macaque and
540 human ET/Betz neurons, a distinctive biphasic pattern was characterized by an early cessation of firing
541 followed by a sustained and dramatic increase in firing later in the current injection. Thus, while ET
542 neurons in both primate and rodent M1 displayed spike frequency acceleration, the temporal dynamics
543 and magnitude of this acceleration appears to be a unique feature of primate ET/Betz neurons. These
544 data emphasize how transcriptomic data from this specialized neuron type can be linked to shared and
545 unique physiological properties across species.
546

547 ## Discussion

548 Comparative analysis is a powerful strategy to understand brain structure and function. Species
549 conservation is strong evidence for functional relevance under evolutionary constraints that can help
550 identify critical molecular and regulatory mechanisms [54,55]. Conversely, divergence indicates adaptive
551 specialization, which may be essential to understand the mechanistic underpinnings of human brain
552 function and susceptibility to human-specific diseases. In the current study, we applied a comparative
553 approach to understand conserved and species-specific features of M1 at the level of cell types using
554 single-nucleus RNA-seq (Cv3 and SSv4), open chromatin (SNARE-seq2 and ATAC-seq) and DNA-
555 methylation (snmC-seq2) technologies. Integrated analysis of over 450,000 nuclei in human, non-
556 human primates (marmoset, a New World monkey, and to a lesser degree macaque, an Old World
557 monkey that is evolutionarily more closely related to humans), and mouse (see also companion paper
558 [6]) yielded a high-resolution, multimodal classification of cell types in each species, and a coarser
559 consensus classification conserved between rodent and primate lineages. Robust species conservation
560 strongly argues for the functional relevance of this consensus cellular architecture. Species

561 specializations are also apparent, both in the additional granularity in cell types within species and
562 differences between conserved cell types. A comparative evolutionary approach provides an anchor
563 point to define the cellular architecture of any tissue and to discover species-specific adaptations.
564
565 A key result of the current study is the identification of a consensus classification of cell types across
566 species that allows the comparison of relative similarities in human compared to common mammalian
567 model organisms in biomedical research. Prior studies have demonstrated that high resolution cellular
568 taxonomies can be generated in mouse, non-human primate and human cortex, and that there is
569 generally good concordance across species [2,11]. However, inconsistencies in the methods and
570 sampling depths used made strong conclusions difficult, compounded by the analysis of different
571 cortical regions in different species. The current study overcame these challenges by focusing on M1, a
572 functionally and anatomically conserved cortical region across mammals, and comparing a variety of
573 methods on similarly isolated tissues (and the same specimens from human and marmoset). Several
574 important points emerged from these integrated analyses. First, with deeper sampling and the same
575 methodology (snRNA-seq with Cv3), a similar cellular complexity on the order of 100 cell types was
576 seen in all three species. The highest resolution molecular classification was seen with RNA-seq
577 compared to epigenomic methods, and among RNA-seq methods with those that allow the most cells
578 to be analyzed. Strikingly, the molecular classifications were well aligned across all methods tested,
579 albeit at different levels of resolution as a function of the information content of the assay and the
580 number of cells profiled. All methods were consistent at the level of subclasses as defined above, both
581 across methods and species; significantly better alignment was achieved among species based on
582 transcriptomics, and with epigenomic methods in some subclasses. Mismatches in cellular sampling
583 affect the ability to compare across species; for example, higher non-neuronal sampling in mouse and
584 marmoset increased detection of rare cell types compared to human. One important comparison was
585 between plate-based (SSv4) and droplet-based (Cv3) RNA-seq of human nuclei, where we compared
586 results between approximately 10,000 SSv4 and 100,000 Cv3 nuclei. On average, SSv4 detected 30%

587 more genes per nucleus and enabled comparisons of isoform usage between cell types, albeit with 20-
588 fold greater sequencing depth. However, SSv4 cost 10 times as much as Cv3 and did not allow
589 detection of additional cell types.
590
591 The snmC-seq2 clustering aligned closely with the transcriptomic classification, although with
592 significantly lower resolution in rarer subclasses. Hypo-methylated sites correlated with gene
593 expression and specific transcription factor binding motifs were enriched in cell type specific sites.
594 Multi-omic SNARE-seq2 measured RNA profiles of nuclei that allowed high confidence assignment to
595 transcriptomic clusters. Examining accessible chromatin (AC) regions within the same nuclei led to
596 strong correlations between cell subclass or type gene expression and active regulatory regions of
597 open chromatin. Using this strategy, gene regulatory activities could be identified within RNA-defined
598 cell populations (including RNA consensus clusters) that could not be resolved from AC data alone
599 (Extended Data Fig. 6a, Supplementary Table 15). By joint consideration of these epigenomic
600 modalities, glutamatergic neurons were found to have more hypo-methylated DMRs and differentially
601 accessible chromatin, consistent with having larger somata and expressing more genes. Within-
602 species, cell types have many more unique AC sites than uniquely expressed marker genes. At the
603 same time, there is striking conservation across species of subclass TFBS motif enrichment within AC
604 and hypo-methylated DMRs. Most subclasses have distinct motifs, although L2/3 and L6 IT and *Lamp5*
605 and *Sncg* subclasses share many motifs and are more clearly distinguished based on gene expression.
606 Taken together, these results show a robust cell type classification that is consistent at the level of
607 subclasses both across transcriptomic and chromatin measures and across species, with additional cell
608 type-level granularity identified with transcriptomics.
609
610 Alignment across species allowed a comparison of relative similarities and differences between
611 species. A common (and expected) theme was that more closely related species are more similar to
612 one another. This was true at the level of gene expression and epigenome patterning across cell types,

613 and in the precision with which transcriptomically-defined cell types could be aligned across species.
614 For example, human and marmoset GABAergic types could be aligned at higher resolution than human
615 and mouse. Human was more similar to macaque than to marmoset. This indicates that cell type
616 similarity increases as a function of evolutionary distance to our closest common ancestors with mouse
617 (~70 mya), marmoset (~40 mya), and macaque (~25 mya). Interestingly, many gene expression
618 differences may change gradually over evolution. This is apparent in the graded changes in expression
619 levels of genes enriched in L5 ET versus L5 IT neurons and in the reduced performance of cell type
620 classification based on marker gene expression that is correlated with evolutionary distance between
621 species.
622
623 Several prominent species differences in cell type proportions were observed. First, the ratio of
624 glutamatergic excitatory projection neurons compared to GABAergic inhibitory interneurons was 2:1 in
625 human compared to 3:1 in marmoset and 5:1 in mouse and leads to a profound shift in the overall
626 excitation-inhibition balance of the cortex. A similar species difference has been described based on
627 histological measures (reviewed in [28]), indicating that snRNA-seq gives a reasonably accurate
628 measurement of cell type proportions. Surprisingly, the relative proportions of GABAergic subclasses
629 and types were similar across species. These results suggest a developmental shift in the size of the
630 GABAergic progenitor pool in the ganglionic eminences or an extended period of neurogenesis and
631 migration. A decreased proportion of the subcortically targeting L5 ET neurons in human was also
632 seen, as previously shown in temporal [2] and frontoinsular [12] cortex. This shift likely reflects the
633 evolutionary increase in cortical neurons relative to their subcortical targets [56] and was less prominent
634 in M1, suggesting regional variation in the proportion of L5 ET neurons. Finally, a large increase in the
635 proportion of L2 and L3 IT neurons was seen in human compared to mouse and marmoset. This
636 increase parallels the disproportionate expansion of human cortical area and supragranular layers that
637 contain neurons projecting to other parts of the cortex, presumably to facilitate greater corticocortical
638 communication. Interestingly, L2 and L3 IT neurons appear to be particularly highly variable across

639 cortical areas and species, and also are more diverse and specialized in human compared to mouse
640 (see companion paper [44]).
641
642 A striking and somewhat paradoxical observation is the high degree of species specialization of
643 consensus types. The majority of DEGs between cell types were consistently species-specific. This
644 result suggests that the conserved cellular features of a cell type are largely due to a minority of DEGs
645 with conserved expression patterns. The current study demonstrates this point for one of the most
646 distinctive brain cell types, the cortical *Pvalb*-expressing GABAergic ChC. ChCs in mouse, non-human
647 primate, and human have 100-150 genes with highly enriched expression compared to other *Pvalb*-
648 expressing interneurons (BCs); however, only 25 of these ChC-enriched genes are shared across
649 species. This small overlapping gene set includes several transcription factors and a member of the
650 netrin family (*UNC5B*) that could be responsible for AIS targeting. Binding sites for these TFs are
651 enriched in ChC cluster regions of open chromatin and in hypo-methylated regions around ChC-
652 enriched genes. While these associations between genes and cellular phenotypes for conserved and
653 divergent features remain to be tested, a comparative strategy can identify these core conserved genes
654 and make strong predictions about the TF code for cell types and the genes responsible for their
655 evolutionarily constrained functions.
656
657 M1 is an agranular cortex lacking a L4, although a recent study demonstrated that there are neurons
658 with L4-like properties in mouse [14]. Here we confirm and extend this finding in human M1. We find a L4-
659 like neuron type in M1 that aligns to a L4 type in human MTG and is scattered between the deep part of
660 L3 and the superficial part of L5 where L4 would be if aggregated into a layer. However, MTG
661 contained several additional L4 types not found in M1, and with a much higher frequency. The human
662 M1 L4-like type is part of the L5 IT_1 consensus cluster that includes several IT types in all species,
663 including two L4-like types in mouse (L4/5 IT_1 and L4/5 IT_2) that also express the canonical L4
664 marker *Rorb* (see companion paper [6]). Therefore, it appears that M1 has L4-like cells from a

transcriptomic perspective, but only a subset of the types compared to granular cortical areas, at much lower density, and scattered rather than aggregated into a tight layer.

The most distinctive cellular hallmark of M1 in primates and cats is the enormous Betz cell, which contributes to direct corticospinal connections to spinal motoneurons in primates that participate in fine motor control [15,16,57–59]. Intracellular recordings from cats have shown highly distinctive characteristics including HCN channel-related membrane properties, spike frequency acceleration, and extremely fast maintained firing rates [19,20]. However, they have never been recorded in primates using patch clamp physiology due to the high degree of myelination in M1 that prevents their visualization, and the inability to obtain motor cortex tissue from neurosurgical procedures which are careful to be function-sparing. A goal of the current project was to identify the transcriptomic cluster corresponding to Betz cells and use this to understand gene expression that may underlie their distinctive properties and species specializations. We have recently taken a similar approach to study von Economo neurons in the fronto-insular cortex, showing they are found within a transcriptomic class consisting of ET neurons [12]. Betz cells are classical ET neurons that, together with the axons of smaller corticospinal neurons, make up part of the pyramidal tract from the cortex to the spinal cord [16,60]. We show that neurons with Betz cell morphology label with markers for the M1 ET clusters. Like von Economo neurons, there does not appear to be an exclusively Betz transcriptomic type. Rather, M1 ET clusters are not exclusive for neurons with Betz morphology, and we find more than one ET cluster contains neurons with Betz morphology.

Although comparative transcriptomic alignments provide strong evidence for functional similarity, the distinctions between corticospinal neurons across species or even between L5 ET and IT neuron types in primates or humans has not been demonstrated physiologically. We recently developed a suite of methodologies for studying specific neuron types in human and non-human tissues, including triple modality Patch-seq to combine physiology, morphology and transcriptome analysis, acute and cultured

691 slice physiology in adult human neurosurgical resections and macaque brain, and AAV-based neuronal
692 labeling to allow targeting of neurons in highly myelinated tissues (companion paper [44]; [61] . Specifically,
693 these tools allow the targeting of L5 neurons in mouse and non-human primate and the assignment of
694 neurons to their transcriptomic types using Patch-seq, which we facilitated by generating and aligning a
695 L5 transcriptomic classification in macaque where such analyses could be performed. We show here
696 that several of the characteristic features of L5 ET versus IT neurons are conserved, and can be
697 reliably resolved from one another in mouse and non-human primate. Furthermore, macaque neurons
698 with Betz-like morphologies mapped to the Betz-containing clusters. However, as predicted by
699 differences in ion channel-related gene expression, not all physiological features were conserved
700 between macaque and mouse ET neurons. Betz/ET neurons had the distinctive pauses, bursting and
701 spike-frequency acceleration described previously in cats but not seen in rodents [19,20]. Finally, we had
702 access to an extremely rare human neurosurgical case where a region of premotor cortex was
703 resected. Similar to macaque M1, this premotor region contained large neurons with characteristic
704 Betz-like morphology that mapped transcriptomically to the Betz-containing clusters. Together these
705 results highlight the predictive power of transcriptomic mapping and cross-species inference of cell
706 types for L5 pyramidal neurons including the Betz cells. Furthermore, these data are consistent with
707 observations that Betz cells may not in fact be completely restricted to M1 but distribute across other
708 proximal motor-related areas that contribute to the pyramidal tract [62]. Finally, a number of ion channels
709 that may contribute to conserved ET versus IT features as well as species specializations of Betz cell
710 function were identified that provide candidate genes to explore gene-function relationships. For
711 example, axon guidance-associated genes are enriched in Betz-containing ET neuron types in
712 primates, possibly explaining why Betz cells in primates directly contact spinal motor neurons rather
713 than spinal interneurons as in rodents. Thus, as the comparative approach is helpful in identifying core
714 conserved molecular programs, it may be equally valuable to understand what is different in human or
715 can be well modeled in closer non-human primate relatives. This is particularly relevant in the context of

716 Betz cells and other ET neuron types that are selectively vulnerable in amyotrophic lateral sclerosis,
717 some forms of frontotemporal dementia, and other neurodegenerative conditions.
718

719 References

720 1. Tasic, B. *et al.* Shared and distinct transcriptomic cell types across neocortical areas. *Nature* **563**,
721 72–78 (2018).
722 2. Hodge, R. D. *et al.* Conserved cell types with divergent features in human versus mouse cortex.
723 *Nature* **573**, 61–68 (2019).
724 3. Tasic, B. *et al.* Adult mouse cortical cell taxonomy revealed by single cell transcriptomics. *Nat.*
725 *Neurosci.* **19**, 335–346 (2016).
726 4. Lake, B. B. *et al.* Neuronal subtypes and diversity revealed by single-nucleus RNA sequencing of
727 the human brain. *Science* **352**, 1586–1590 (2016).
728 5. Luo, C. *et al.* Single-cell methylomes identify neuronal subtypes and regulatory elements in
729 mammalian cortex. *Science* **357**, 600–604 (2017).
730 6. Yao, Z. *et al.* An integrated transcriptomic and epigenomic atlas of mouse primary motor cortex cell
731 types. *bioRxiv* 2020.02.29.970558 (2020) doi:10.1101/2020.02.29.970558.
732 7. Lake, B. B. *et al.* Integrative single-cell analysis of transcriptional and epigenetic states in the
733 human adult brain. *Nat. Biotechnol.* **36**, 70–80 (2018).
734 8. Zeisel, A. *et al.* Brain structure. Cell types in the mouse cortex and hippocampus revealed by
735 single-cell RNA-seq. *Science* **347**, 1138–1142 (2015).
736 9. Gray, L. T. *et al.* Layer-specific chromatin accessibility landscapes reveal regulatory networks in
737 adult mouse visual cortex. *Elife* **6**, (2017).
738 10. Lee, D.-S. *et al.* Simultaneous profiling of 3D genome structure and DNA methylation in single
739 human cells. *Nat. Methods* **16**, 999–1006 (2019).
740 11. Krienen, F. M., Goldman, M., Zhang, Q. & del Rosario, R. Innovations in primate interneuron

741 repertoire. *bioRxiv* (2019).
742 12. Hodge, R. D. *et al.* Transcriptomic evidence that von Economo neurons are regionally specialized
743 extratelencephalic-projecting excitatory neurons. *Nat. Commun.* **11**, 1172 (2020).
744 13. La Manno, G. *et al.* Molecular Diversity of Midbrain Development in Mouse, Human, and Stem
745 Cells. *Cell* **167**, 566–580.e19 (2016).
746 14. Yamawaki, N., Borges, K., Suter, B. A., Harris, K. D. & Shepherd, G. M. G. A genuine layer 4 in
747 motor cortex with prototypical synaptic circuit connectivity. *Elife* **3**, e05422 (2014).
748 15. Betz, W. Anatomischer Nachweis zweier Gehirncentra. *Zentralbl Med Wiss* **12**, (1874).
749 16. Lassek, A. M. The Human Pyramidal Tract II. A Numerical Investigation of the Betz Cells of the
750 Motor Area. *J. Nerv. Ment. Dis.* **94**, 225–226 (1941).
751 17. Jacobs, B. *et al.* Comparative morphology of gigantopyramidal neurons in primary motor cortex
752 across mammals. *J. Comp. Neurol.* **526**, 496–536 (2018).
753 18. Kaiserman-Abramof, I. R. & Peters, A. Some aspects of the morphology of Betz cells in the
754 cerebral cortex of the cat. *Brain Res.* **43**, 527–546 (1972).
755 19. Spain, W. J., Schwindt, P. C. & Crill, W. E. Post-inhibitory excitation and inhibition in layer V
756 pyramidal neurones from cat sensorimotor cortex. *The Journal of Physiology* vol. 434 609–626
757 (1991).
758 20. Chen, W., Zhang, J. J., Hu, G. Y. & Wu, C. P. Electrophysiological and morphological properties of
759 pyramidal and nonpyramidal neurons in the cat motor cortex in vitro. *Neuroscience* **73**, 39–55
760 (1996).
761 21. Miller, M. N., Okaty, B. W. & Nelson, S. B. Region-Specific Spike-Frequency Acceleration in Layer
762 5 Pyramidal Neurons Mediated by Kv1 Subunits. *Journal of Neuroscience* vol. 28 13716–13726
763 (2008).
764 22. Gu, Z. *et al.* Control of species-dependent cortico-motoneuronal connections underlying manual
765 dexterity. *Science* **357**, 400–404 (2017).
766 23. Lemon, R. N. Descending pathways in motor control. *Annu. Rev. Neurosci.* **31**, 195–218 (2008).

767 24. Stuart, T. *et al.* Comprehensive Integration of Single-Cell Data. *Cell* **177**, 1888–1902.e21 (2019).
768 25. Oberheim, N. A. *et al.* Uniquely Hominid Features of Adult Human Astrocytes. *Journal of*
769 *Neuroscience* vol. 29 3276–3287 (2009).
770 26. Colombo, J. A. The interlaminar glia: from serendipity to hypothesis. *Brain Struct. Funct.* **222**,
771 1109–1129 (2017).
772 27. Bakken, T. E. *et al.* Single-nucleus and single-cell transcriptomes compared in matched cortical
773 cell types. *PLoS One* **13**, e0209648 (2018).
774 28. Džaja, D., Hladnik, A., Bičanić, I., Baković, M. & Petanjek, Z. Neocortical calretinin neurons in
775 primates: increase in proportion and microcircuitry structure. *Front. Neuroanat.* **8**, 103 (2014).
776 29. DeFelipe, J., Alonso-Nanclares, L. & Arellano, J. I. Microstructure of the neocortex: comparative
777 aspects. *J. Neurocytol.* **31**, 299–316 (2002).
778 30. Crow, M., Paul, A., Ballouz, S., Huang, Z. J. & Gillis, J. Characterizing the replicability of cell types
779 defined by single cell RNA-sequencing data using MetaNeighbor. *Nat. Commun.* **9**, 884 (2018).
780 31. Boldog, E. *et al.* Transcriptomic and morphophysiological evidence for a specialized human cortical
781 GABAergic cell type. *Nat. Neurosci.* **21**, 1185–1195 (2018).
782 32. Paul, A. *et al.* Transcriptional Architecture of Synaptic Communication Delineates GABAergic
783 Neuron Identity. *Cell* **171**, 522–539.e20 (2017).
784 33. Verkhratsky, A. & Nedergaard, M. The homeostatic astroglia emerges from evolutionary
785 specialization of neural cells. *Philos. Trans. R. Soc. Lond. B Biol. Sci.* **371**, (2016).
786 34. Nortley, R. *et al.* Amyloid β oligomers constrict human capillaries in Alzheimer's disease via
787 signaling to pericytes. *Science* vol. 365 eaav9518 (2019).
788 35. La Manno, G. *et al.* RNA velocity of single cells. *Nature* **560**, 494–498 (2018).
789 36. Riccomagno, M. M. *et al.* The RacGAP β2-Chimaerin selectively mediates axonal pruning in the
790 hippocampus. *Cell* **149**, 1594–1606 (2012).
791 37. Chen, S., Lake, B. B. & Zhang, K. High-throughput sequencing of the transcriptome and chromatin
792 accessibility in the same cell. *Nat. Biotechnol.* **37**, 1452–1457 (2019).

793 38. Nongluk Plongthongkum, Dinh Diep, Song Chen, Blue B. Lake, Kun Zhang. Scalable Dual-omic
794 Profiling with Single-nucleus Chromatin Accessibility and mRNA Expression Sequencing 2
795 (SNARE-Seq2). (2020).
796 39. Pliner, H. A. *et al.* Cicero Predicts cis-Regulatory DNA Interactions from Single-Cell Chromatin
797 Accessibility Data. *Mol. Cell* **71**, 858–871.e8 (2018).
798 40. Schep, A. N., Wu, B., Buenrostro, J. D. & Greenleaf, W. J. chromVAR: inferring transcription-
799 factor-associated accessibility from single-cell epigenomic data. *Nat. Methods* **14**, 975–978 (2017).
800 41. Luo, C. *et al.* Robust single-cell DNA methylome profiling with snmC-seq2. *Nat. Commun.* **9**, 3824
801 (2018).
802 42. Fornes, O. *et al.* JASPAR 2020: update of the open-access database of transcription factor binding
803 profiles. *Nucleic Acids Res.* **48**, D87–D92 (2020).
804 43. Bernard, A. *et al.* Transcriptional architecture of the primate neocortex. *Neuron* **73**, 1083–1099
805 (2012).
806 44. Berg, J. *et al.* Human cortical expansion involves diversification and specialization of supragranular
807 intratelencephalic-projecting neurons. *bioRxiv* 2020.03.31.018820 (2020)
808 doi:10.1101/2020.03.31.018820.
809 45. von Economo, C. & Koskinas, G. N. *Die Cytoarchitektonik der Hirnrinde des Erwachsenen*
810 *Menschen*. (J. Springer, 1925).
811 46. Somogyi, P., Freund, T. F. & Cowey, A. The axo-axonic interneuron in the cerebral cortex of the
812 rat, cat and monkey. *Neuroscience* **7**, 2577–2607 (1982).
813 47. Hof, P. R., Nimchinsky, E. A. & Morrison, J. H. Neurochemical phenotype of corticocortical
814 connections in the macaque monkey: quantitative analysis of a subset of neurofilament protein-
815 immunoreactive projection neurons in frontal, parietal, temporal, and cingulate cortices. *J. Comp.*
816 *Neurol.* **362**, 109–133 (1995).
817 48. Tsang, Y. M., Chiong, F., Kuznetsov, D., Kasarskis, E. & Geula, C. Motor neurons are rich in non-
818 phosphorylated neurofilaments: cross-species comparison and alterations in ALS. *Brain Res.* **861**,

45–58 (2000).

49. Preuss, T. M., Stepniewska, I., Jain, N. & Kaas, J. H. Multiple divisions of macaque precentral motor cortex identified with neurofilament antibody SMI-32. *Brain Research* vol. 767 148–153 (1997).

50. Scheibel, M. E., Davies, T. L., Lindsay, R. D. & Scheibel, A. B. Basilar dendrite bundles of giant pyramidal cells. *Exp. Neurol.* **42**, 307–319 (1974).

51. Baker, A. *et al.* Specialized Subpopulations of Deep-Layer Pyramidal Neurons in the Neocortex: Bridging Cellular Properties to Functional Consequences. *J. Neurosci.* **38**, 5441–5455 (2018).

52. Feng, G. *et al.* Imaging neuronal subsets in transgenic mice expressing multiple spectral variants of GFP. *Neuron* **28**, 41–51 (2000).

53. Groh, A. *et al.* Cell-Type Specific Properties of Pyramidal Neurons in Neocortex Underlying a Layout that Is Modifiable Depending on the Cortical Area. *Cerebral Cortex* vol. 20 826–836 (2010).

54. Tosches, M. A. *et al.* Evolution of pallium, hippocampus, and cortical cell types revealed by single-cell transcriptomics in reptiles. *Science* **360**, 881–888 (2018).

55. Arendt, D. *et al.* The origin and evolution of cell types. *Nat. Rev. Genet.* **17**, 744–757 (2016).

56. Herculano-Houzel, S., Catania, K., Manger, P. R. & Kaas, J. H. Mammalian Brains Are Made of These: A Dataset of the Numbers and Densities of Neuronal and Nonneuronal Cells in the Brain of Glires, Primates, Scandentia, Eulipotyphlans, Afrotherians and Artiodactyls, and Their Relationship with Body Mass. *Brain Behav. Evol.* **86**, 145–163 (2015).

57. Rivara, C.-B., Sherwood, C. C., Bouras, C. & Hof, P. R. Stereologic characterization and spatial distribution patterns of Betz cells in the human primary motor cortex. *Anat. Rec. A Discov. Mol. Cell. Evol. Biol.* **270**, 137–151 (2003).

58. Evarts, E. V. Representation of movements and muscles by pyramidal tract neurons of the precentral motor cortex. in *Neurophysiological basis of normal and abnormal motor activities* 215–253 (Raven Press New York, 1967).

59. Evarts, E. V. RELATION OF DISCHARGE FREQUENCY TO CONDUCTION VELOCITY IN

845 PYRAMIDAL TRACT NEURONS. *J. Neurophysiol.* **28**, 216–228 (1965).
846 60. Lassek, A. M. THE PYRAMIDAL TRACT: A STUDY OF RETROGRADE DEGENERATION IN THE
847 MONKEY. *Arch NeurPsych* **48**, 561–567 (1942).
848 61. Ting, J. T. *et al.* A robust ex vivo experimental platform for molecular-genetic dissection of adult
849 human neocortical cell types and circuits. *Sci. Rep.* **8**, 8407 (2018).
850 62. Vigneswaran, G., Kraskov, A. & Lemon, R. N. Large Identified Pyramidal Cells in Macaque Motor
851 and Premotor Cortex Exhibit 'Thin Spikes': Implications for Cell Type Classification. *Journal of*
852 *Neuroscience* vol. 31 14235–14242 (2011).
853 63. Krimer, L. S. *et al.* Cluster Analysis–Based Physiological Classification and Morphological
854 Properties of Inhibitory Neurons in Layers 2–3 of Monkey Dorsolateral Prefrontal Cortex. *J.*
855 *Neurophysiol.* **94**, 3009–3022 (2005).
856 64. Rotaru, D. C. *et al.* Functional properties of GABA synaptic inputs onto GABA neurons in monkey
857 prefrontal cortex. *J. Neurophysiol.* **113**, 1850–1861 (2015).
858 65. Gouwens, N. W. *et al.* Toward an integrated classification of neuronal cell types: morphoelectric
859 and transcriptomic characterization of individual GABAergic cortical neurons. *bioRxiv*
860 2020.02.03.932244 (2020) doi:10.1101/2020.02.03.932244.
861 66. Fetz, E. E., Cheney, P. D., Mewes, K. & Palmer, S. Control of forelimb muscle activity by
862 populations of corticomotoneuronal and rubromotoneuronal cells. *Prog. Brain Res.* **80**, 437–49;
863 discussion 427–30 (1989).
864 67. Mi, H., Muruganujan, A., Ebert, D., Huang, X. & Thomas, P. D. PANTHER version 14: more
865 genomes, a new PANTHER GO-slim and improvements in enrichment analysis tools. *Nucleic*
866 *Acids Res.* **47**, D419–D426 (2019).
867 68. Koopmans, F. *et al.* SynGO: An Evidence-Based, Expert-Curated Knowledge Base for the
868 Synapse. *Neuron* **103**, 217–234.e4 (2019).
869 69. Luo, C. *et al.* Single nucleus multi-omics links human cortical cell regulatory genome diversity to
870 disease risk variants. *bioRxiv* 2019.12.11.873398 (2019) doi:10.1101/2019.12.11.873398.

871 70. Amemiya, H. M., Kundaje, A. & Boyle, A. P. The ENCODE Blacklist: Identification of Problematic
872 Regions of the Genome. *Sci. Rep.* **9**, 9354 (2019).
873 71. Wolf, F. A., Angerer, P. & Theis, F. J. SCANPY: large-scale single-cell gene expression data
874 analysis. *Genome Biol.* **19**, 15 (2018).
875 72. Traag, V. A., Waltman, L. & van Eck, N. J. From Louvain to Leiden: guaranteeing well-connected
876 communities. *Sci. Rep.* **9**, 5233 (2019).
877 73. Guyon, I., Weston, J., Barnhill, S. & Vapnik, V. Gene Selection for Cancer Classification using
878 Support Vector Machines. *Mach. Learn.* **46**, 389–422 (2002).
879 74. Brodersen, K. H., Ong, C. S., Stephan, K. E. & Buhmann, J. M. The Balanced Accuracy and Its
880 Posterior Distribution. in *2010 20th International Conference on Pattern Recognition* 3121–3124
881 (2010).
882 75. Lemaître, G., Nogueira, F. & Aridas, C. K. Imbalanced-learn: A Python Toolbox to Tackle the
883 Curse of Imbalanced Datasets in Machine Learning. *J. Mach. Learn. Res.* **18**, 1–5 (2017).
884 76. Hie, B., Bryson, B. & Berger, B. Efficient integration of heterogeneous single-cell transcriptomes
885 using Scanorama. *Nat. Biotechnol.* **37**, 685–691 (2019).
886 77. He, Y. *et al.* Spatiotemporal DNA Methylome Dynamics of the Developing Mammalian Fetus.
887 doi:10.1101/166744.
888 78. McLeay, R. C. & Bailey, T. L. Motif Enrichment Analysis: a unified framework and an evaluation on
889 ChIP data. *BMC Bioinformatics* **11**, 165 (2010).
890 79. Palmer, C., Liu, C. & Chun, J. Nuclei Isolation for SNARE-seq2 v1 (protocols.io.8tvhwn6).
891 doi:10.17504/protocols.io.8tvhwn6.
892 80. Lun, A. T. L. *et al.* EmptyDrops: distinguishing cells from empty droplets in droplet-based single-
893 cell RNA sequencing data. *Genome Biol.* **20**, 63 (2019).
894 81. Gayoso, A. & Shor, J. *GitHub: DoubletDetection*. (2019). doi:10.5281/zenodo.2678042.
895 82. Hahne, F. & Ivanek, R. Visualizing Genomic Data Using Gviz and Bioconductor. *Methods Mol. Biol.*
896 **1418**, 335–351 (2016).

897 83. Buenrostro, J. D. *et al.* Single-cell chromatin accessibility reveals principles of regulatory variation.
898 *Nature* **523**, 486–490 (2015).
899 84. Cusanovich, D. A. *et al.* Multiplex single-cell profiling of chromatin accessibility by combinatorial
900 cellular indexing. *Science* vol. 348 910–914 (2015).
901 85. Yue, F. *et al.* A comparative encyclopedia of DNA elements in the mouse genome. *Nature* **515**,
902 355–364 (2014).
903 86. Levine, J. H. *et al.* Data-Driven Phenotypic Dissection of AML Reveals Progenitor-like Cells that
904 Correlate with Prognosis. *Cell* **162**, 184–197 (2015).
905 87. Graybuck, L. T. *et al.* Prospective, brain-wide labeling of neuronal subclasses with enhancer-driven
906 AAVs. (2019) doi:10.1101/525014.
907 88. Ting, J. T., Daigle, T. L., Chen, Q. & Feng, G. Acute brain slice methods for adult and aging
908 animals: application of targeted patch clamp analysis and optogenetics. *Methods Mol. Biol.* **1183**,
909 221–242 (2014).
910 89. Gouwens, N. W. *et al.* Classification of electrophysiological and morphological neuron types in the
911 mouse visual cortex. *Nat. Neurosci.* **22**, 1182–1195 (2019).
912 90. Chan, K. Y. *et al.* Engineered AAVs for efficient noninvasive gene delivery to the central and
913 peripheral nervous systems. *Nat. Neurosci.* **20**, 1172–1179 (2017).
914 91. Rudy, B. & McBain, C. J. Kv3 channels: voltage-gated K+ channels designed for high-frequency
915 repetitive firing. *Trends Neurosci.* **24**, 517–526 (2001).

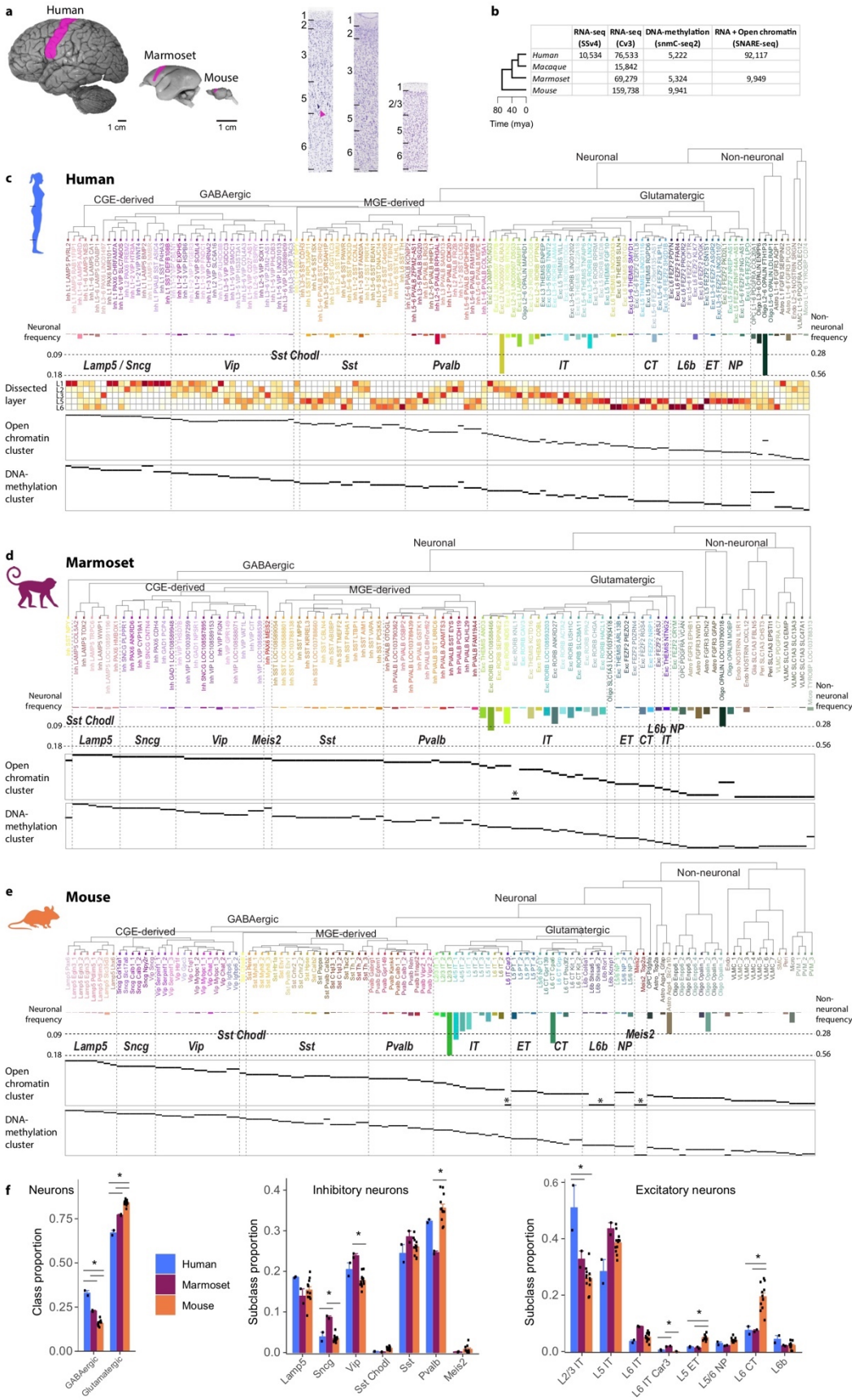
a
Human
Marmoset
Mouse
1 cm
1 cm
b
RNA-seq (SSv4)
RNA-seq (Cv3)
DNA-methylation (snmC-seq2)
RNA + Open chromatin (SNARE-seq)
Human 10,534 76,533 5,222 92,117
Macaque 15,842
Marmoset 69,279 5,324 9,949
Mouse 159,738 9,941
80 40 0
Time (mya)
c
Human
Neuronal
Non-neuronal
GABAergic
Glutamatergic
CGE-derived
MGE-derived
Neuronal frequency
Non-neuronal frequency
Lamp5 / Sncg
Vip
Sst Chodl
Sst
Pvalb
IT
CT
L6b
ET
NP
Dissected layer
Open chromatin cluster
DNA-methylation cluster
d
Marmoset
Neuronal
Non-neuronal
GABAergic
Glutamatergic
CGE-derived
MGE-derived
Neuronal frequency
Non-neuronal frequency
Sst Chodl
Lamp5
Sncg
Vip
Meis2
Sst
Pvalb
IT
ET
CT
L6b
NP
Open chromatin cluster
DNA-methylation cluster
e
Mouse
Non-neuronal
Neuronal
GABAergic
Glutamatergic
CGE-derived
MGE-derived
Neuronal frequency
Non-neuronal frequency
Sst Chodl
Meis2
Lamp5
Sncg
Vip
Sst
Pvalb
IT
ET
CT
L6b
NP
Open chromatin cluster
DNA-methylation cluster
f
Neurons
Class proportion
GABAergic
Glutamatergic
Human
Marmoset
Mouse
Inhibitory neurons
Subclass proportion
Lamp5
Sncg
Vip
Sst Chodl
Sst
Pvalb
Meis2
Excitatory neurons
Subclass proportion
L2/3 IT
L5 IT
L6 IT
L6 IT Car3
L5 ET
L5/6 NP
L6 CT
L6b

917 **Figure 1. Molecular taxonomy of cell types in M1 of human, marmoset, and mouse. a**, M1
918 highlighted in lateral views of neocortex across species. Nissl-stained sections of M1 annotated with
919 layers and showing the relative expansion of cortical thickness, particularly L2 and L3 in primates, and
920 large pyramidal neurons or 'Betz' cells in human L5 (arrowhead). Scale bars, 100 μm. **b**, Phylogeny of
921 species and number of nuclei included in analysis for each molecular assay. All assays used nuclei
922 isolated from the same donors for human and marmoset. SSv4, SMART-Seq v4; Cv3, Chromium v3;
923 mya, millions of years ago. **c-e**, Dendrograms of cell types defined by RNA-seq (Cv3) for human (**c**),
924 marmoset (**d**), and mouse (**e**) and annotated with cluster frequency and dissected layer (human only).
925 Epigenomic clusters (in rows) aligned to RNA-seq clusters as indicated by horizontal black bars.
926 Asterisks denote RNA clusters that lack corresponding epigenomic clusters. **f**, Relative proportions of
927 cells in several classes and subclasses were significantly different between species based on an
928 ANOVA followed by Tukey's HSD tests (asterisk, adjusted $P < 0.05$).
929

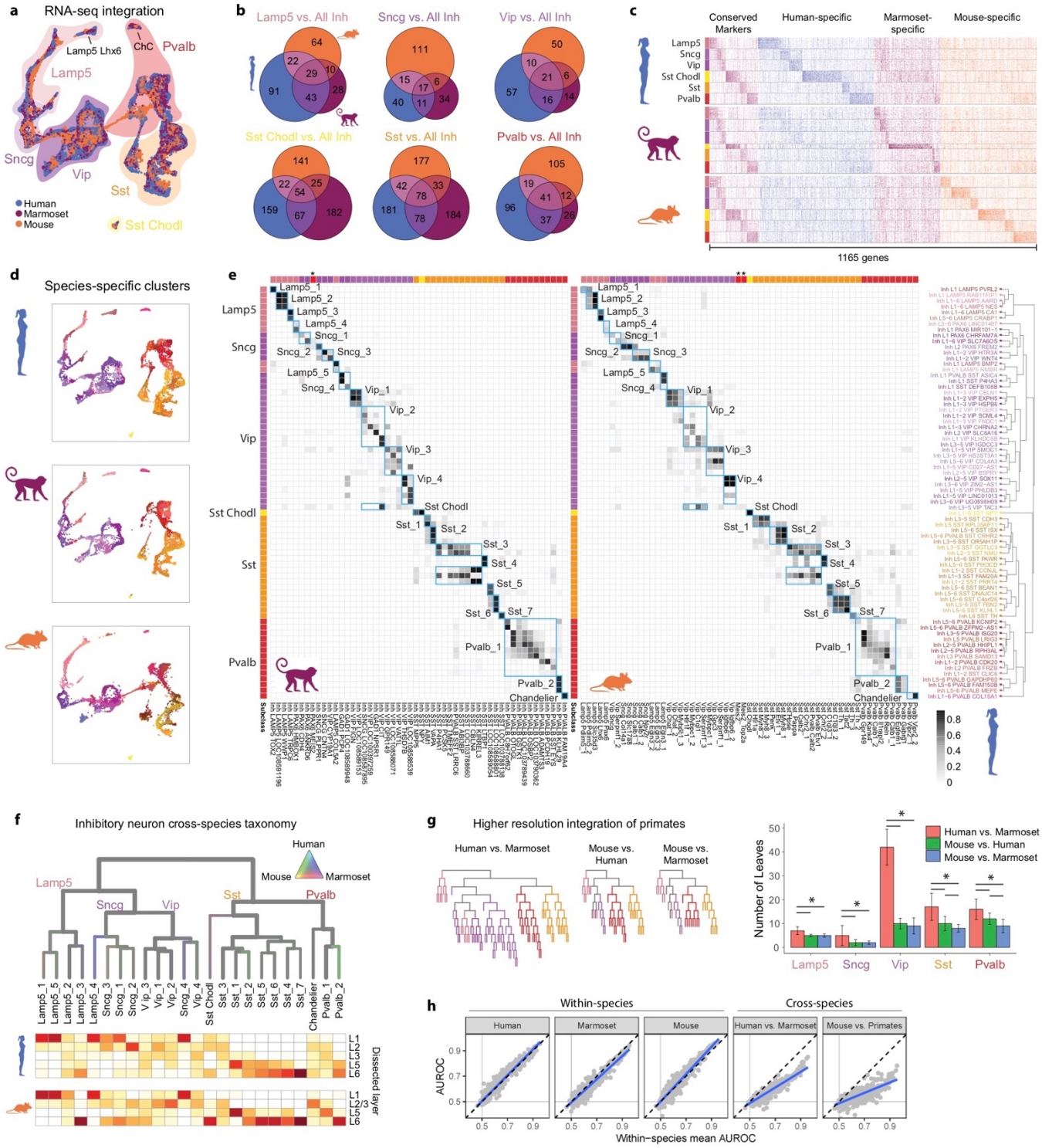

Figure 2. Evolution of GABAergic neuron types across species. a, UMAP projection of integrated snRNA-seq data from human, marmoset, and mouse GABAergic neurons. Filled outlines indicate cell subclasses. **b,** Venn diagrams indicating the number of shared DEGs across species by subclass.

934 DEGs were determined by ROC tests of each subclass versus all other GABAergic subclasses within a
935 species. **c,** Heatmap of all DEGs from **b** ordered by subclass and species enrichment. Heatmap shows
936 gene expression scaled by column for up to 50 randomly sampled nuclei from each subclass for each
937 species. **d,** UMAP projection from **a**, separated by species, and colored by within-species clusters. **e,**
938 Cluster overlap heatmap showing the proportion of nuclei in each pair of species clusters that are
939 mixed in the cross-species integrated space. Cross-species consensus clusters are indicated by
940 labeled blue boxes. Human clusters (rows) are ordered by the dendrogram reproduced from **Figure 1c**.
941 Marmoset (left columns) and mouse (right columns) clusters are ordered to align with human clusters.
942 Color bars at top and left indicate subclasses of within-species clusters. Asterisks indicate marmoset
943 and mouse Meis2 subclasses, which were not present in human. **f,** Dendrogram of GABAergic neuron
944 consensus clusters with edges colored by species mixture (grey, well mixed). Below: Estimated spatial
945 distributions of clusters based on layer dissections in human (top) and mouse (bottom). **g,**
946 Dendrograms of pairwise species integrations, colored by subclass. Bar plots quantifying well-mixed
947 leaf nodes. Significant differences (adjusted $P < 0.05$, Tukey's HSD test) between species are indicated
948 for each subclass. **h,** Scatter plots of MetaNeighbor analysis showing the performance (AUROC) of
949 gene-sets to classify GABAergic neurons within and between species. Blue lines, linear regression fits;
950 black lines, mean within species performance; grey lines, performance equivalent to chance.
951

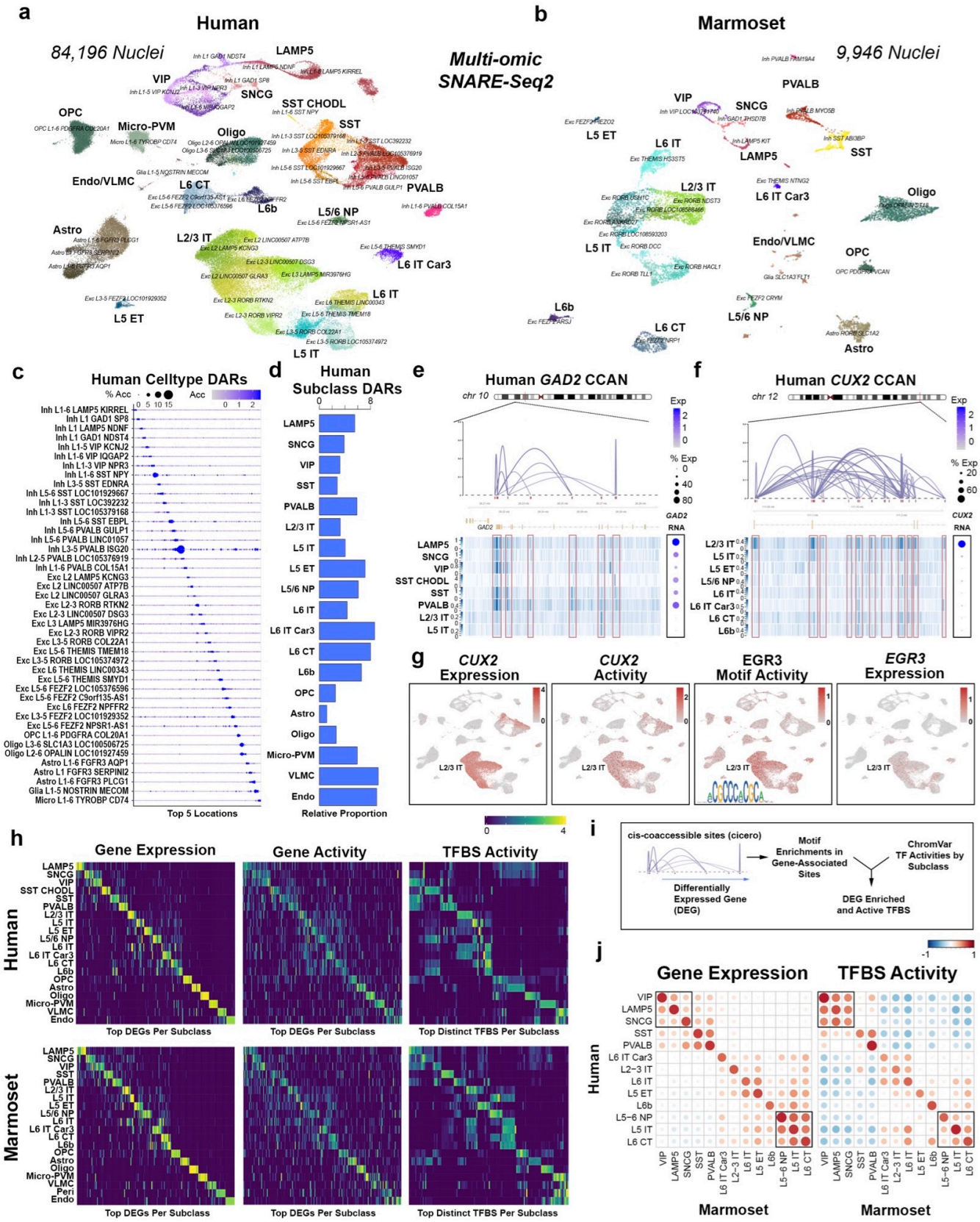
a
Human
84,196 Nuclei
Multi-omic SNARE-Seq2
b
Marmoset
9,946 Nuclei
c
Human Celltype DARs
d
Human Subclass DARs
Relative Proportion
e
Human GAD2 CCAN
f
Human CUX2 CCAN
g
CUX2 Expression
CUX2 Activity
EGR3 Motif Activity
EGR3 Expression
h
Gene Expression
Gene Activity
TFBS Activity
Top DEGs Per Subclass
Top Distinct TFBS Per Subclass
i
cis-coaccessible sites (cicero)
Differentially Expressed Gene (DEG)
Motif Enrichments in Gene-Associated Sites
ChromVar TF Activities by Subclass
DEG Enriched and Active TFBS
j
Gene Expression
TFBS Activity
Human
Marmoset

952

953 **Figure 3. Dual-omic expression and chromatin accessibility reveals regulatory processes**
954 **defining M1 cell types. a-b** UMAP visualizations of human (**a**) and marmoset (**b**) M1 SNARE-Seq2
955 data (2 individuals per species) indicating both subclass and accessibility-level cluster identities. **c**, Dot
956 plot showing proportion and scaled average accessibility of differentially accessible regions (DARs)
957 identified between human AC clusters (adjusted P < 0.001, log-fold change > 1, top 5 distinct sites per
958 cluster). **d**, Proportion of total human or marmoset DARs identified between subclasses (adjusted P <
959 0.001, log-fold change > 1) after normalization to cluster sizes. **e-f**, Connection plots for cis-co-
960 accessible network (CCAN) sites associated with the human *GAD2* (**e**) and *CUX2* (**f**) genes.
961 Corresponding AC read pile-up tracts for GABAergic and select glutamatergic subclasses are shown.
962 Right panels are dot plots showing the percentage of expressing nuclei and average gene expression
963 values (log scale) for *GAD2* or *CUX2* within each of the clusters indicated. **g**, UMAP plots as in Figure
964 5a (human) showing (scaled from low—gray to high—red) *CUX2* gene expression (RNA) and activity
965 level predicted from AC data. UMAP plots for activity level of the EGR3-binding motif, identified using
966 chromVAR and found to be enriched within *CUX2* co-accessible sites, and the corresponding
967 expression (RNA) of the *EGR3* gene are shown. **h**, Heatmaps for human (top) and marmoset (bottom)
968 showing TFBS enrichments, according to the scheme outlined in (**i**), within genes differentially
969 expressed between subclasses and having at least two cis-co-accessible sites. Left panels show
970 scaled average (log scale) gene expression values (RNA) for the top DEGs (adjusted P < 0.05, log-fold
971 change > 1, top 10 distinct sites per cluster visualized), middle panels show the corresponding scaled
972 average cicero gene activity scores and the right panels show scaled values for the corresponding top
973 distinct chromVAR TFBS activities (adjusted P < 0.05, log-fold change > 0.5, top 10 distinct sites per
974 cluster visualized). **j**, Correlation plots comparing scaled average gene expression profiles (left panel)
975 or chromVAR TFBS activity scores (right panel) between human and marmoset matched subclasses.
976

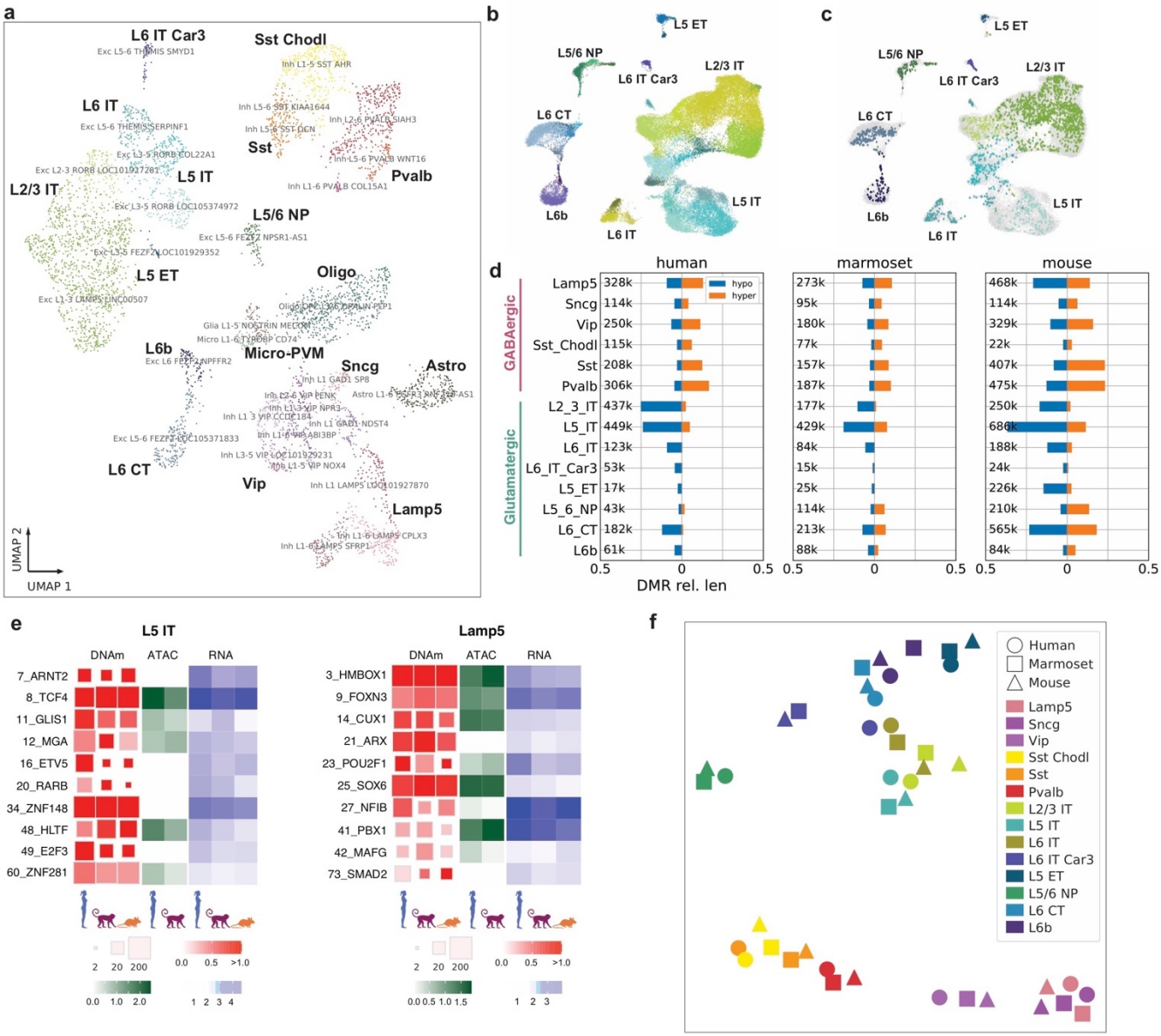

Figure 4. DNA methylation differences across clusters and species. a, UMAP visualization of human M1 DNAm-seq (snmC-seq2) data indicating both subclass and DNAm cluster identities. **b**,**c**, UMAP visualization of integration between DNAm-seq and RNA-seq of human glutamatergic neurons colored by cell subclass for all nuclei (**b**) or only nuclei profiled with DNAm-seq (**c**). **d**, Barplots of the relative lengths of hypo- and hyper-methylated DMRs among cell subclasses across three species normalized by cytosine coverage genome-wide (Methods). Total number of DMRs for each subclass

984 are listed (k, thousands). **e**, Distinct TF motif enrichment for L5 IT and *Lamp5* subclasses across

985 species. **f**, t-SNE visualization of subclass TF motif enrichment that is conserved across species.

986

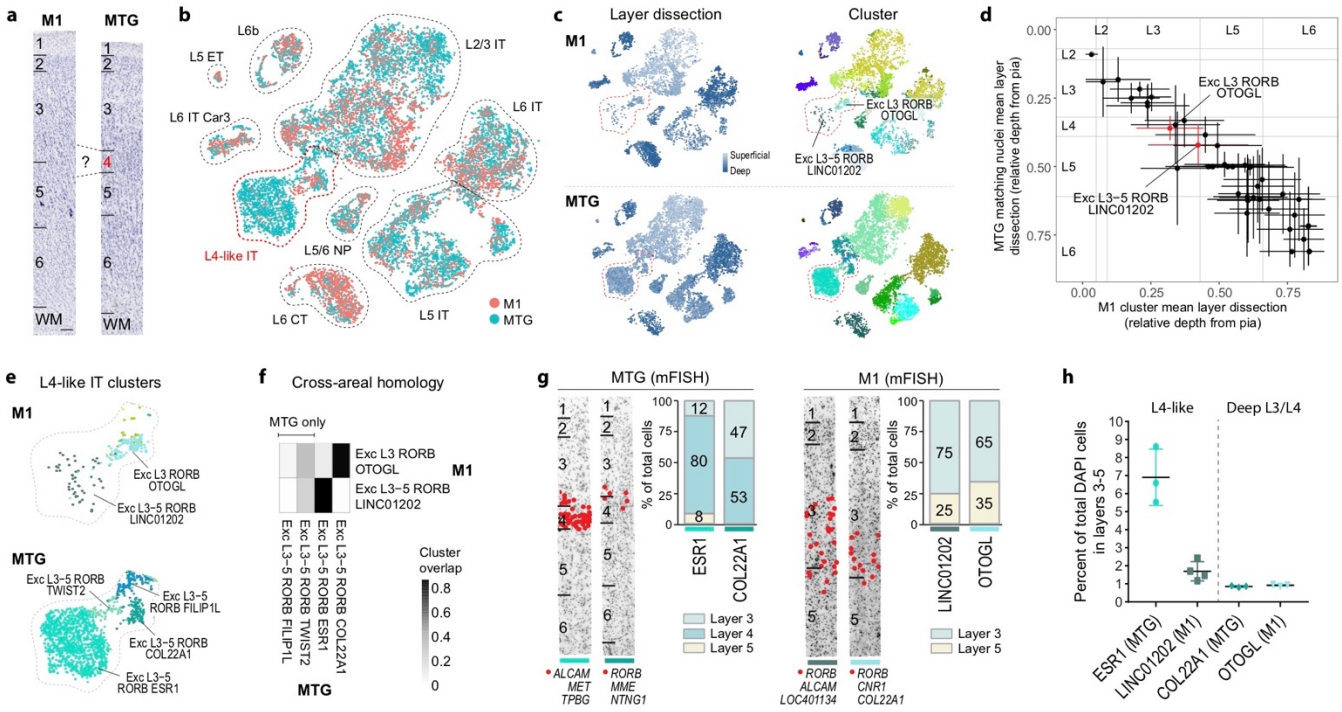

Figure 5. L4-like neurons identified in M1 based on cross-areal cell type homology. a, t-SNE projection of glutamatergic neuronal nuclei from M1 and MTG based on similarity of integrated expression levels. Nuclei are intermixed within all cell subclasses. **b**, Nuclei annotated based on the relative depth of the dissected layer and within-area cluster. A subset of clusters from superficial layers are highlighted. **c**, Proportion of nuclei in each cluster that overlap between areas. MTG clusters *COL22A1* and *ESR1* map almost one-to-one with M1 clusters *OTOGL* and *LINC01202*, respectively. **d**, Estimated relative depth from pia of M1 glutamatergic clusters and closest matching MTG neurons based on similarity of integrated expression. Mean (points) and standard deviation (bars) of the dissected layer are shown for each cluster and approximate layer boundaries are indicated for M1 and MTG. **e**, Magnified view of L4-like clusters in M1 and MTG. Note that MTG clusters *FILIP1L* and *TWIST2* have little overlap with any M1 clusters. **f**, Overlap of M1 and MTG clusters in integrated space identifies two one-to-one cell type homologies and two MTG-specific clusters. **g**, ISH labeling of MTG and M1 clusters quantifies differences in layer distributions for homologous types between cortical areas. Cells (red dots) in each cluster were labeled using the markers listed below each representative

002 inverted image of a DAPI-stained cortical column. **h**, ISH estimated frequencies of homologous clusters

003 shows M1 has a 4-fold sparser L4-like type and similarly rare deep L3 type.

004

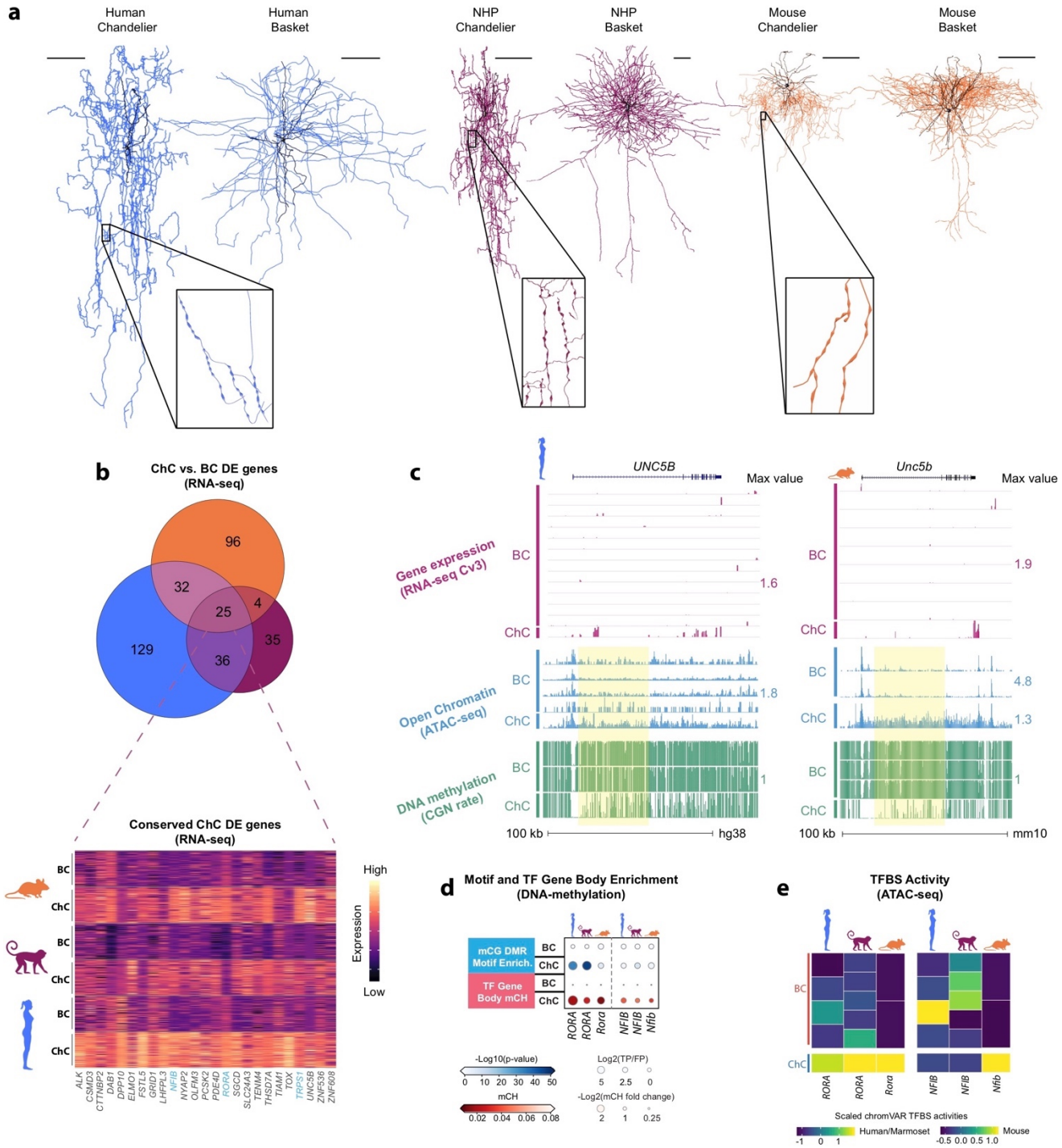

Figure 6. Chandelier neurons have a core set of conserved molecular features. a, Representative ultrastructure reconstructions of a ChC and BC from human (left), macaque (middle), and mouse (right). Insets show higher magnification of ChC axon cartridges. Macaque reconstructions were from source data available in Neuromorpho [63,64]. Mouse cells also appear in [65]. **b,** Venn diagram indicating

010 the number of shared ChC-enriched genes across species (top). DEGs were determined by a ROC test
011 of ChCs against BCs within a species. Heatmap showing scaled expression of the 25 conserved DEGs
012 in 100 randomly selected ChC and BC nuclei for each species (bottom); transcription factors are
013 colored in blue. **c**, Genome browser tracks showing *UNC5B* locus in human (left) and mouse (right)
014 ChCs and BCs. Tracks show aligned transcripts, regions of accessible chromatin, CGN methylation
015 rate, and CHN methylation rate. Yellow highlights mark examples of ChC-enriched regions of
016 accessible chromatin with hypo-methylated CGN. **d,** Heatmaps of TF gene body hypo-methylation
017 (mCH) state (bottom half, red) and genome-wide enrichment of TF motif across mCG DMRs in ChCs
018 and BCs (top half, blue). **e,** Scaled TFBS activities identified from SNARE-seq2 for human and
019 marmoset according to the scheme in Figure 4i and from mouse snATAC-seq data, using genes
020 enriched in ChC versus BC (Supplementary Table 19). Rows correspond to BC and ChC clusters
021 identified in snATAC-seq and SNARE-seq2 datasets.
022

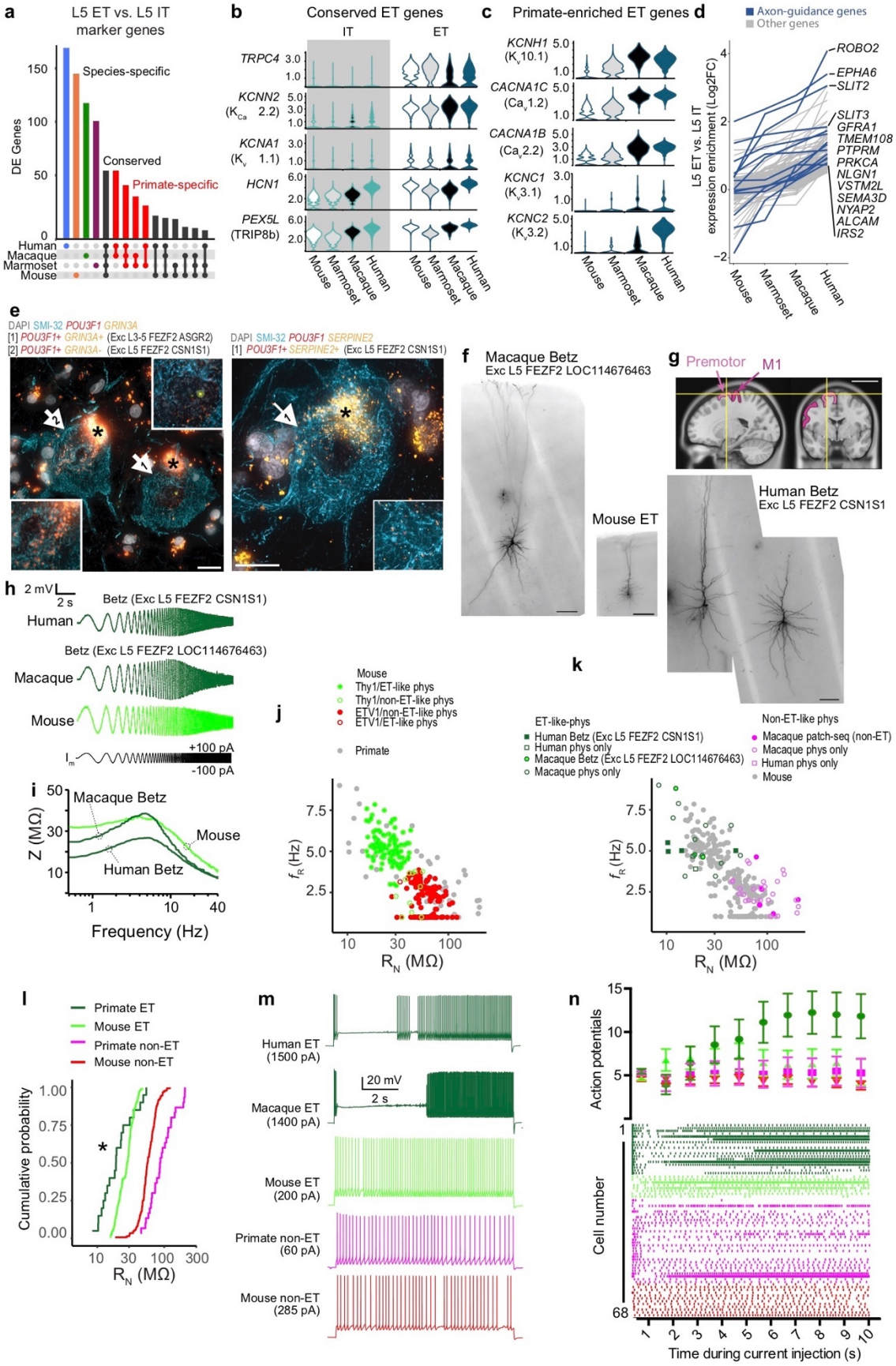
a
L5 ET vs. L5 IT marker genes
DE Genes
Species-specific
Conserved
Primate-specific
Human
Macaque
Marmoset
Mouse
b
Conserved ET genes
IT
ET
TRPC4
KCNN2 (K_Ca 2.2)
KCNA1 (K_v 1.1)
HCN1
PEX5L (TRIP8b)
Mouse
Marmoset
Macaque
Human
c
Primate-enriched ET genes
KCNH1 (K_v10.1)
CACNA1C (Ca_v1.2)
CACNA1B (Ca_v2.2)
KCNC1 (K_v3.1)
KCNC2 (K_v3.2)
d
Axon-guidance genes
Other genes
L5 ET vs. L5 IT expression enrichment (Log2FC)
ROBO2
EPHA6
SLIT2
SLIT3
GFRA1
TMEM108
PTPRM
PRKCA
NLGN1
VSTM2L
SEMA3D
NYAP2
ALCAM
IRS2
e
DAPI SMI-32 POU3F1 GRIN3A
[1] POU3F1+ GRIN3A+ (Exc L3-5 FEZF2 ASGR2)
[2] POU3F1+ GRIN3A- (Exc L5 FEZF2 CSN1S1)
DAPI SMI-32 POU3F1 SERPINE2
[1] POU3F1+ SERPINE2+ (Exc L5 FEZF2 CSN1S1)
f
Macaque Betz
Exc L5 FEZF2 LOC114676463
Mouse ET
g
Premotor
M1
Human Betz
Exc L5 FEZF2 CSN1S1
h
2 mV
2 s
Betz (Exc L5 FEZF2 CSN1S1)
Human
Betz (Exc L5 FEZF2 LOC114676463)
Macaque
Mouse
+100 pA
-100 pA
i
Macaque Betz
Mouse
Human Betz
Z (MΩ)
Frequency (Hz)
j
Mouse
Thy1/ET-like phys
Thy1/non-ET-like phys
ETV1/non-ET-like phys
ETV1/ET-like phys
Primate
f_R (Hz)
R_N (MΩ)
k
ET-like-phys
Human Betz (Exc L5 FEZF2 CSN1S1)
Human phys only
Macaque Betz (Exc L5 FEZF2 LOC114676463)
Macaque phys only
Non-ET-like phys
Macaque patch-seq (non-ET)
Macaque phys only
Human phys only
Mouse
f_R (Hz)
R_N (MΩ)
l
Primate ET
Mouse ET
Primate non-ET
Mouse non-ET
Cumulative probability
R_N (MΩ)
m
Human ET (1500 pA)
20 mV
2 s
Macaque ET (1400 pA)
Mouse ET (200 pA)
Primate non-ET (60 pA)
Mouse non-ET (285 pA)
n
Action potentials
Cell number
Time during current injection (s)

023

024 **Figure 7. Betz cells have specialized molecular and physiological properties. a,** Upset plot
025 showing conserved and divergent L5 ET glutamatergic neuron marker genes. DEGs were determined
026 by performing a ROC test between L5 ET and L5 IT within each species. **b, c,** Violin plots of ion
027 channel-related gene expression for genes that are enriched in (**b**) ET versus IT neurons and in (**c**)
028 primate versus mouse ET neurons. Protein names are in parentheses. **d,** Line graph of 131 genes with
029 expression enrichment in L5 ET versus IT neurons in human (>0.5 $\log_2$ fold-change) that decreases
030 with evolutionary distance from human. **e,** Two example photomicrographs of ISH labeled, SMI-32 IF
031 stained Betz cells in L5 human M1. Cells corresponding to two L5 ET clusters are labeled based on two
032 sets of marker genes. Insets show higher magnification of ISH in corresponding cells. Asterisks mark
033 lipofuscin; scale bar, 20 µm. **f, g,** Exemplar biocytin fills obtained from patch-seq experiments in
034 human, macaque and mouse brain slices. The example human and macaque neurons mapped to a
035 Betz cell transcriptomic cell type. Scale bars, 200 µm. **g,** MRI image in sagittal and coronal planes and
036 approximate location of excised premotor cortex tissue (yellow lines) and adjacent M1. **h,** Voltage
037 responses to a chirp stimulus for the neurons shown in **f** and **g** (left human neuron). **i,** Corresponding
038 ZAP profiles. All neurons were clustered into putative ET and non-IT neurons based upon their
039 resonant frequency and input resistance. **j,** For mouse L5 neurons (*Thy1*-YFP line H, n=117; *Etv1*-
040 EGFP line, n=123; unlabeled, n=21) 99.2 % of neurons in the *Etv1*-EGFP line possessed non-ET-like
041 physiology, whereas, 91.4% of neurons in the *Thy1*-YFP line H had ET-like physiology. **k,** For primate
042 L5 neurons (human, n=8, macaque n=42), all transcriptomically-defined Betz cells (human, n=4,
043 macaque n=3) had ET-like physiology (human n=6, macaque, n=14), whereas all transcriptomically-
044 defined non-ET neurons (human n=2, macaque n=3) had non-ET like physiology (human n=2,
045 macaque n=28). **l,** Cumulative probability distribution of L5 neuron input resistance for primate versus
046 mouse. * p = 0.0064, Kolmogorov-Smirnov test between mouse and primate ET neurons. **m,** Example
047 voltage responses to 10s step current injections for monkey, mouse and human ET and non-ET
048 neurons. The amplitude of the current injection was adjusted to produce ~5 spikes during the first
049 second. **n**, Raster plot (below) and average firing rate (above) during 1 s epochs during the 10s DC

current injection. Primate ET neurons (pooled data from human and macaque) displayed a distinctive decrease followed by a pronounced increase in firing rate over the course of the current injection. Notably, a similar biphasic-firing pattern is observed in macaque corticospinal neurons *in vivo* during prolonged motor movements [66], suggesting that the firing pattern of these neurons during behavior is intimately tied to their intrinsic membrane properties.

056 # Methods

057 ***Ethical compliance***

058 Postmortem adult human brain tissue was collected after obtaining permission from decedent next-of-
059 kin. Postmortem tissue collection was performed in accordance with the provisions of the United States
060 Uniform Anatomical Gift Act of 2006 described in the California Health and Safety Code section 7150
061 (effective 1/1/2008) and other applicable state and federal laws and regulations. The Western
062 Institutional Review Board reviewed tissue collection processes and determined that they did not
063 constitute human subjects research requiring institutional review board (IRB) review.

064

065 ***Postmortem human tissue specimens***

066 Male and female donors 18–68 years of age with no known history of neuropsychiatric or neurological
067 conditions ('control' cases) were considered for inclusion in the study (Extended Data Table 1). Routine
068 serological screening for infectious disease (HIV, Hepatitis B, and Hepatitis C) was conducted using
069 donor blood samples and only donors negative for all three tests were considered for inclusion in the
070 study. Only specimens with RNA integrity (RIN) values ≥7.0 were considered for inclusion in the study.
071 Postmortem brain specimens were processed as previously described [2]. Briefly, coronal brain slabs
072 were cut at 1cm intervals and frozen for storage at -80°C until the time of further use. Putative hand and
073 trunk-lower limb regions of the primary motor cortex were identified, removed from slabs of interest, and
074 subdivided into smaller blocks. One block from each donor was processed for cryosectioning and
075 fluorescent Nissl staining (Neurotrace 500/525, ThermoFisher Scientific). Stained sections were
076 screened for histological hallmarks of primary motor cortex. After verifying that regions of interest
077 contained M1, blocks were processed for nucleus isolation as described below.

078

079 ***Human RNA-sequencing, QC and clustering***

080 SMART-seq v4 nucleus isolation and sorting. Vibratome sections were stained with fluorescent Nissl
081 permitting microdissection of individual cortical layers (dx.doi.org/10.17504/protocols.io.7aehibe).
082 Nucleus isolation was performed as previously described (dx.doi.org/10.17504/protocols.io.ztqf6mw).
083 NeuN staining was carried out using mouse anti-NeuN conjugated to PE (FCMAB317PE, EMD
084 Millipore) at a dilution of 1:500. Control samples were incubated with mouse IgG1k-PE Isotype control
085 (BD Biosciences, 555749). DAPI (4',6-diamidino-2-phenylindole dihydrochloride, ThermoFisher
086 Scientific, D1306) was applied to nuclei samples at a concentration of 0.1µg/ml. Single-nucleus sorting
087 was carried out on either a BD FACSAria II SORP or BD FACSAria Fusion instrument (BD
088 Biosciences) using a 130 µm nozzle. A standard gating strategy based on DAPI and NeuN staining was
089 applied to all samples as previously described [2]. Doublet discrimination gates were used to exclude
090 nuclei aggregates.
091
092 SMART-seq v4 RNA-sequencing. The SMART-Seq v4 Ultra Low Input RNA Kit for Sequencing (Takara
093 #634894) was used per the manufacturer's instructions. Standard controls were processed with each
094 batch of experimental samples as previously described. After reverse transcription, cDNA was amplified
095 with 21 PCR cycles. The NexteraXT DNA Library Preparation (Illumina FC-131-1096) kit with
096 NexteraXT Index Kit V2 Sets A-D (FC-131-2001, 2002, 2003, or 2004) was used for sequencing library
097 preparation. Libraries were sequenced on an Illumina HiSeq 2500 instrument using Illumina High
098 Output V4 chemistry.
099
100 SMART-seq v4 gene expression quantification. Raw read (fastq) files were aligned to the GRCh38
101 human genome sequence (Genome Reference Consortium, 2011) with the RefSeq transcriptome
102 version GRCh38.p2 (current as of 4/13/2015) and updated by removing duplicate Entrez gene entries
103 from the gtf reference file for STAR processing. For alignment, Illumina sequencing adapters were
104 clipped from the reads using the fastqMCF program. After clipping, the paired-end reads were mapped
105 using Spliced Transcripts Alignment to a Reference (STAR) using default settings. Reads that did not

106 map to the genome were then aligned to synthetic construct (i.e. ERCC) sequences and the *E. coli*
107 genome (version ASM584v2). Quantification was performed using summerizeOverlaps from the R
108 package GenomicAlignments. Expression levels were calculated as counts per million (CPM) of exonic
109 plus intronic reads.
110
111 10x Chromium RNA-sequencing. Nucleus isolation for 10x Chromium RNA-sequencing was conducted
112 as described (dx.doi.org/10.17504/protocols.io.y6rfzd6). After sorting, single-nucleus suspensions were
113 frozen in a solution of 1X PBS, 1% BSA, 10% DMSO, and 0.5% RNAsin Plus RNase inhibitor
114 (Promega, N2611) and stored at -80°C. At the time of use, frozen nuclei were thawed at 37°C and
115 processed for loading on the 10x Chromium instrument as described
116 (dx.doi.org/10.17504/protocols.io.nx3dfqn). Samples were processed using the 10x Chromium Single-
117 Cell 3' Reagent Kit v3. 10x chip loading and sample processing was done according to the
118 manufacturer's protocol. Gene expression was quantified using the default 10x Cell Ranger v3 pipeline
119 except substituting the curated genome annotation used for SMART-seq v4 quantification. Introns were
120 annotated as "mRNA", and intronic reads were included in expression quantification.
121
122 Quality control of RNA-seq data. Nuclei were included for analysis if they passed all QC criteria.
123 SMART-seq v4 criteria:
124 > 30% cDNA longer than 400 base pairs
125 > 500,000 reads aligned to exonic or intronic sequence
126 > 40% of total reads aligned
127 > 50% unique reads
128 > 0.7 TA nucleotide ratio
129 Cv3 criteria:
130 > 500 (non-neuronal nuclei) or > 1000 (neuronal nuclei) genes detected
131 < 0.3 doublet score

132

133 Clustering RNA-seq data. Nuclei passing QC criteria were grouped into transcriptomic cell types using
134 a previously reported iterative clustering procedure (Tasic et al. 2018; Hodge, Bakken et al., 2019).
135 Briefly, intronic and exonic read counts were summed, and $\log_2$-transformed expression was centered
136 and scaled across nuclei. X- and Y-chromosomes and mitochondrial genes were excluded to avoid
137 nuclei clustering based on sex or nuclei quality. DEGs were selected, principal components analysis
138 (PCA) reduced dimensionality, and a nearest neighbor graph was built using up to 20 principal
139 components. Clusters were identified with Louvain community detection (or Ward's hierarchical
140 clustering if N < 3000 nuclei), and pairs of clusters were merged if either cluster lacked marker genes.
141 Clustering was applied iteratively to each subcluster until clusters could not be further split.

142

143 Cluster robustness was assessed by repeating iterative clustering 100 times for random subsets of
144 80% of nuclei. A co-clustering matrix was generated that represented the proportion of clustering
145 iterations that each pair of nuclei were assigned to the same cluster. We defined consensus clusters by
146 iteratively splitting the co-clustering matrix as described (Tasic et al. 2018; Hodge, Bakken et al., 2019).
147 The clustering pipeline is implemented in the R package “scrattch.hicat”, and the clustering method is
148 provided by the “run_consensus_clust” function (https://github.com/AllenInstitute/scrattch.hicat).

149

150 Clusters were curated based on QC criteria or cell class marker expression (*GAD1*, *SLC17A7*,
151 *SNAP25*). Clusters were identified as donor-specific if they included fewer nuclei sampled from donors
152 than expected by chance. To confirm exclusion, clusters automatically flagged as outliers or donor-
153 specific were manually inspected for expression of broad cell class marker genes, mitochondrial genes
154 related to quality, and known activity-dependent genes.

155

156 ***Marmoset sample processing and nuclei isolation***

157 Marmoset experiments were approved by and in accordance with Massachusetts Institute of
158 Technology IACUC protocol number 051705020. Two adult marmosets (2.3 and 3.1 years old; one
159 male, one female; Extended Data Table 2) were deeply sedated by intramuscular injection of ketamine
160 (20-40 mg/kg) or alfaxalone (5-10 mg/kg), followed by intravenous injection of sodium pentobarbital
161 (10–30 mg/kg). When pedal withdrawal reflex was eliminated and/or respiratory rate was diminished,
162 animals were transcardially perfused with ice-cold sucrose-HEPES buffer. Whole brains were rapidly
163 extracted into fresh buffer on ice. Sixteen 2-mm coronal blocking cuts were rapidly made using a
164 custom-designed marmoset brain matrix. Coronal slabs were snap-frozen in liquid nitrogen and stored
165 at -80°C until use.
166
167 As with human samples, M1 was isolated from thawed slabs using fluorescent Nissl staining
168 (Neurotrace 500/525, ThermoFisher Scientific). Stained sections were screened for histological
169 hallmarks of primary motor cortex. Nuclei were isolated from the dissected regions following this
170 protocol: https://www.protocols.io/view/extraction-of-nuclei-from-brain-tissue-2srged6 and processed
171 using the 10x Chromium Single-Cell 3' Reagent Kit v3. 10x chip loading and sample processing was
172 done according to the manufacturer's protocol.
173
174 ***Marmoset RNA-sequencing, QC and clustering***
175 RNA-sequencing. Libraries were sequenced on NovaSeq S2 instruments (Illumina). Raw sequencing
176 reads were aligned to calJac3. Mitochondrial sequence was added into the published reference
177 assembly. Human sequences of RNR1 and RNR2 (mitochondrial) and RNA5S (ribosomal), were
178 aligned using gmap to the marmoset genome and added to the calJac3 annotation. Reads that mapped
179 to exons or introns of each assembly were assigned to annotated genes. Libraries were sequenced to a
180 median read depth of 5.95 reads per unique molecular index (UMI). The alignment pipeline can be
181 found at https://github.com/broadinstitute/Drop-seq.
182

183 Cell filtering. Cell barcodes were filtered to distinguish true nuclei barcodes from empty beads and PCR
184 artifacts by assessing proportions of ribosomal and mitochondrial reads, ratio of intronic/exonic reads (>
185 50% of intronic reads), library size (> 1000 UMIs) and sequencing efficiency (true cell barcodes have
186 higher reads/UMI). The resulting digital gene expression matrix (DGE) from each library was carried
187 forward for clustering.
188
189 Clustering. Clustering analysis proceeded as in Krienen et al (2019, bioRxiv). Briefly, independent
190 component analysis. (ICA, using the fastICA package in R) was performed jointly on all marmoset
191 DGEs after normalization and variable gene selection as in (Saunders et al 2018, *Cell*). The first-round
192 clustering resulted in 15 clusters corresponding to major cell classes (neurons, glia, endothelial). Each
193 cluster was curated as in (Saunders et al 2018, *Cell*) to remove doublets and outliers. Independent
194 components (ICs) were partitioned into those reflecting artifactual signals (e.g. those for which cell
195 loading indicated replicate or batch effects). Remaining ICs were used to determine clustering (Louvain
196 community detection algorithm igraph package in R); for each cluster nearest neighbor and resolution
197 parameters were set to optimize 1:1 mapping between each IC and a cluster.
198
199 ***Mouse snRNA-seq data generation and analysis***
200 Single-nuclei were isolated from mouse primary motor cortex, gene expression was quantified using
201 Cv3 and SSv4 RNA-sequencing, and transcriptomic cell types and dendrogram were defined as
202 described in a companion paper [6].
203
204 ***Integrating and clustering human Cv3 and SSv4 snRNA-seq datasets***
205 To establish a set of human consensus cell types, we performed a separate integration of snRNA-seq
206 technologies on the major cell classes (Glutamatergic, GABAergic, and Non-neuronal). Broadly, this
207 integration is comprised of 6 steps: (1) subsetting the major cell class from each technology (e.g. Cv3
208 GABAergic and SSv4 GABAergic); (2) finding marker genes for all clusters within each technology; (3)

integrating both datasets with Seurat's standard workflow using marker genes to guide integration (Seurat 3.1.1); (4) overclustering the data to a greater number of clusters than were originally identified within a given individual dataset; (5) finding marker genes for all integrated clusters; and (6) merging similar integrated clusters together based on marker genes until all merging criteria were sufficed, resulting in the final human consensus taxonomy.

More specifically, each expression matrix was $\log_2$(CPM + 1) transformed then placed into a Seurat object with accompanying metadata. Variable genes were determined by downsampling each expression matrix to a maximum of 300 nuclei per scrattch.hicat-defined cluster (from a previous step; see scrattch.hicat clustering) and running select_markers (scrattch.io 0.1.0) with n set to 20, to generate a list of up to 20 marker genes per cluster. The union of the Cv3 and SSv4 gene lists were then used as input for anchor finding, dimensionality reduction, and Louvain clustering of the full expression matrices. We used 100 dimensions for steps in the workflow, and 100 random starts during clustering. Louvain clustering was performed to overcluster the dataset to identify more integrated clusters than the number of scrattch.hicat-defined clusters. For example, GABAergic neurons had 79 and 37 scrattch.hicat-defined clusters, 225 overclustered integrated clusters, and 72 final human consensus clusters after merging for Cv3 and SSv4 datasets, respectively. To merge the overclustered integrated clusters, up to 20 marker genes were found for each cluster to establish the neighborhoods of the integrated dataset. Clusters were then merged with their nearest neighbor if there were not a minimum of ten Cv3 and two SSv4 nuclei in a cluster, and a minimum of 4 DEGs that distinguished the query cluster from the nearest neighbor (note: these were the same parameters used to perform the initial scrattch.hicat clustering of each dataset).

Integrating and clustering MTG and M1 SSv4 snRNA-seq datasets

To compare cell types between our M1 human cell type taxonomy and our previously described human MTG taxonomy [2], we used Seurat's standard integration workflow to perform a supervised integration

235 of the M1 and MTG SSv4 datasets. Intronic and exonic reads were summed into a single expression
236 matrix for each dataset, CPM normalized, and placed into a Seurat object with accompanying
237 metadata. All nuclei from each major cell class were integrated and clustered separately. Up to 100
238 marker genes for each cluster within each dataset were identified, and the union of these two gene lists
239 was used as input to guide alignment of the two datasets during integration, dimensionality reduction,
240 and clustering steps. We used 100 dimensions for all steps in the workflow.
241
242 ***Integrating Cv3 snRNA-seq datasets across species***
243 To identify homologous cell types across species, we used Seurat's SCTransform workflow to perform
244 a separate supervised integration on each cell class across species. Raw expression matrices were
245 reduced to only include genes with one-to-one orthologs defined in the three species (14,870 genes;
246 downloaded from NCBI Homologene in November, 2019) and placed into Seurat objects with
247 accompanying metadata. To avoid having one species dominate the integrated space and to account
248 for potential differences in each species' clustering resolution, we downsampled the number of nuclei to
249 have similar numbers across species at the subclass level (e.g. *Lamp5*, *Sst*, L2/3 IT, L6b, etc.). The
250 species with the largest number of clusters under a given subclass was allowed a maximum of 200
251 nuclei per cluster. The remaining species then split this theoretical maximum (200 nuclei times the max
252 number of clusters under subclass) evenly across their clusters. For example, the L2/3 IT subclass had
253 8, 4, and 3 clusters for human, marmoset, and mouse, respectively. All species were allowed a
254 maximum of 1600 L2/3 IT nuclei total; or a maximum of 200 human, 400 marmoset, and 533 mouse
255 nuclei per cluster. To integrate across species, all Seurat objects were merged and normalized using
256 Seurat's SCTransform function. To better guide the alignment of cell types from each species, we found
257 up to 100 marker genes for each cluster within a given species. We used the union of these gene lists
258 as input for integration and dimensionality reduction steps, with 30 dimensions used for integration and
259 100 for dimensionality reduction and clustering. Clustering the human-marmoset-mouse integrated
260 space provided an additional quality control mechanism, revealing numerous small, species-specific

integrated clusters that contained only low-quality nuclei (low UMIs and genes detected). We excluded 4836 nuclei from the marmoset dataset that constituted low-quality integrated neuronal clusters.

To identify which clusters in our three species taxonomy aligned with macaque clusters from our L5 dissected Cv3 dataset, we performed an identical integration workflow on Glutamatergic neurons as was used for the three species integration. Macaque clusters were assigned subclass labels based on their corresponding alignment with subclasses from the other species. The annotated L5 dissected macaque Cv3 dataset was then used as a reference for mapping macaque patch-seq nuclei (see section below).

Estimation of cell type homology

To identify homologous groups from different species, we applied a tree-based method (https://github.com/AllenInstitute/BICCN_M1_Evo and package: https://github.com/huqiwen0313/speciesTree). In brief, the approach consists of 4 steps: 1) metacell clustering, 2) hierarchical reconstruction of a metacell tree, 3) measurements of species mixing and stability of splits and 4) dynamic pruning of the hierarchical tree.

Firstly, to reduce noise in single-cell datasets and to remove species-specific batch effects, we clustered cells into small highly similar groups based on the integrated matrix generated by Seurat, as described in the previous section. These cells were further aggregated into metacells and the expression values of the metacells were calculated by averaging the gene expression of individual cells that belong to each metacell. Correlation was calculated based on the metacell gene expression matrix to infer the similarity of each metacell cluster. Then hierarchical clustering was performed based on the metacell gene expression matrix using Ward's method. For each node or corresponding branch in the hierarchical tree, we calculated 3 measurements, and the hierarchical tree was visualized based on these measurements: 1) Cluster size visualized as the thickness of branches in the tree; 2) Species

mixing calculated based on entropy of the normalized cell distribution and visualized as the color of each node and branch; 3) Stability of each node. The entropy of cells was calculated as: $H = -\sum_i p_i log p_i$, where p_i is the probability of cells from one species appearing among all the cells in a node. We assessed the node stability by evaluating the agreement between the original hierarchical tree and a result on a subsampled dataset calculated based on the optimal subtree in the subsampled hierarchical trees derived from subsampling 95% of cells in the original dataset. The entire subsampling process was repeated 100 times and the mean stability score for every node in the original tree was calculated. Finally, we recursively searched each node in the tree. If the heuristic criteria (see below) were not met for any node below the upper node, the entire subtree below the upper node was pruned and all the cells belonging to this subtree were merged into one homologous group.

To identify robust homologous groups, we applied criteria in two steps to dynamically search the cross-species tree. Firstly, for each node in the tree, we computed the mixing of cells from 3 species based on entropy and set it as a tuning parameter. For each integrated tree, we tuned the entropy parameter to make sure the tree method generated the highest resolution of homologous clusters without losing the ability to identify potential species-specific clusters. Nodes with entropy larger than 2.9 (for inhibitory neurons) or 2.75 (for excitatory neurons) were considered as well-mixed nodes. For example, an entropy of 2.9 corresponded to a mixture of human, marmoset, and mouse equal to (0.43, 0.37, 0.2) or (0.38, 0.30, 0.32). We recursively searched all the nodes in the tree until we found the node nearest the leaves of the tree that was well-mixed among species, and this node was defined as a well-mixed upper node. Secondly, we further checked the within-species cell composition for the subtrees below the well-mixed upper node to determine if further splits were needed. For the cells on the subtrees below the well mixed upper node, we measured the purity of within-species cell composition by calculating the percentage of cells that fall into a specific sub-group in each individual species. If the purity for any species was larger than 0.8, we went one step further below the well mixed upper node so that its children were selected. Any branches below these nodes (or well-mixed upper node if the

312 within-species cell composition criteria was not met) were pruned and cells from these nodes were
313 merged into the same homologous groups, then the final integrated tree was generated.
314 As a final curation step, the homologous groups generated by the tree method were merged to be
315 consistent with within-species clusters. We defined consensus types by comparing the overlap of
316 within-species clusters between human and marmoset and human and mouse, as previously described
317 [2]. For each pair of human and mouse clusters and human and marmoset clusters, the overlap was
318 defined as the sum of the minimum proportion of nuclei in each cluster that overlapped within each leaf
319 of the pruned tree. This approach identified pairs of clusters that consistently co-clustered within one or
320 more leaves. Cluster overlaps varied from 0 to 1 and were visualized as a heatmap with human M1
321 clusters in rows and mouse or marmoset M1 clusters in columns. Cell type homologies were identified
322 as one-to-one, one-to-many, or many-to many so that they were consistent in all three species. For
323 example, the Vip_2 consensus type could be resolved into multiple homologous types between human
324 and marmoset but not human and mouse, and the coarser homology was retained. Consensus type
325 names were assigned based on the annotations of member clusters from human and mouse and
326 avoided specific marker gene names due to the variability of marker expression across species.
327
328 To quantify cell type alignment between pairs of species, we pruned the hierarchical tree described
329 above based on the stability and mixing of two species. We performed this analysis for human-
330 marmoset, human-mouse, and marmoset-mouse and compared the alignment resolution of each
331 subclass. The pruning criteria were tuned to fit the two-species comparison and to remove bias, and we
332 set the same criteria for all comparisons (entropy cutoff 3.0). Specifically, for each subclass and
333 pairwise species comparison, we calculated the number of leaves in the pruned tree. We repeated this
334 analysis on the 100 subsampled datasets and calculated the mean and standard deviation of the
335 number of leaves in the pruned trees. For each subclass, we tested for significant differences in the
336 average number of leaves across pairs of species using an ANOVA test followed by post-hoc Tukey
337 HSD tests.

338

339 ***Marker determination for cell type clusters by NS-Forest v2.1***

340 NS-Forest v2.1 was used to determine the minimum set of marker genes whose combined expression
341 identified cells of a given type with maximum classification accuracy (T. Bakken et al. 2017; Aevermann
342 et al. 2018). (https://github.com/JCVenterInstitute/NSForest/releases). Briefly, for each cluster NS-
343 Forest produces a Random Forest (RF) model using a one vs all binary classification approach. The
344 top ranked genes from RF are then filtered by expression level to retain genes that are expressed in at
345 least 50% of the cells within the target cluster. The selected genes are then reranked by Binary Score
346 calculated by first finding median cluster expression values for a given gene and dividing by the target
347 median cluster expression value. Next, one minus this scaled value is calculated resulting in 0 for the
348 target cluster and 1 for clusters that have no expression, while negative scaled values are set to 0.
349 These values are then summed and normalized by dividing by the total number of clusters. In the ideal
350 case, where all off-target clusters have no expression, the binary score is 1. Finally, for the top 6 binary
351 genes optimal expression level cutoffs are determined and all permutations of genes are evaluated by
352 f-beta score, where the beta is weighted to favor precision. This f-beta score indicates the power of
353 discrimination for a cluster and a given set of marker genes. The gene combination giving the highest f-
354 beta score is selected as the optimal marker gene combination. Marker gene sets for human, mouse
355 and marmoset primary motor cortex are listed in Supplementary Tables 4, 5, and 6, respectively, and
356 were used to construct the semantic cell type definitions provided in Supplementary Table 1.

357

358 ***Calculating differentially expressed genes (DEGs)***

359 To identify subclass level DEGs that are conserved and divergent across species, we used the
360 integrated Seurat objects from the species integration step. Seurat objects for each major cell class
361 were downsampled to have up to 200 cells per species cell type. Positive DEGs were then found using
362 Seurat's `FindAllMarkers` function using the ROC test with default parameters. We compared each
363 subclass within species to all remaining nuclei in that class and used the SCT normalized counts to test

364 for differential expression. For example, human *Sst* nuclei were compared to all other GABAergic
365 human neurons using the ROC test. Venn diagrams were generated using the eulerr package (6.0.0) to
366 visualize the relationship of DEGs across species for a given subclass. Heatmaps of DEGs for all
367 subclasses under a given class were generated by downsampling each subclass to 50 random nuclei
368 per species. SCT normalized counts were then scaled and visualized with Seurat's `DoHeatmap`
369 function.
370
371 To identify ChC DEGs that are enriched over BCs, we used the integrated Seurat objects from the
372 species integration step. The *Pvalb* subclass was subset and species cell types were then designated
373 as either ChCs or BCs. Positive DEGs were then found using Seurat's `FindAllMarkers` function
374 using the ROC test to compare ChCs and BCs for each species. Venn diagrams were generated using
375 the eulerr package (6.0.0) to visualize the relationship of ChC-enriched DEGs across species.
376 Heatmaps of conserved DEGs were generated by downsampling the dataset to have 100 randomly
377 selected BCs and ChCs from each species. SCT normalized counts were then scaled and visualized
378 with Seurat's `DoHeatmap` function.
379
380 We used the four species (human, macaque, marmoset, and mouse) integrated Glutamatergic Seurat
381 object from the species integration step for all L5 ET DEG figures. L5 ET and L5 IT subclasses were
382 downsampled to 200 randomly selected nuclei per species. A ROC test was then performed using
383 Seurat's `FindAllMarkers` function between the two subclasses for each species to identify L5 ET-
384 specific marker genes. We then used the UpSetR (1.4.0) package to visualize the intersections of the
385 marker genes across all four species as an upset plot. To determine genes that decrease in expression
386 across evolutionary distance in L5 ET neurons, we found the log-fold change between L5 ET and L5 IT
387 for each species across all genes. We then filtered the gene lists to only include genes that had a trend
388 of decreasing log-fold change (human > macaque > marmoset > mouse). Lastly, we excluded any gene

389 that did not have a log-fold change of 0.5 or greater in the human comparison. These 131 genes were
390 then used as input for GO analysis with the PANTHER Classification System [67] for the biological
391 process category, with organism set to Homo sapiens. All significant GO terms for this gene list were
392 associated with cell-cell adhesion and axon-guidance, and are colored blue in the line graph of their
393 expression enrichment.
394
395 ***Estimating differential isoform usage between human and mouse***
396 To assess changes of isoform usage between mouse and human, we used SSv4 data with full
397 transcript coverage and estimated isoform abundance in each cell subclasses. To mitigate low read
398 depth in each cell, we aggregated reads from all cells in each subclass. We estimated the relative
399 isoform usage in each subclass by calculating its genic proportion (P), defined as the ratio (R) of
400 isoform expression to the gene expression, where $R = (P_{human} - P_{mouse}) / (P_{human} + P_{mouse})$. For a common
401 set of transcripts for mouse and human, we used UCSC browser TransMapV5 set of human transcripts
402 (hg38 assembly, Gencode v31 annotations) mapped to the mouse genome (mm10 assembly)
403 http://hgdownload.soe.ucsc.edu/gbdb/mm10/transMap/V5/mm10.ensembl.transMapV5.bigPsl. We
404 considered only medium to highly expressed isoforms, which have abundance > 10 TPM (Transcripts
405 per Million) and P > 0.2 in either mouse or human and gene expression > 10 TPM in both mouse and
406 human.
407
408 Calculating isoform abundance in each cell subclass:
409 1) Aggregated reads from each subclass
410 2) Mapped reads to the mouse or human reference genome with STAR 2.7.3a using default
411 parameters
412 3) Transformed genomic coordinates into transcriptomic coordinates using STAR parameter: --
413 quantMode TranscriptomeSAM

4) Quantified isoform and gene expression using RSEM 1.3.3 parameters: --bam --seed 12345 --paired-end --forward-prob 0.5 --single-cell-prior --calc-ci

Estimating statistical significance:

1) Calculated the standard deviation of isoform genic proportion (P_{human} and P_{mouse}) from the RSEM's 95% confidence intervals of isoform expression
2) Calculated the P-value using normal distribution for the (P_{human} - P_{mouse}) and the summed (mouse + human) variance
3) Bonferroni-adjusted P-values by multiplying nominal P-values by the number of medium to highly expressed isoforms in each subclass

Species cluster dendrograms

DEGs for a given species were identified using Seurat's `FindAllMarkers` function with a Wilcox test and comparing each cluster to every other cluster under the same subclass, with logfc.threshold set to 0.7 and min.pct set to 0.5. The union of up to 100 genes per cluster with the highest avg_logFC were used.The average $\log_2$ expression of the DEGs were then used as input for the `build_dend` function from scrattch.hicat to create the dendrograms. This was performed on both human and marmoset datasets. For mouse dendrogram methods, see the companion paper [6].

Multiplex fluorescent in situ hybridization (FISH)

Fresh-frozen human postmortem brain tissues were sectioned at 14-16 µm onto Superfrost Plus glass slides (Fisher Scientific). Sections were dried for 20 minutes at -20°C and then vacuum sealed and stored at -80°C until use. The RNAscope multiplex fluorescent v1 kit was used per the manufacturer's instructions for fresh-frozen tissue sections (ACD Bio), except that fixation was performed for 60 minutes in 4% paraformaldehyde in 1X PBS at 4°C and protease treatment was shortened to 5minutes. Primary antibodies were applied to tissues after completion of mFISH staining. Primary antibodies used

were mouse anti-GFAP (EMD Millipore, MAB360, 1:250 dilution) and mouse anti-Neurofilament H (SMI-32, Biolegend, 801701). Secondary antibodies were goat anti-mouse IgG (H+L) Alexa Fluor conjugates (594, 647). Sections were imaged using a 60X oil immersion lens on a Nikon TiE fluorescence microscope equipped with NIS-Elements Advanced Research imaging software (version 4.20). For all RNAscope mFISH experiments, positive cells were called by manually counting RNA spots for each gene. Cells were called positive for a gene if they contained ≥ 3 RNA spots for that gene. Lipofuscin autofluorescence was distinguished from RNA spot signal based on the larger size of lipofuscin granules and broad fluorescence spectrum of lipofuscin.

Gene family conservation

To investigate the conservation and divergence of gene family coexpression between primates and mouse, MetaNeighbor analysis [30] was performed using gene groups curated by the HUGO Gene Nomenclature Committee (HGNC) at the European Bioinformatics Institute (https://www.genenames.org; downloaded January 2020) and by the Synaptic Gene Ontology (SynGO) [68] (downloaded February 2020). HGNC annotations were propagated via the provided group hierarchy to ensure the comprehensiveness of parent annotations. Only groups containing five or more genes were included in the analysis.

After splitting data by class, MetaNeighbor was used to compare data at the cluster level using labels from cross-species integration with Seurat. Cross-species comparisons were performed at two levels of the phylogeny: 1) between the two primate species, marmoset and human; and 2) between mouse and primates. In the first case, the data from the two species were each used as the testing and training set across two folds of cross-validation, reporting the average performance (AUROC) across folds. In the second case, the primate data were used as an aggregate training set, and performance in mouse was reported. Results were compared to average within-species performance.

466 ***Replicability of clusters***

467 MetaNeighbor was used to provide a measure of neuronal subclass and cluster replicability within and
468 across species. For this application, we tested all pairs of species (human-marmoset, marmoset-
469 mouse, human-mouse) as well as testing within each species. After splitting the data by class, highly
470 variable genes were identified using the get_variable_genes function from MetaNeighbor, yielding 928
471 genes for GABAergic and 763 genes for Glutamatergic neuron classes, respectively. These were used
472 as input for the MetaNeighborUS function, which was run using the fast_version and one_vs_best
473 parameters set to TRUE. Using the one_vs_best parameter means that only the two closest
474 neighboring clusters are tested for their similarity to the training cluster, with results reported as the
475 AUROC for the closest neighbor over the second closest. AUROCs are plotted in heatmaps in
476 Extended Data Figures 2 and 3. Data to reproduce these figures can be found in Supplementary Table
477 9, and scripts are on GitHub (http://github.com/gillislab/MetaNeighbor).

478

479 ***Single-cell methylome data (snmC-seq2): Sequencing and quantification***

480 Library preparation and Illumina sequencing. Single nuclei were isolated from human and marmoset M1
481 tissue as described above for RNA-seq profiling and for mouse as detailed in [6]. Detailed methods for
482 bisulfite conversion and library preparation were previously described for snmC-seq2[5,41]. The snmC-
483 seq2 libraries generated from mouse brain tissues were sequenced using an Illumina Novaseq 6000
484 instrument with S4 flowcells and 150 bp paired-end mode.

485

486 Mapping and feature count pipeline. We implemented a versatile mapping pipeline (http://cemba-
487 data.rtfd.io) for all the single-cell methylome based technologies developed by our group [5,41,69]. The
488 main steps of this pipeline included: 1) demultiplexing FASTQ files into single-cell; 2) reads level QC; 3)
489 mapping; 4) BAM file processing and QC; and 5) final molecular profile generation. The details of the
490 five steps for snmC-seq2 were described previously [41]. We mapped all the reads from the three
491 corresponding species onto the human hg19 genome, the marmoset ASM275486v1 genome, and the

492 mouse mm10 genome. After mapping, we calculated the methyl-cytosine counts and total cytosine
493 counts for two sets of genome regions in each cell: the non-overlapping chromosome 100-kb bins of
494 each genome, the methylation levels of which were used for clustering analysis, and the gene body
495 regions, the methylation levels of which were used for cluster annotation and integration with RNA
496 expression data.
497
498 ***snmC-seq2: Quality control and preprocessing***
499 Cell filtering. We filtered the cells based on these main mapping metrics: 1) mCCC rate < 0.03. mCCC
500 rate reliably estimates the upper bound of bisulfite non-conversion rate [5]; 2) overall mCG rate > 0.5; 3)
501 overall mCH rate < 0.2; 4) total final reads > 500,000; and 5) bismark mapping rate > 0.5. Other metrics
502 such as genome coverage, PCR duplicates rate, and index ratio were also generated and evaluated
503 during filtering. However, after removing outliers with the main metrics 1-5, few additional outliers can
504 be found.
505
506 Feature filtering. 100kb genomic bin features were filtered by removing bins with mean total cytosine
507 base calls < 250 or > 3000. Regions overlap with the ENCODE blacklist [70] were also excluded from
508 further analysis.
509
510 Computation and normalization of the methylation rate. For CG and CH methylation, the computation of
511 methylation rate from the methyl-cytosine and total cytosine matrices contains two steps: 1) prior
512 estimation for the beta-binomial distribution and 2) posterior rate calculation and normalization per cell.
513 Step 1. For each cell we calculated the sample mean, m, and variance, v, of the raw mc rate *(mc / cov)*
514 for each sequence context (CG, CH). The shape parameters (α, β) of the beta distribution were then
515 estimated using the method of moments:
516 $$\alpha = m(m(1-m)/v - 1)$$
517 $$\beta = (1-m)(m(1-m)/v - 1)$$

518 This approach used different priors for different methylation types for each cell and used weaker prior to
519 cells with more information (higher raw variance).
520
521 Step 2. We then calculated the posterior: $\widehat{mc} = \frac{\alpha+mc}{\alpha+\beta+cov}$., We normalized this rate by the cell's global
522 mean methylation, $m = \alpha/(\alpha+\beta)$. Thus, all the posterior $\widehat{mc}$ with 0 *cov* will be constant 1 after
523 normalization. The resulting normalized *mc* rate matrix contains no NA (not available) value, and
524 features with less *cov* tend to have a mean value close to 1.
525
526 Selection of highly variable features. Highly variable methylation features were selected based on a
527 modified approach using the scanpy package *scanpy.pp.highly_variable_genes* function [71]. In brief, the
528 *scanpy.pp.highly_variable_genes* function normalized the dispersion of a gene by scaling with the
529 mean and standard deviation of the dispersions for genes falling into a given bin for mean expression of
530 genes. In our modified approach, we reasoned that both the mean methylation level and the mean *cov*
531 of a feature (100kb bin or gene) could impact *mc* rate dispersion. We grouped features that fall into a
532 combined bin of mean and *cov*, and then normalized the dispersion within each *mean-cov* group. After
533 dispersion normalization, we selected the top 3000 features based on normalized dispersion for
534 clustering analysis.
535
536 Dimension reduction and combination of different mC types. For each selected feature, *mc* rates were
537 scaled to unit variance, and zero mean. PCA was then performed on the scaled *mc* rate matrix. The
538 number of significant PCs was selected by inspecting the variance ratio of each PC using the elbow
539 method. The CH and CG PCs were then concatenated together for further analysis in clustering and
540 manifold learning.
541
542 ***snmC-seq2: Data analysis***

543 Consensus clustering on concatenated PCs. We used a consensus clustering approach based on
544 multiple Leiden-clustering [72] over K-Nearest Neighbor (KNN) graph to account for the randomness of
545 the Leiden clustering algorithms. After selecting dominant PCs from PCA in both mCH and mCG
546 matrix, we concatenated the PCs together to construct a KNN graph using *scanpy.pp.neighbors* with
547 Euclidean distance. Given fixed resolution parameters, we repeated the Leiden clustering 300 times on
548 the KNN graph with different random starts and combined these cluster assignments as a new feature
549 matrix, where each single Leiden result is a feature. We then used the outlier-aware DBSCAN
550 algorithm from the scikit-learn package to perform consensus clustering over the Leiden feature matrix
551 using the hamming distance. Different epsilon parameters of DBSCAN are traversed to generate
552 consensus cluster versions with the number of clusters that range from minimum to the maximum
553 number of clusters observed in the multiple Leiden runs. Each version contained a few outliers that
554 usually fall into three categories: 1) cells located between two clusters that had gradient differences
555 instead of clear borders; 2) cells with a low number of reads that potentially lack information in essential
556 features to determine the specific cluster; and 3) cells with a high number of reads that were potential
557 doublets. The amount of type 1 and 2 outliers depends on the resolution parameter and is discussed in
558 the choice of the resolution parameter section. The type 3 outliers were very rare after cell filtering. The
559 supervised model evaluation then determined the final consensus cluster version.
560
561 Supervised model evaluation on the clustering assignment. For each consensus clustering version, we
562 performed a Recursive Feature Elimination with Cross-Validation (RFECV) [73] process from the scikit-
563 learn package to evaluate clustering reproducibility. We first removed the outliers from this process,
564 and then we held out 10% of the cells as the final testing dataset. For the remaining 90% of the cells,
565 we used tenfold cross-validation to train a multiclass prediction model using the input PCs as features
566 and *sklearn.metrics.balanced_accuracy_score* [74] as an evaluation score. The multiclass prediction
567 model is based on *BalancedRandomForestClassifier* from the imblearn package that accounts for
568 imbalanced classification problems[75]. After training, we used the 10% testing dataset to test the model

performance using the *balanced_accuracy_score* score. We kept the best model and corresponding clustering assignments as the final clustering version. Finally, we used this prediction model to predict outliers' cluster assignments, we rescued the outlier with prediction probability > 0.3, otherwise labeling them as outliers.

Choice of resolution parameter. Choosing the resolution parameter of the Leiden algorithm is critical for determining the final number of clusters. We selected the resolution parameter by three criteria: 1. The portion of outliers < 0.05 in the final consensus clustering version. 2. The ultimate prediction model accuracy > 0.95. 3. The average cell per cluster ≥ 30, which controls the cluster size to reach the minimum coverage required for further epigenome analysis such as DMR calls. All three criteria prevented the over-splitting of the clusters; thus, we selected the maximum resolution parameter under meeting the criteria using a grid search.

Three-level of iterative clustering analysis. We used an iterative approach to cluster the data into three levels of categories with the consensus clustering procedure described above. In the first level termed CellClass, clustering analysis is done on all cells. The resulting clusters are then manually merged into three canonical classes, glutamatergic neurons, GABAergic neurons, and non-neurons, based on marker genes. The same clustering procedure was then conducted within each CellClass to get clusters as the MajorType level. Within each MajorType, we got the final clusters as the SubTypes in the same way.

Integrating cell clusters identified from snmC-seq2 and from Cv3. We identified gene markers based on gene body mCH hypo-methylation for each level of clustering of snmC-seq2 data using our in-house analysis utilities (https://github.com/lhqing/cemba_data), and identified gene markers for cell class from Cv3 analysis using scanpy [71]. We then used Scanorama [76] to integrate the two modalities.

595 Calling CG differentially methylated regions (DMRs). We identified CG DMRs using methylpy
596 (https://github.com/yupenghe/methylpy) as previously described [77]. Briefly, we first called CG
597 differentially methylated sites and then merged them into blocks if they both showed similar sample-
598 specific methylation patterns and were within 250bp. Normalized relative lengths of DMRs (Figure 4d)
599 were calculated by summation of lengths of DMRs and 250bp around divided by numbers of cytosine
600 covered in sequencing.
601
602 TFBS motif enrichment analysis. For each cell subclass (cluster), we performed TFBS motif enrichment
603 analysis for its hypo-methylated DMRs against the hypo-methylated DMRs from other cell subclasses
604 (clusters) using software AME [78]. DMRs and 250bp regions around were used in the analysis.
605
606 ***SNARE-Seq2: Sample preparation***
607 Human and marmoset primary motor cortex nuclei were isolated for SNARE-seq2 according to the
608 following protocol: https://www.protocols.io/view/nuclei-isolation-for-snare-seq2-8tvhwn6 [7,79].
609 Fluorescence-activated nuclei sorting (FANS) was then performed on a FACSAria Fusion (BD
610 Biosciences, Franklin Lakes, NJ) gating out debris from FSC and SSC plots and selecting $DAPI^+$
611 singlets (Extended Data Fig. 5a). Samples were kept on ice until sorting was complete and were used
612 immediately for SNARE-seq2.
613
614 ***SNARE-Seq2: Library preparation and sequencing***
615 A detailed step-by-step protocol for SNARE-Seq2 has been outlined in a companion paper [38]. The
616 resulting AC libraries were sequenced on MiSeq (Illumina) (R1: 75 cycles for the 1st end of AC DNA
617 read, R2: 94 cycles for cell barcodes and UMI read, R3: 8 cycles for i5 read, R4: 75 cycles for the 2nd
618 end of AC DNA read) for library validation, then on NovaSeq6000 (Illumina) using 300 cycles reagent
619 kit for data generation. RNA libraries were combined at equimolar ratio and sequenced on MiSeq
620 (Illumina) (Read 1: 70 cycles for the cDNA read, Index 1: 6 cycles for i7 read, Read 2: 94 cycles for cell

621 barcodes and UMI read) for library validation, then on NovaSeq6000 (Illumina) using 200 cycles
622 reagent kit for data generation.
623
624 ***SNARE-Seq2: Data processing***
625 A detailed step-by-step SNARE-seq2 data processing pipeline has been provided in a companion
626 paper [38]. For RNA data, this has involved the use of dropEst to extract cell barcodes and STAR
627 (v2.5.2b) to align tagged reads to the genome (GRCh38 version 3.0.0 for human; GCF 000004665.1
628 Callithrix jacchus-3.2, marmoset). For AC data, this involved snaptools for alignment to the genome
629 (cellranger-atac-GRCh38-1.1.0 for human, GCF 000004665.1 Callithrix jacchus-3.2, marmoset) and to
630 generate snap objects for processing using the R package snapATAC.
631
632 ***SNARE-Seq2: Data analysis***
633 RNA quality filtering. For SNARE-Seq2 data, quality filtering of cell barcodes and clustering analysis
634 were first performed on transcriptomic (RNA) counts and used to inform on subsequent accessible
635 chromatin quality filtering and analysis. Each cell barcode was tagged by an associated library batch ID
636 (for example MOP1, MOP2… etc.), RNA read counts associated with dT and n6 adaptor primers were
637 merged, libraries were combined for each sample within each experiment and empty barcodes
638 removed using the emptyDrops() function of DropletUtils [80], mitochondrial transcripts were removed,
639 doublets were identified using the DoubletDetection software [81] and removed. All samples were
640 combined across experiments within species and cell barcodes having greater than 200 and less than
641 7500 genes detected were kept for downstream analyses. To further remove low quality datasets, a
642 gene UMI ratio filter (gene.vs.molecule.cell.filter) was applied using Pagoda2 (https://github.com/hms-
643 dbmi/pagoda2).
644
645 RNA data clustering. For human SNARE-seq2 RNA data, clustering analysis was first performed using
646 Pagoda2 where counts were normalized to the total number per nucleus and batch variations were

647 corrected by scaling expression of each gene to the dataset-wide average. After variance
648 normalization, the top 6000 over-dispersed genes were used for principal component analysis.
649 Clustering was performed using an approximate k-nearest neighbor graph (k values between 50 – 500)
650 based on the top 75 principal components and cluster identities were determined using the infomap
651 community detection algorithm. Major cell types were identified using a common set of broad cell type
652 marker genes: *GAD1/GAD2* (GABAergic neurons), *SLC17A7/SATB2* (glutamatergic neurons),
653 *PDGFRA* (oligodendrocyte progenitor cells), *AQP4* (astrocytes), *PLP1/MOBP* (oligodendrocytes),
654 *MRC1* (perivascular macrophages), *PTPRC* (T cells), *PDGFRB* (vascular smooth muscle cells), *FLT1*
655 (vascular endothelial cells), *DCN* (vascular fibroblasts), *APBB1IP* (microglia) (Extended Data Fig. 5c).
656 Low quality clusters that showed very low gene/UMI detection rates, low marker gene detection and/or
657 mixed cell type marker profiles were removed. Oligodendrocytes were over-represented (54,080 total),
658 possibly reflecting a deeper subcortical sampling then intended, therefore, to ensure a more balanced
659 distribution of cell types, we capped the number of oligodendrocytes at 5000 total and repeated the
660 PAGODA2 clustering as above. To achieve optimal clustering of the different cell types, different k
661 values were used to identify cluster subpopulations for different cell types (L2/3 glutamatergic neurons,
662 k = 500; all other glutamatergic neurons, astrocytes, oligodendrocytes, OPCs, k = 100; GABAergic
663 neurons, vascular cells, microglia/perivascular macrophages, k = 50). To assess the appropriateness of
664 the chosen k values, clusters were compared against SMARTer clustering of data generated on human
665 M1 through correlation of cluster-averaged scaled gene expression values using the corrplot package
666 (https://github.com/taiyun/corrplot) (Extended Data Fig. 5d). For cluster visualization, uniform manifold
667 approximation and projection (UMAP) dimensional reduction was performed in Seurat (version 3.1.0)
668 using the top 75 principal components identified using Pagoda2. For marmoset, clustering was initially
669 performed using Seurat, where the top 2000 variable features were selected from the mean variance
670 plot using the 'vst' method and used for principal component analysis. UMAP embeddings were
671 generated using the top 75 principal components. To harmonize cellular populations across platforms
672 and modalities, snRNA-seq within-species cluster identities were then predicted from both human and

673 marmoset data. We used an iterative nearest centroid classifier algorithm (Methods, 'Mapping of
674 samples to reference taxonomies') to generate probability scores for each SNARE-seq2 nuclei mapping
675 to their respective species' snRNA-seq reference cluster (Cv3 for marmoset and SMART-Seqv4 for
676 human). Comparing the predicted RNA cluster assignment of each nuclei with Pagoda2-identified
677 clusters showed highly consistent cluster membership using Jaccard similarity index (Extended Data
678 Fig. 5e), confirming the robustness of these cell identities discovered using different analysis platforms.
679
680 AC quality filtering and peak calling. Initial analysis of corresponding SNARE-Seq2 chromatin
681 accessibility data was performed using SnapATAC software (version 2)
682 (https://github.com/r3fang/SnapATAC) (https://doi.org/10.1101/615179). Snap objects were generated
683 by combining individual snap files across libraries within each species. Cell barcodes were included for
684 downstream analyses only if cell barcodes passed RNA quality filtering (above) and showed greater
685 than 1000 read fragments and 500 UMI. Read fragments were then binned to 5000 bp windows of the
686 genome and only cell barcodes showing the fraction of binned reads within promoters greater than 10%
687 (15% for marmoset) and less than 80% were kept for downstream analysis. Peak regions were called
688 independently for RNA cluster, subclass and class groupings using MACS2 software
689 (https://github.com/taoliu/MACS) using the following options "--nomodel --shift 100 --ext 200 --qval 5e-2
690 -B --SPMR". Peak regions were combined across peak callings and used to generate a single peak
691 count matrix (cell barcodes by chromosomal peak locations) using the "createPmat" function of
692 SnapATAC.
693
694 AC data clustering. The peak count matrices were filtered to keep only locations from chromosomes 1-
695 22, x or y, and processed using Seurat (version 3.1.0) and Signac (version 0.1.4) software [24]
696 (https://satijalab.org). All peaks having at least 100 counts (20 for marmoset) across cells were used for
697 dimensionality reduction using latent semantic indexing ("RunLSI" function) and visualized by UMAP
698 using the first 50 dimensions (40 for marmoset).

699

700 Calculating gene activity scores. For a gene activity matrix from accessibility data, cis-co-accessible
701 sites and gene activity scores were calculated using Cicero software (v1.2.0) [39] (https://cole-trapnell-
702 lab.github.io/cicero-release/). The binary peak matrix was used as input with expression family variable
703 set to "binomialff" to make the aggregated input Cicero CDS object using the AC peak-derived UMAP
704 coordinates and setting 50 cells to aggregate per bin. Co-accessible sites were then identified using the
705 "run_cicero" function using default settings and modules of cis-co-accessible sites identified using the
706 "generate_ccans" function. Co-accessible sites were annotated to a gene if they fell within a region
707 spanning 10,000 bp upstream and downstream of the gene's transcription start site (TSS). The Cicero
708 gene activity matrix was then calculated using the "build_gene_activity_matrix" function using a co-
709 accessibility cutoff of 0.25 and added to a separate assay of the Seurat object.

710

711 Integrating RNA/AC data modalities. For reconciliation of differing resolutions achievable from RNA and
712 accessible chromatin (Extended Data Fig. 5f-k), integrative analysis was performed using Seurat.
713 Transfer anchors were identified between the activity and RNA matrices using the
714 "FindTransferAnchors" function. For human, transfer anchors were generated using an intersected list
715 of variable genes identified from Pagoda2 analysis of RNA clusters (top 2000 genes) and marker genes
716 for clusters identified from SSv4 data (2492 genes having β-scores > 0.4), and canonical correlation
717 analysis (CCA) for dimension reduction. For marmoset, transfer anchors were generated using an
718 intersected list of variable genes identified using Seurat (top 2000 genes) and DEGs identified between
719 marmoset consensus clusters (Cv3 snRNA-seq data, $P < 0.05$, top 100 markers per cluster). Imputed
720 RNA expression values were then calculated using the "TransferData" function from the Cicero gene
721 activity matrix using normalized RNA expression values for reference and LSI for dimension reduction.
722 RNA and imputed expression data were merged, a UMAP co-embedding and shared nearest neighbor
723 (SNN) graph generated using the top 50 principal components (40 for marmoset) and clusters identified
724 ("FindClusters") using a resolution of 4. Resulting integrated clusters were compared against

725 consensus RNA clusters by calculating jaccard similarity scores using scratch.hicat software. Cell
726 populations identified as T-cells from Pagoda2 analysis (human only) and those representing low
727 quality integrated clusters, showing a mixture of disparate cell types, were removed from these
728 analyses. RNA clusters were assigned to co-embedded clusters based on the highest jaccard similarity
729 score and frequency and then merged to generate the best matched co-embedded clusters, taking in
730 account cell type and subclass to ensure more accurate merging of ambiguous populations. This
731 enabled AC-level clusters that directly matched the RNA-defined populations (Extended Data Fig. 5k).
732 For consensus cluster and subclass level predictions (Extended Data Fig. 5g) the Seurat
733 "TransferData" function was used to transfer RNA consensus cluster or subclass labels to AC data
734 using the pre-computed transfer anchors and LSI dimensionality reduction.
735
736 Final AC peak and gene activity matrices. A final combined list of peak regions was then generated
737 using MACS2 as detailed above for all cell populations corresponding to RNA consensus (> 100
738 nuclei), accessibility-level, subclass (> 50 nuclei) and class level barcode groupings. The corresponding
739 peak by cell barcode matrix generated by SnapATAC was used to establish a Seurat object as outlined
740 above, with peak counts, Cicero gene activity scores and RNA expression values for matched cell
741 barcodes contained within different assay slots.
742
743 Transcription factor motif analyses. Jaspar motifs (JASPAR2020, all vertebrate) were used to generate
744 a motif matrix and motif object that was added to the Seurat object using Signac ("CreateMotifMatrix",
745 "CreateMotifObject", "AddMotifObject") and GC content, region lengths and dinucleotide base
746 frequencies calculated using the "RegionStats" function. Motif enrichments within specific chromosomal
747 sites were calculated using the FindMotifs function. For motif activity scores, chromVAR
748 (https://greenleaflab.github.io/chromVAR) was performed according to default parameters (marmoset)
749 or using Signac "RunChromVAR" function on the peak count matrix (human). The chromVAR deviation
750 score matrix was then added to a separate assay slot of the Seurat object and differential activity of

751 TFBS between different populations were assessed using the “Find[All]Markers” function through
752 logistic regression and using the number of peak counts as a latent variable.
753
754 Differentially accessible regions (DARs) between cell populations (Fig. 4b) were identified using the
755 “find_all_diff” function (https://github.com/yanwu2014/chromfunks) and p-values calculated using a
756 hypergeometric test. For visualization, the top DARs (q value < 0.001 and log-fold change > 1) were
757 selected and the top distinct sites visualized by dot plot in Seurat. For motif enrichment analyses, peak
758 counts associated with the clusters selected for comparison (all subclasses, all AC-level clusters,
759 *PVALB*-positive for ChC analyses) were used to identify cis-co-accessible site networks or CCANs
760 using cicero as indicated above. Peak locations were annotated to the nearest gene (10,000 bases
761 upstream and downstream of the TSS) and only genes identified from SNARE-seq2 RNA data as being
762 differentially expressed (Seurat, Wilcoxon Rank Sum test) within the clusters of interest (adjusted P <
763 0.05, average log-fold change > 0.5) were used. Genes having more than one co-accessible site were
764 assessed for motif enrichments within all overlapping sites using the “FindMotifs” function in Signac
765 (using peaks for all cell barcodes for subclass and AC-level, or only peaks for ChC or L5 ET cells).
766 Motifs were then trimmed to only those showing significant differential activity (chromVAR) between the
767 clusters of interest (P < 0.05) as assessed using the “FindMarkers” function on the chromVAR assay
768 slot using Seurat and using the number of total peaks as a latent variable. The top distinct genes
769 (subclass, AC-level) or all genes (ChC, Betz) used for motif enrichment analysis were visualized for
770 scaled average RNA expression levels and scaled average cicero gene activities using the ggHeat
771 plotting function (SWNE package, https://github.com/yanwu2014/swne). Top chromVAR TFBS activities
772 were also visualized using ggHeat.
773
774 Correlation plots. For correlation of RNA expression and associated AC activities for consensus and
775 AC-level clusters (Extended Data Fig. 6a-b), average scaled expression values were generated and
776 pairwise correlations performed for marker genes identified from an intersected list of variable genes

777 identified from Pagoda2 analysis of RNA clusters (top 2000 genes) and marker genes for clusters
778 identified from SSv4 data (2492 genes having β-scores > 0.4). For correlation across species,
779 expression values for genes used to integrate human and marmoset GABAergic and glutamatergic
780 clusters (Cv3 scRNA-seq data), or chromVAR TFBS activity scores for all Jaspar motifs were averaged
781 by subclass, scaled (trimming values to a minimum of 0 and a maximum of 4) for each species
782 separately, then correlated and visualized using corrplot.
783
784 Plots and figures. All UMAP, feature, dot, and violin plots were generated using Seurat. Connection
785 plots were generated using cicero and peak track gradient heatmaps were generated using Gviz [82] from
786 bedGraph files generated during peak calling using SnapATAC. Correlation plots were generated using
787 the corrplot package.
788
789 ***Mouse chandelier cell ATAC-Seq: Data acquisition and analysis***
790 Chandelier cells are rare in mouse cortex and were enriched by isolating individual neurons from
791 transgenically-labelled mouse primary visual cortex (VISp). Many of the transgenic mouse lines have
792 previously been characterized by single-cell RNA-seq [1]. Single-cell suspensions of cortical neurons
793 were generated as described previously [1] and subjected to tagmentation (ATAC-seq) [83,84]. Mixed
794 libraries, containing 60 to 96 samples were sequenced on an Illumina MiSeq. In total, 4,275 single-cells
795 were collected from 36 driver-reporter combinations in 67 mice. After sequencing, raw FASTQ files
796 were aligned to the GRCm38 (mm10) mouse genome using Bowtie v1.1.0 as previously described [9].
797 Following alignment, duplicate reads were removed using samtools rmdup, which yielded only single
798 copies of uniquely mapped paired reads in BAM format. Quality control filtering was applied to select
799 samples with >10,000 uniquely mapped paired-end fragments, >10% of which were longer than 250
800 base pairs and with >25% of their fragments overlapping high-depth cortical DNase-seq peaks from
801 ENCODE [85]. The resulting dataset contained a total of 2,799 samples.
802

803 To increase the cell-type resolution of chromatin accessibility profiles beyond that provided by driver
804 lines, a feature-free method for computation of pairwise distances (Jaccard) was used. Using Jaccard
805 distances, principal component analysis (PCA) and t-distributed stochastic neighbor embedding (t-SNE)
806 were performed, followed by Phenograph clustering [86]. This clustering method grouped cells from
807 class-specific driver lines together, but also segregated them into multiple clusters. Phenograph-defined
808 neighborhoods were assigned to cell subclasses and clusters by comparison of accessibility near
809 transcription start site (TSS ± 20 kb) to median expression values of scRNA-seq clusters at the cell type
810 and at the subclass level from mouse primary visual cortex [87]. From this analysis, a total of 226
811 samples were assigned to *Pvalb* and 124 samples to *Pvalb Vipr2* (ChC) clusters. The sequence data
812 for these samples were grouped together and further processed through the Snap-ATAC pipeline.
813
814 Mouse scATAC-seq peak counts for *Pvalb* and ChC were used to generate a Seurat object as outlined
815 for human and marmoset SNARE-Seq2 AC data. Cicero cis-co-accessible sites were identified, gene
816 activity scores calculated, and motif enrichment analyses performed as outlined above. Genes used for
817 motif enrichment were ChC markers identified from differential expression analysis between *PVALB-*
818 *positive* clusters in mouse Cv3 scRNA-seq data (adjusted $P < 0.05$).
819
820 ***Patch-seq neuronal physiology, morphology, and transcriptomics***
821 Subjects. The human neurosurgical specimen was obtained from a 61-year old female patient that
822 underwent deep tumor resection (glioblastoma) from the frontal lobe at a local hospital (Harborview
823 Medical Center). The patient provided informed consent and experimental procedures were approved
824 by the hospital institute review board before commencing the study. Post-hoc analysis revealed that the
825 neocortical tissue obtained from this patient was from a premotor region near the confluence of the
826 superior frontal gyrus and the precentral gyrus (Fig. 7g). All procedures involving macaques and mice
827 were approved by the Institutional Animal Care and Use Committee at either the University of
828 Washington or the Allen Institute for Brain Science. Macaque M1 tissue was obtained from male (n=4)

829 and female (n=5) animals (mean age= 10 ± 2.21 years) designated for euthanasia via the Washington
830 National Primate Research Center's Tissue Distribution Program. Mouse M1 tissue was obtained from
831 4-12 week old male and female mice from the following transgenic lines: *Thy1h*-eyfp (B6.Cg-Tg(*Thy1*-
832 YFP)-HJrs/J: JAX Stock No. 003782), *Etv1*-egfp Tg(*Etv1*-EGFP)BZ192Gsat/Mmucd (etv1) mice
833 maintained with the outbred Charles River Swiss Webster background (Crl:CFW(SW) CR Stock No.
834 024), and C57BL/6-Tg(*Pvalb*-tdTomato)15Gfng/J: JAX stock No. 027395.
835
836 Brain slice preparation. Brain slice preparation was similar for *Pvalb*-TdTomato mice, macaque and
837 human samples. Upon resection, human neurosurgical tissue was immediately placed in a chilled and
838 oxygenated solution formulated to prevent excitotoxicity and preserve neural function [88]. This artificial
839 cerebral spinal fluid (NMDG aCSF) consisted of (in mM): 92 with N-methyl-D-glucamine (NMDG), 2.5
840 KCl, 1.25 NaH_2PO_4, 30 $NaHCO_3$, 20 4-(2-hydroxyethyl)-1-piperazineethanesulfonic acid (HEPES), 25
841 glucose, 2 thiourea, 5 Na-ascorbate, 3 Na-pyruvate, 0.5 $CaCl_2 \cdot 4H_2O$ and 10 $MgSO_4 \cdot 7H_2O$. The pH of
842 the NMDG aCSF was titrated to pH 7.3–7.4 with concentrated hydrochloric acid and the osmolality was
843 300-305 mOsmoles/Kg. The solution was pre-chilled to 2-4°C and thoroughly bubbled with carbogen
844 (95% O_2/5% CO_2) prior to collection. Macaques were anesthetized with sevoflurane gas during which
845 the entire cerebrum was extracted and placed in the same protective solution described above. After
846 extraction, macaques were euthanized with sodium-pentobarbital. We dissected the trunk/limb area of
847 the primary motor cortex for brain slice preparation. *Pvalb*-TdTomato mice were deeply anesthetized by
848 intraperitoneal administration of Advertin (20mg/kg IP) and were perfused through the heart with NMDG
849 aCSF (bubbled with carbogen).
850
851 Brains were sliced at 300-micron thickness on a vibratome using the NMDG protective recovery
852 method and a zirconium ceramic blade [61,88]. Mouse brains were sectioned coronally, and human and
853 macaque brains were sectioned such that the angle of slicing was perpendicular to the pial surface.
854 After sections were obtained, slices were transferred to a warmed (32-34° C) initial recovery chamber

filled with NMDG aCSF under constant carbogenation. After 12 minutes, slices were transferred to a chamber containing an aCSF solution consisting of (in mM): 92 NaCl, 2.5 KCl, 1.25 NaH_2PO_4, 30 $NaHCO_3$, 20 HEPES, 25 glucose, 2 thiourea, 5 Na-ascorbate, 3 Na-pyruvate, 2 $CaCl_2 \cdot 4H_2O$ and 2 $MgSO_4 \cdot 7H_2O$ continuously bubbled with 95% O_2/5% CO_2. Slices were held in this chamber for use in acute recordings or transferred to a 6-well plate for long-term culture and viral transduction. Cultured slices were placed on membrane inserts and wells were filled with culture medium consisting of 8.4 g/L MEM Eagle medium, 20% heat-inactivated horse serum, 30 mM HEPES, 13 mM D-glucose, 15 mM $NaHCO_3$, 1 mM ascorbic acid, 2 mM $MgSO_4 \cdot 7H_2O$, 1 mM $CaCl_2.4H_2O$, 0.5 mM GlutaMAX-I, and 1 mg/L insulin (Ting et al 2018). The slice culture medium was carefully adjusted to pH 7.2-7.3, osmolality of 300-310 mOsmoles/Kg by addition of pure H_2O, sterile-filtered and stored at 4°C for up to two weeks. Culture plates were placed in a humidified 5% CO_2 incubator at 35°C and the slice culture medium was replaced every 2-3 days until end point analysis. 1-3 hours after brain slices were plated on cell culture inserts, brain slices were infected by direct application of concentrated AAV viral particles over the slice surface (Ting et al 2018).

Thy1 and Etv1 mice were deeply anesthetized by IP administration of ketamine (130 mg/kg) and xylazine (8.8 mg/kg) mix and were perfused through the heart with chilled (2-4°C) sodium-free aCSF consisting of (in mM): 210 Sucrose, 7 D-glucose, 25 $NaHCO_3$, 2.5 KCl, 1.25 NaH_2PO_4, 7 $MgCl_2$, 0.5 $CaCl_2$, 1.3 Na-ascorbate, 3 Na-pyruvate bubbled with carbogen (95% O_2/5% CO_2). Near coronal slices 300 microns thick were generated using a Leica vibratome (VT1200) in the same sodium-free aCSF and were transferred to warmed (35°C) holding solution (in mM): 125 NaCl, 2.5 KCl, 1.25 NaH_2PO_4, 26 $NaHCO_3$, 2 $CaCl_2$, 2 $MgCl_2$, 17 dextrose, and 1.3 sodium pyruvate bubbled with carbogen (95% O_2/5% CO_2). After 30 minutes of recovery, the chamber holding slices was allowed to cool to room temperature.

880 Patch clamp electrophysiology. Macaque, human and *Pvalb*-TdTomato mouse brain slices were placed
881 in a submerged, heated (32-34°C) recording chamber that was continually perfused (3-4 mL/min) with
882 aCSF under constant carbogenation and containing (in mM) 1): 119 NaCl, 2.5 KCl, 1.25 NaH_2PO_4, 24
883 $NaHCO_3$, 12.5 glucose, 2 $CaCl_2 \cdot 4H_2O$ and 2 $MgSO_4 \cdot 7H_2O$ (pH 7.3-7.4). Slices were viewed with an
884 Olympus BX51WI microscope and infrared differential interference contrast (IR-DIC) optics and a 40x
885 water immersion objective. The infragranular layers of macaque primary motor cortex and human
886 premotor cortex are heavily myelinated, which makes visualization of neurons under IR-DIC virtually
887 impossible. To overcome this challenge, we labeled neurons using various viral constructs in
888 organotypic slice cultures (Extended Data Fig. 10g).
889 Patch pipettes (2-6 MΩ) were filled with an internal solution containing (in mM): 110.0 K-gluconate,
890 10.0 HEPES, 0.2 EGTA, 4 KCl, 0.3 Na2-GTP, 10 phosphocreatine disodium salt hydrate, 1 Mg-ATP, 20
891 µg/ml glycogen, 0.5U/µL RNAse inhibitor (Takara, 2313A) and 0.5% biocytin (Sigma B4261), pH 7.3.
892 Fluorescently labeled neurons from *Thy1* or *Etv1* mice were visualized through a 40x objective using
893 either Dodt contrast with a CCD camera (Hamamatsu) and/or a 2-photon imaging/ uncaging system
894 from Prairie (Bruker) Technologies. Recordings were made in aCSF: (in mM): 125 NaCl, 3.0 KCl, 1.25
895 NaH_2PO_4, 26 $NaHCO_3$, 2 $CaCl_2$, 1 MgCl2, 17 dextrose, and 1.3 sodium pyruvate bubbled with
896 carbogen (95% O_2/5% CO_2) at 32-35°, with synaptic inhibition blocked using 100 µM picrotoxin.
897 Sylgard-coated patch pipettes (3-6 MΩ) were filled with an internal solution containing (in mM): 135 K-
898 gluconate, 12 KCl, 11 HEPES, 4 MgATP, 0.3 NaGTP, 7 K_2-phosphocreatine, 4 Na_2-phophocreatine (pH
899 7.42 with KOH) with neurobiotin (0.1-0.2%), Alexa 594 (40 µM) and Oregon Green BAPTA 6F (100
900 µM).
901
902 Whole cell somatic recordings were acquired using either a Multiclamp 700B amplifier, or an AxoClamp
903 2B amplifier (Molecular Devices) and were digitized using an ITC-18 (HEKA). Data acquisition software
904 was either MIES (https://github.com/AllenInstitute/MIES/) or custom software written in Igor Pro.
905 Electrical signals were digitized at 20-50 kHz and filtered at 2-10 kHz. Upon attaining whole-cell current

906 clamp mode, the pipette capacitance was compensated and the bridge was balanced. Access
907 resistance was monitored throughout the recording and was 8-25 MΩ.
908
909 Data analysis. Data were analyzed using custom analysis software written in Igor Pro. All
910 measurements were made at resting membrane potential. Input resistance (R_N) was measured from a
911 series of 1 s hyperpolarizing steps from -150 pA to +50 pA in +20 pA increments. For neurons with low
912 input resistance (e.g. the Betz cells) this current injection series was scaled by upwards of 4x. Input
913 resistance (R_N) was calculated from the linear portion of the current−steady state voltage relationship
914 generated in response to these current injections. Resonance (f_R) was determined from the voltage
915 response to a constant amplitude sinusoidal current injection (Chirp stimulus). The chirp stimulus
916 increased in frequency either linearly from 1-20 Hz over 20 s or logarithmically from 0.2-40 Hz over 20s.
917 The amplitude of the Chirp was adjusted in each cell to produce a peak-to-peak voltage deflection of
918 ~10 mV. The impedance amplitude profile (ZAP) was constructed from the ratio of the fast Fourier
919 transform of the voltage response to the fast Fourier transform of the current injection. ZAPs were
920 produced by averaging at least three presentations of the Chirp and were smoothed using a running
921 median smoothing function. The frequency corresponding to the peak impedance (Z_{max}) was defined as
922 the resonant frequency. Spike input/output curves were constructed in response to 1 s step current
923 injections (50 pA-500 pA in 50 pA steps). For a subset of experiments, this current injection series was
924 extended to 3A in 600 pA steps to probe the full dynamic range of low R_N neurons. Spike frequency
925 acceleration analysis was performed for current injections producing ~10 spikes during the 1 s step.
926 Acceleration ratio was defined as the ratio of the second to the last interspike interval. To examine the
927 dynamics of spike timing over longer periods, we also measured spiking in response to 10 s step
928 current injections in which the amplitude of the current was adjusted to produce ~5 spikes in the first
929 second. Action potential properties were measured for currents near rheobase. Action potential
930 threshold was defined as the voltage at which the first derivative of the voltage response exceeded 20

931 V/s. AP width was measured at half the amplitude between threshold and the peak voltage. Fast AHP
932 was defined relative to threshold. We clustered mouse, macaque and human pyramidal neurons into
933 two broad groups based on their R_N and f_R using Ward's algorithm.
934
935 Biocytin histology. A horseradish peroxidase (HRP) enzyme reaction using diaminobenzidine (DAB) as
936 the chromogen was used to visualize the filled cells after electrophysiological recording, and 4,6-
937 diamidino-2-phenylindole (DAPI) stain was used identify cortical layers as described previously [89].
938
939 Microscopy. Mounted sections were imaged as described previously [89]. Briefly, operators captured
940 images on an upright AxioImager Z2 microscope (Zeiss, Germany) equipped with an Axiocam 506
941 monochrome camera and 0.63x optivar. Two-dimensional tiled overview images were captured with a
942 20X objective lens (Zeiss Plan-NEOFLUAR 20X/0.5) in brightfield transmission and fluorescence
943 channels. Tiled image stacks of individual cells were acquired at higher resolution in the transmission
944 channel only for the purpose of automated and manual reconstruction. Light was transmitted using an
945 oil-immersion condenser (1.4 NA). High-resolution stacks were captured with a 63X objective lens
946 (Zeiss Plan-Apochromat 63x/1.4 Oil or Zeiss LD LCI Plan-Apochromat 63x/1.2 Imm Corr) at an interval
947 of 0.28 µm (1.4 NA objective; mouse specimens) or 0.44 µm (1.2 NA objective; human and non-human
948 primate specimens) along the Z axis. Tiled images were stitched in ZEN software and exported as
949 single-plane TIFF files.
950
951 Morphological reconstruction. Reconstructions of the dendrites and the full axon were generated based
952 on a 3D image stack that was run through a Vaa3D-based image processing and reconstruction
953 pipeline as described previously [89].
954
955 Viral vector production and transduction. Recombinant AAV vectors were produced by triple-
956 transfection of ITR-containing enhancer plasmids along with AAV helper and rep/cap plasmids using

957 the AAV293 cell line, followed by harvest, purification and concentration of the viral particles. The
958 AAV293 packaging cell line and plasmid supplying the helper function are available from a commercial
959 source (Cell Biolabs). The PHP.eB capsid variant was generated by Dr. Viviana Gradinaru at the
960 California Institute of Technology [90] and the DNA plasmid for AAV packaging is available from Addgene
961 (plasmid#103005). Quality control of the packaged AAV was determined by viral titering to determine
962 an adequate concentration was achieved (>$5E^{12}$ viral genomes per mL), and by sequencing the AAV
963 genome to confirm the identity of the viral vector that was packaged. Human and NHP L5 ET neurons
964 including Betz cells were targeted in cultured slices by transducing the slices with viral vectors that
965 either generically label neurons (AAV-hSyn1-tdTomato), or that enrich for L5 ET neurons by expressing
966 reporter transgene under the control of the msCRE4 enhancer [87].
967
968 Processing of Patch-seq samples. For a subset of experiments, the nucleus was extracted at the end of
969 the recording and processed for RNA-sequencing. Prior to data collection for these experiments, all
970 surfaces were thoroughly cleaned with RNAse Zap. The contents of the pipette were expelled into a
971 PCR tube containing lysis buffer (Takara, 634894). cDNA libraries were produced using the SMART-
972 Seq v4 Ultra Low Input RNA Kit for Sequencing according to the manufacturer's instructions. We
973 performed reverse transcription and cDNA amplification for X PCR cycles. Sample proceeded through
974 Nextera NT DNA Library Preparation using Nextera XT Index Kit V2 Set A(FC-131-2001).
975
976 Mapping of samples to reference taxonomies. To identify which cell type a given patch-seq nuclei
977 mapped to, we used our previously described nearest centroid classifier [1]. Briefly, a centroid classifier
978 was constructed for Glutamatergic reference data (human SSv4 or macaque Cv3) using marker genes
979 for each cluster. Patch-seq nuclei were then mapped to the appropriate species reference 100 times,
980 using 80% of randomly sampled marker genes during each iteration. Probabilities for each nuclei
981 mapping to each cluster were computed over the 100 iterations, resulting in a confidence score ranging

982 from 0 to 100. We identified four human patch-seq nuclei that mapped with > 85% confidence and four
983 macaque nuclei that mapped with > 93% confidence to a cluster in the L5 ET subclass.
984

985 Data availability

986 Raw sequence data are available for download from the Neuroscience Multi-omics Archive
987 (https://nemoarchive.org/) and the Brain Cell Data Center (https://biccn.org/data). Visualization and
988 analysis tools are available at NeMO Analytics (Individual species:
989 https://nemoanalytics.org//index.html?layout_id=ac9863bf; Integrated species:
990 https://nemoanalytics.org//index.html?layout_id=34603c2b) and Cytosplore Viewer
991 (https://viewer.cytosplore.org/). These tools allow users to compare cross-species datasets and
992 consensus clusters via genome and cell browsers and calculate differential expression within and
993 among species. A semantic representation of the cell types defined through these studies is available in
994 the provisional Cell Ontology (https://bioportal.bioontology.org/ontologies/PCL; Supplementary Table
995 1).
996

997 Code availability

998 Code to reproduce figures will be available for download from
999 https://github.com/AllenInstitute/BICCN_M1_Evo.
000

001 Acknowledgements

002 We thank the Tissue Procurement, Tissue Processing and Facilities teams at the Allen Institute for
003 Brain Science for assistance with the transport and processing of postmortem and neurosurgical brain
004 specimens; the Technology team at the Allen Institute for assistance with data management; M.
005 Vawter, J. Davis and the San Diego Medical Examiner's Office for assistance with postmortem tissue
006 donations. We thank Ximena Opitz-Araya and Allen Institute for Brain Science Viral Technology team

007 for AAV packaging. We thank Krissy Brouner, Augustin Ruiz, Tom Egdorf, Amanda Gary, Michelle
008 Maxwell, Alice Pom and Jasmine Bomben for biocytin staining. We thank Nadezhda Dotson, Rachel
009 Enstrom, Madie Hupp, Lydia Potekhina, and Shea Ransford for imaging biocytin filled cells. We thank
010 Lindsay Ng, Dijon Hill and Ram Rajanbabu for patching the human and mouse cells in the figure
011 describing chandelier neurons and Sara Kebede, Alice Mukora, Grace Willams for reconstructing them.
012 This work was funded by the Allen Institute for Brain Science and by the U.S. National Institutes of
013 Health grant U01 MH114812-02 to E.S.L. Support for the development of NS-Forest v.2 and the
014 provisional cell ontology was provided by the Chan–Zuckerberg Initiative DAF, an advised fund of the
015 Silicon Valley Community Foundation (2018-182730). G.Q. is supported by NSF CAREER award
016 1846559. This work was partially supported by an NWO Gravitation project: BRAINSCAPES: A
017 Roadmap from Neurogenetics to Neurobiology (NWO: 024.004.012) and NWO TTW project 3DOMICS
018 (NWO: 17126). This project was supported in part by NIH grants P51OD010425 from the Office of
019 Research Infrastructure Programs (ORIP) and UL1TR000423 from the National Center for Advancing
020 Translational Sciences (NCATS). Its contents are solely the responsibility of the authors and do not
021 necessarily represent the official view of NIH, ORIP, NCATS, the Institute of Translational Health
022 Sciences or the University of Washington National Primate Research Center. This work is supported in
023 part by NIH BRAIN Initiative award RF1MH114126 from the National Institute of Mental Health to
024 E.S.L., J.T.T., and B.P.L., NIH BRAIN Initiative award U19MH121282 to J.R.E., the National Institute on
025 Drug Abuse award R01DA036909 to B.T., National Institute of Neurological Disorders and Stroke
026 award R01NS044163 to W.J.S. and the California Institute for Regenerative Medicine (GC1R-06673-
027 B) and the Chan Zuckerberg Initiative DAF, an advised fund of the Silicon Valley Community
028 Foundation (2018–182730) to R.H.S. J.R.E. is an Investigator of the Howard Hughes Medical Institute.
029 The authors thank the Allen Institute founder, Paul G. Allen, for his vision, encouragement and support.
030

Author contributions

RNA data generation: A.M.Y., A.Re., A.T., B.B.L., B.T., C.D.K., C.R., C.R.P., C.S.L., D.B., D.D., D.M., E.S.L., E.Z.M., F.M.K., G.F., H.T., H.Z., J.C., J.Go., J.S., K.C., K.L., K.Si., K.Sm., K.Z., M.G., M.K., M.T., N.Dee, N.M.R., N.P., R.D.H., S.A.M., S.D., S.L., T.C., T.E.B., T.P., W.J.R. mC data generation: A.B., A.I.A., A.Ri., C.L., H.L., J.D.L., J.K.O., J.R.E., J.R.N., M.M.B., R.G.C. ATAC data generation: A.E.S., B.B.L., B.R., B.T., C.R.P., C.S.L., D.D., J.C., J.D.L., J.K.O., K.Z., L.T.G., M.M.B., N.P., S.P., W.J.R., X.H., X.W. Electrophysiology, morphology, and Patch-seq data generation: A.L.K., B.E.K., D.M., E.S.L., G.D.H., J.Go., J.T.T., K.Sm., M.T., N.Dem., P.R.N., R.D., S.A.S., S.O., T.L.D., T.P., W.J.S. Data archive and infrastructure: A.E.S., A.M., B.R.H., H.C.B., J.A.M., J.Go., J.K., J.O., M.M., O.R.W., R.H., S.A.A., S.S., Z.Y. Cytosplore Viewer software: B.P.L., B.V.L., J.E., T.H. Data analysis: A.D., B.B.L., B.D.A., B.E.K., B.P.L., B.V.L., D.D., E.A.M., E.S.L., F.M.K., F.X., H.L., J.E., J.Gi., J.Go., J.R.E., J.T.T., K.Sm., M.C., N.Dem., N.L.J., O.P., P.V.K., Q.H., R.F., R.H.S., R.Z., S.F., S.O., T.E.B., T.H., W.D., W.T., Y.E.L., Z.Y. Data interpretation: A.D., A.Re., B.B.L., B.E.K., B.T., C.K., C.L., E.S.L., F.X., H.L., H.Z., J.Gi., J.Go., J.R.E., J.T.T., M.C., M.H., M.M.B., N.Dem., N.L.J., P.R.H., P.V.K., Q.H., R.D.H., R.H.S., R.Z., S.D., S.O., T.E.B., W.T., Y.E.L., Z.Y. Writing manuscript: A.D., B.B.L., B.E.K., C.K., E.S.L., F.M.K., M.C., N.Dem., N.L.J., P.R.H., Q.H., R.H.S., T.E.B., W.J.S., W.T.

Competing interests

A.R. is an equity holder and founder of Celsius Therapeutics, a founder of Immunitas, and an SAB member in Syros Pharmaceuticals, Neogene Therapeutics, Asimov, and Thermo Fisher Scientific. B.R. is a shareholder of Arima Genomics, Inc. K.Z. is a co-founder, equity holder and serves on the Scientific Advisor Board of Singlera Genomics. P.V.K. serves on the Scientific Advisory Board to Celsius Therapeutics Inc.

Materials & Correspondence

Correspondence and requests for materials should be addressed to E.S.L. and T.E.B.

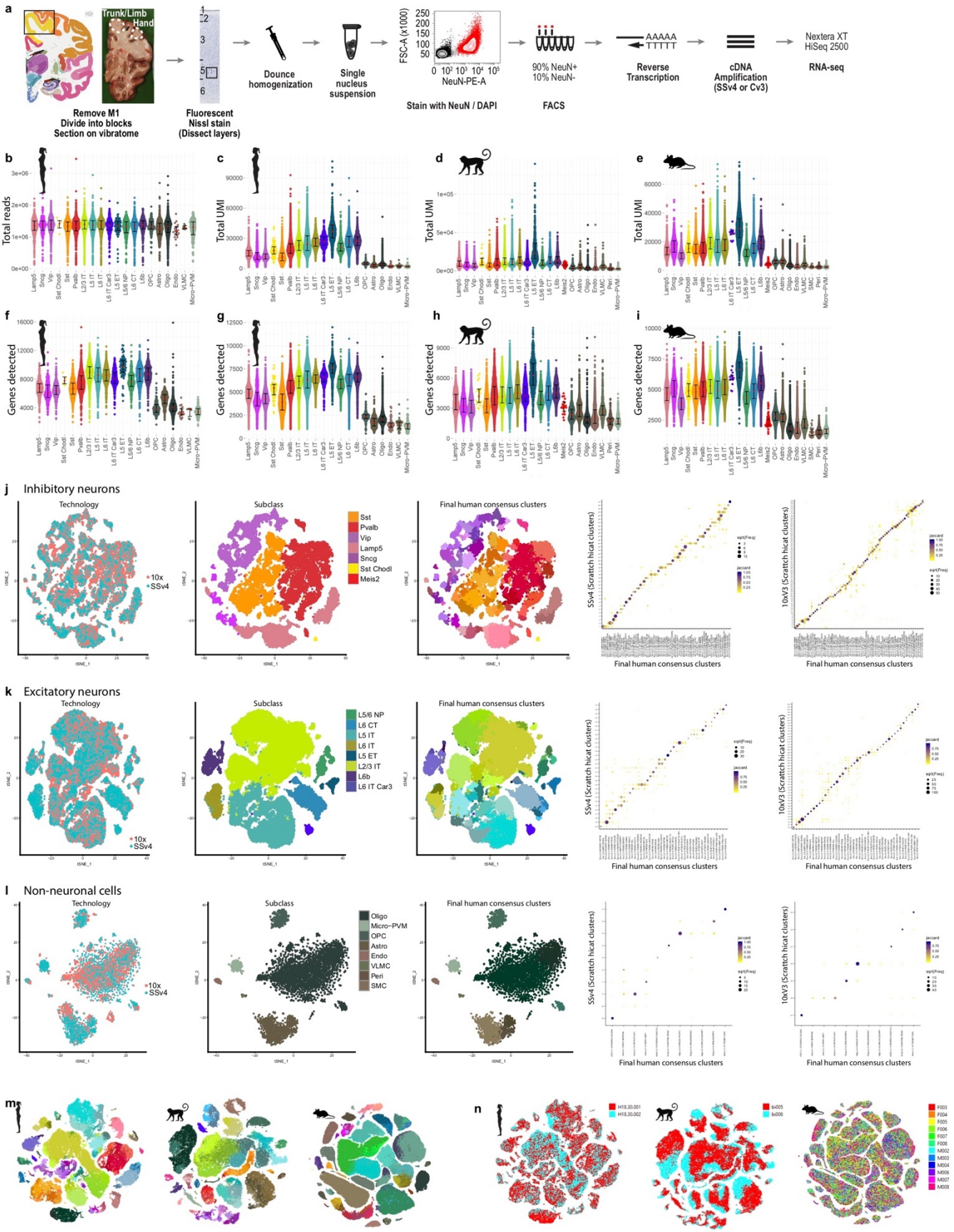
a
Trunk/Limb
Hand
Remove M1
Divide into blocks
Section on vibratome
Fluorescent
Nissl stain
(Dissect layers)
Dounce
homogenization
Single
nucleus
suspension
FSC-A (x1000)
NeuN-PE-A
Stain with NeuN / DAPI
90% NeuN+
10% NeuN-
FACS
AAAAA
TTTTT
Reverse
Transcription
cDNA
Amplification
(SSv4 or Cv3)
Nextera XT
HiSeq 2500
RNA-seq
b
Total reads
c
Total UMI
d
Total UMI
e
Total UMI
f
Genes detected
g
Genes detected
h
Genes detected
i
Genes detected
j Inhibitory neurons
Technology
10x
SSv4
Subclass
Sst
Pvalb
Vip
Lamp5
Sncg
Sst Chodl
Meis2
Final human consensus clusters
SSv4 (Scratch hicat clusters)
10xV3 (Scratch hicat clusters)
k Excitatory neurons
L5/6 NP
L6 CT
L5 IT
L6 IT
L5 ET
L2/3 IT
L6b
L6 IT Car3
l Non-neuronal cells
Oligo
Micro-PVM
OPC
Astro
Endo
VLMC
Peri
SMC
m
n

058

059 **Extended Data Figure 1. RNA-seq quality metrics and integration of human datasets. a**,
060 Schematic of single-nucleus isolation from M1 of post-mortem human brain and profiling with RNA-seq.
061 Box in the Nissl image highlights a cluster of Betz cells in L5. **b**, Using SSv4, > 1 million total reads
062 were sequenced across all subclasses in human. **c-e**, Using Cv3, total unique molecular identifiers
063 (UMI) varies between subclasses, and these differences are shared across species. **f-i**, Gene detection
064 (expression > 0) is highest in human using SSv4 (**e**) and lowest for marmoset using Cv3 (**h**). Note that
065 the average read depth used for SSv4 was approximately 20-fold greater than for Cv3 (target 60,000
066 reads per nucleus). **j-k**, tSNE projections of single nuclei based on expression of several thousand
067 genes with variable gene expression and colored by cluster label (**j**) or donor (**k**). **l-n**, Integration of
068 SSv4 and Cv3 RNA-seq datasets from human single nuclei isolated from GABAergic (**l**) and
069 glutamatergic (**m**) neurons and non-neuronal cells (**n**). Left: UMAP visualizations colored by RNA-seq
070 technology, cell subclass, and unsupervised consensus clusters. Right: Confusion matrices show
071 membership of SSv4 and Cv3 nuclei within integrated consensus clusters.
072

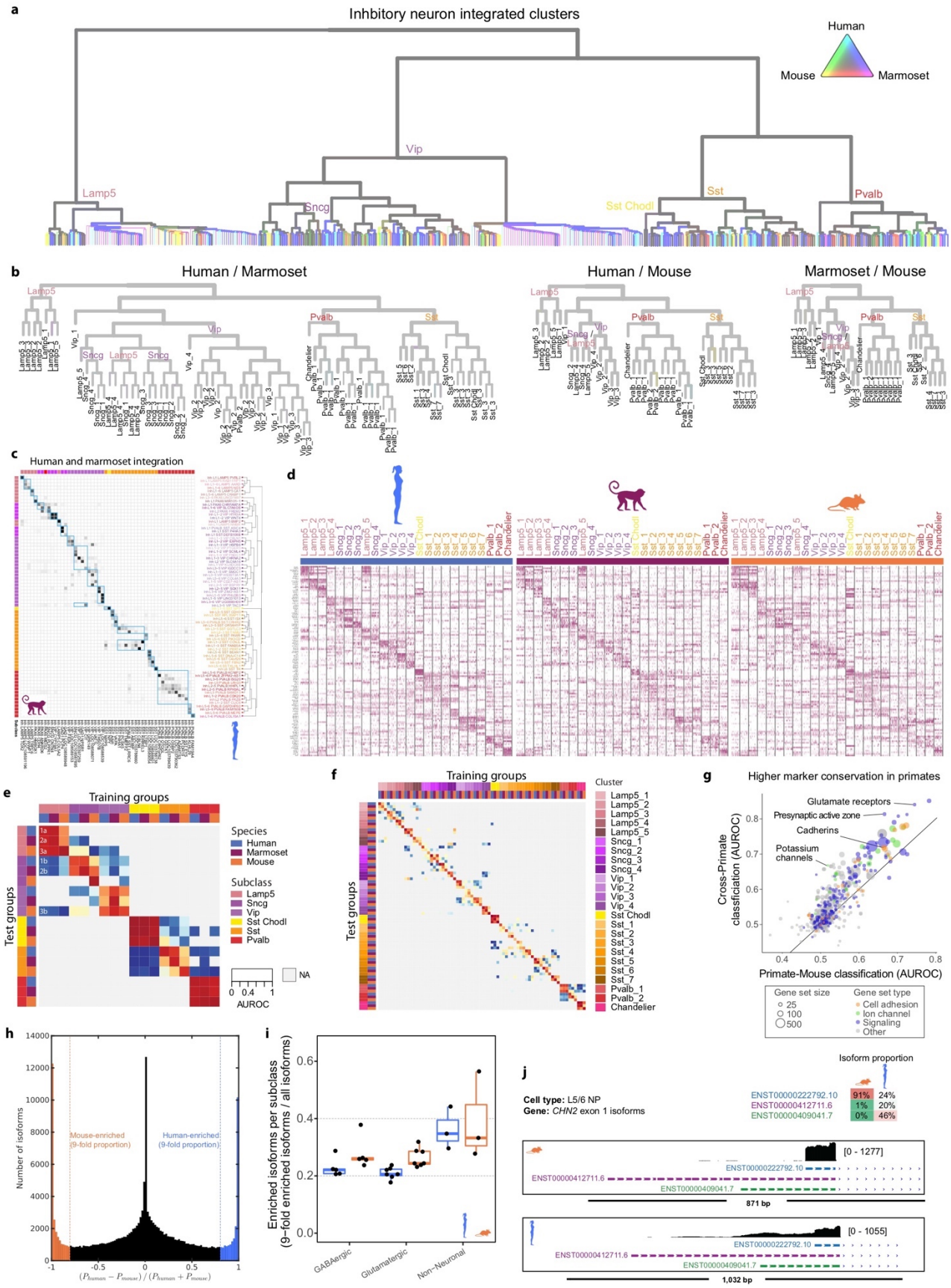
a
Inhbitory neuron integrated clusters
Human
Mouse
Marmoset
Lamp5
Sncg
Vip
Sst Chodl
Sst
Pvalb
b
Human / Marmoset
Human / Mouse
Marmoset / Mouse
c
Human and marmoset integration
d
e
Training groups
Test groups
Species
Human
Marmoset
Mouse
Subclass
Lamp5
Sncg
Vip
Sst Chodl
Sst
Pvalb
NA
AUROC
f
Training groups
Test groups
Cluster
g
Higher marker conservation in primates
Glutamate receptors
Presynaptic active zone
Cadherins
Potassium channels
Cross-Primate classification (AUROC)
Primate-Mouse classification (AUROC)
Gene set size
25
100
500
Gene set type
Cell adhesion
Ion channel
Signaling
Other
h
Number of isoforms
Mouse-enriched (9-fold proportion)
Human-enriched (9-fold proportion)
i
Enriched isoforms per subclass (9-fold enriched isoforms / all isoforms)
GABAergic
Glutamatergic
Non-Neuronal
j
Isoform proportion
Cell type: L5/6 NP
Gene: CHN2 exon 1 isoforms
ENST00000222792.10
ENST00000412711.6
ENST00000409041.7
91%
24%
1%
20%
0%
46%
[0 - 1277]
871 bp
[0 - 1055]
1,032 bp

073

074 **Extended Data Figure 2. RNA-seq integration of GABAergic neurons across species. a**,
075 Dendrogram of GABAergic neuron clusters from unsupervised clustering of integrated RNA-seq data
076 from human, marmoset and mouse. Edge thickness indicates the relative number of nuclei, and edge
077 color indicates species mixing (grey is well mixed). Major branches are labeled by subclass.
078 Dendrogram shown in **Figure 2f** is derived from this tree based on pruning species-specific branches.
079 **b,** Dendrograms of pairwise species integrations from **Figure 2g** with leaves labeled by cross-species
080 clusters and edges colored by species mixing. **c,** Cluster overlap heatmap from human-marmoset
081 pairwise Seurat integration showing the proportion of within-species clusters that coalesce within
082 integrated clusters. Columns and rows are ordered as in **Figure 2e** with cross-species consensus
083 clusters indicated by blue boxes. Top and left color bars indicate subclasses of within-species clusters.
084 **d,** Heatmaps showing scaled expression of the top 5 marker genes for each GABAergic cross-species
085 cluster, and 5 marker genes for *Lamp5* and *Sst*. Initial genes were identified by performing a Wilcox test
086 of every integrated cluster against every other GABAergic nuclei. Additional DEGs were identified for
087 *Lamp5* and *Sst* cross-species clusters, by comparing one of the cross-species clusters to all other
088 related nuclei (e.g. *Sst*_1 against all other *Sst*). **e-f,** Heatmap of 1-vs-best MetaNeighbor scores for
089 GABAergic subclasses (**e**) and clusters (**f**). Each column shows the performance for a single training
090 group across the three test datasets. AUROCs are computed between the two closest neighbors in the
091 test dataset, where the closer neighbor will have the higher score, and all others are shown in gray
092 (NA). For example, in **e** the first column contains results of training on human *Lamp5*, labeled with
093 numbers to indicate test datasets, where 1 is human, 2 is marmoset and 3 is mouse, and letters to
094 indicate closest (**a**) and second-closest (**b**) neighboring groups. Dark red 3x3 blocks along the diagonal
095 indicate high transcriptomic similarity across all three species. **g**, Scatter plot of MetaNeighbor analysis
096 showing the performance (AUROC) of gene sets to classify GABAergic neuron consensus types by
097 training with human or marmoset data and testing with the other species (Cross-Primate, y-axis) or
098 training with primate data and testing with mouse (Primate-Mouse, x-axis). Gene set size and type are
099 indicated by point size and color, respectively. **h**, Histogram of the relative difference in isoform genic

100 proportion (P) between human and mouse for all subclass comparisons. All moderately to highly
101 expressed isoforms were included (gene TPM > 10 in both species; isoform TPM > 10 and proportion >
102 0.2 in either species). Vertical lines indicate >9-fold change in mouse or human. **i**, Proportion of all
103 isoforms in **h** that switch between species (FDR P < 0.05; >9-fold change in P) summarized by
104 subclass and grouped by cell class. **j**, Comparison between species of isoform genic proportions for the
105 top three most common isoforms of Chimerin 2 (*CHN2*) expressed in the L5/6 NP subclass. Genome
106 browser tracks of RNA-seq (SSv4) reads in human and mouse at the *CHN2* locus.
107

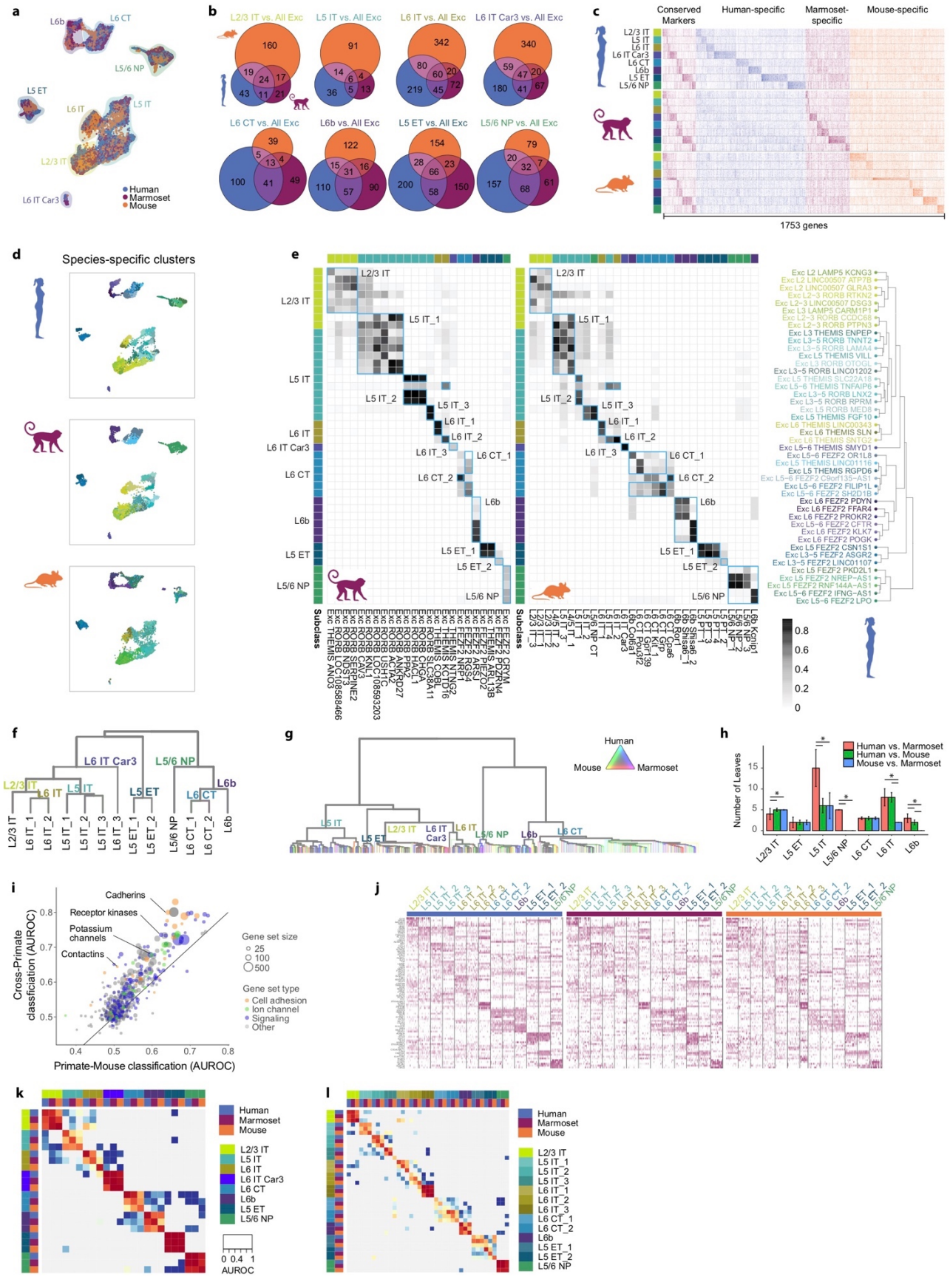
a
L6b
L6 CT
L5/6 NP
L5 ET
L6 IT
L5 IT
L2/3 IT
L6 IT Car3
Human
Marmoset
Mouse
b
L2/3 IT vs. All Exc
L5 IT vs. All Exc
L6 IT vs. All Exc
L6 IT Car3 vs. All Exc
L6 CT vs. All Exc
L6b vs. All Exc
L5 ET vs. All Exc
L5/6 NP vs. All Exc
c
Conserved Markers
Human-specific
Marmoset-specific
Mouse-specific
1753 genes
d
Species-specific clusters
e
Subclass
f
g
Human
Mouse
Marmoset
h
Human vs. Marmoset
Human vs. Mouse
Mouse vs. Marmoset
Number of Leaves
i
Cadherins
Receptor kinases
Potassium channels
Contactins
Cross-Primate classification (AUROC)
Primate-Mouse classification (AUROC)
Gene set size
Gene set type
Cell adhesion
Ion channel
Signaling
Other
j
k
Human
Marmoset
Mouse
AUROC
l

Extended Data Figure 3. Glutamatergic neuron cell type homology across species. a, UMAP visualization of integrated snRNA-seq data from human, marmoset, and mouse glutamatergic neurons. Highlighted colors indicate subclass. **b,** Venn diagrams indicating number of shared DEGs across species by subclass. DEGs determined by ROC test of subclass against all other glutamatergic subclasses within a species. **c,** Heatmap of all DEGs from **b** ordered by subclass and species enrichment. Heatmap shows expression scaled by column for up to 50 randomly sampled nuclei from each subclass for each species. **d,** UMAP visualization of integrated snRNA-seq data with projected nuclei split by species. Colors indicate different within-species clusters. **e,** Cluster overlap heatmap showing the proportion of within-species clusters that coalesce with a given integrated cross-species cluster. Cross-species clusters are labelled and indicated by blue boxes with human-marmoset overlap shown to the left and human-mouse overlap shown to the right. Top and left axes indicate the subclass of a given within-species cluster by color. Bottom axis indicates marmoset (left) and mouse (right) within species clusters. Right axis shows the glutamatergic branch of the human dendrogram from **Figure 1c**. **f,** Dendrogram of glutamatergic neuron cross-species clusters. **g,** Unpruned dendrogram of glutamatergic neuron clusters from unsupervised clustering of integrated RNA-seq data. Edge thickness indicates the relative number of nuclei, and edge color indicates species mixing. Major branches are labeled by subclass. **h**, Bar plots quantifying the number of well-mixed clusters from unsupervised clustering of pairwise species integrations. Significant differences (adjusted $P < 0.05$, Tukey's HSD test) between species are indicated for each subclass. **i,** Scatter plot of MetaNeighbor analysis showing the performance (AUROC) of gene sets to classify glutamatergic neuron consensus types by training with human or marmoset data and testing with the other species (Cross-Primate, y-axis) or training with primate data and testing with mouse (Primate-Mouse, x-axis). Gene set size and type are indicated by point size and color, respectively. **j,** Heatmaps showing scaled expression of marker genes for each glutamatergic cross-species cluster. The top 5 marker genes for each cross-species cluster are shown, with an additional 5 genes for L5 ET, L5 IT, and L6 IT. Initial genes were identified by performing a Wilcox test of every integrated cluster against every other glutamatergic

135 nuclei. Additional DEGs were identified for L5 ET, L5 IT, and L6 IT cross-species clusters, by

136 comparing one of the cross-species clusters to all other related nuclei (e.g. L5 IT_1 against all other L5

137 IT). **k**, **l,** Heatmap of 1-vs-best MetaNeighbor scores for glutamatergic subclasses (**k**) and clusters (**l**).

138 Results are displayed as in **Extended Data Fig. 2e,f**.

139

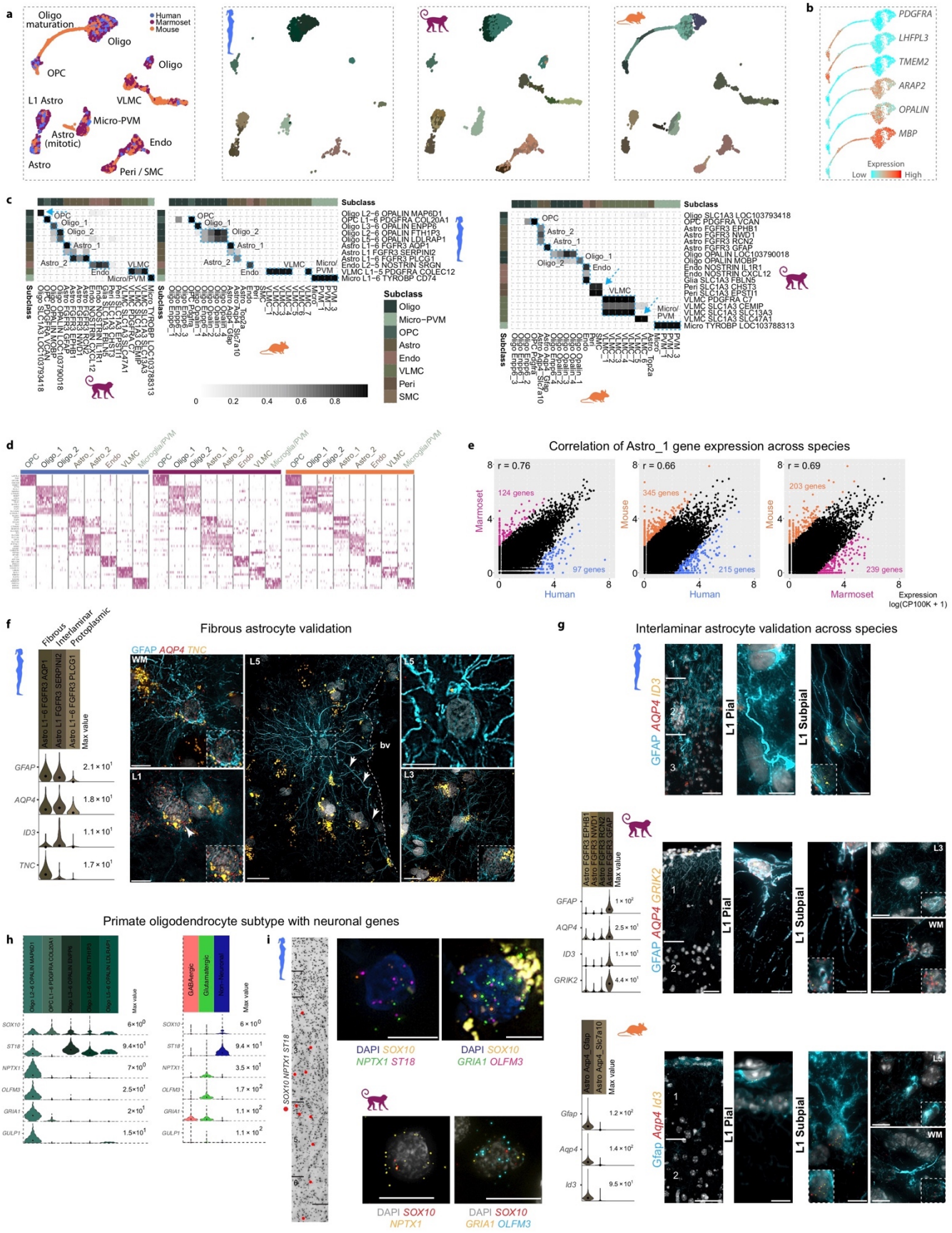
a
Oligo maturation
Human
Marmoset
Mouse
Oligo
OPC
Oligo
L1 Astro
VLMC
Micro-PVM
Astro (mitotic)
Endo
Astro
Peri / SMC
b
PDGFRA
LHFPL3
TMEM2
ARAP2
OPALIN
MBP
Expression
Low
High
c
Subclass
Oligo
Micro−PVM
OPC
Astro
Endo
VLMC
Peri
SMC
d
e
Correlation of Astro_1 gene expression across species
r = 0.76
124 genes
97 genes
Marmoset
Human
r = 0.66
345 genes
215 genes
Mouse
Human
r = 0.69
203 genes
239 genes
Mouse
Marmoset
Expression log(CP100K + 1)
f
Fibrous astrocyte validation
Fibrous
Interlaminar
Protoplasmic
Max value
GFAP
AQP4
ID3
TNC
GFAP AQP4 TNC
WM
L5
L1
L3
bv
g
Interlaminar astrocyte validation across species
GFAP AQP4 ID3
L1 Pial
L1 Subpial
GFAP AQP4 GRIK2
L3
WM
Gfap Aqp4 Id3
L5
h
Primate oligodendrocyte subtype with neuronal genes
SOX10
ST18
NPTX1
OLFM3
GRIA1
GULP1
GABAergic
Glutamatergic
Non-Neuronal
i
SOX10 NPTX1 ST18
DAPI SOX10 NPTX1 ST18
DAPI SOX10 GRIA1 OLFM3
DAPI SOX10 NPTX1
DAPI SOX10 GRIA1 OLFM3

141 **Extended Data Figure 4. Non-neuronal cell type homology across species. a**, UMAP plots of
142 integrated RNA-seq data for non-neuronal nuclei, colored by species and within-species clusters. Note
143 that some cell types are present in only one or two species. **b**, UMAP of mouse oligodendrocyte
144 precursors and mature cells showing expression levels of marker genes for different stages of cell
145 maturation. **c**, Heatmaps of the proportion of nuclei in each species-specific cluster that overlap in the
146 integrated RNA-seq analysis. Blue boxes define homologous cell types that can be resolved across all
147 three species. Arrows highlight clusters that overlap between two species and are not detected in the
148 third species, due to differences in sampling depth of non-neuronal cells, relative abundances of cell
149 types between species, or evolutionary divergence. **d**, Conserved marker genes for homologous cell
150 types across species. **e**, Pairwise comparisons between species of log-transformed gene expression of
151 the Astro_1 type. Colored points correspond to significantly differentially expressed (DE) genes (FDR <
152 0.01, log-fold change > 2). r, Spearman correlation. **f**, Fibrous astrocyte in situ validation. Violin plots of
153 marker genes of human astrocyte clusters that correspond to fibrous, interlaminar, and protoplasmic
154 types based on in situ labeling of types. Left ISH: Fibrous astrocytes located in the white matter (WM,
155 top) and a subset of L1 (bottom) astrocytes express the Astro L1-6 *FGFR3 AQP1* marker gene *TNC*.
156 Middle ISH: Image of putative varicose projection astrocyte located in cortical L5 adjacent to a blood
157 vessel (bv) and extending long GFAP-labeled processes (white arrows) does not express the marker
158 gene *TNC*. The white dashed box indicates the area shown at higher magnification in the top right
159 panel. Likewise, the L3 protoplasmic astrocyte shown in the bottom right panel does not express *TNC*.
160 **g**, Combined GFAP immunohistochemistry and RNAscope FISH for markers of L1 astrocytes in
161 human, mouse, and marmoset. In human (top), pial and subpial interlaminar astrocytes are labeled with
162 *AQP4* and *ID3* and extend long processes from L1 down to L3. In marmoset (middle), both pial and
163 subpial L1 astrocytes express *AQP4* and *GRIK2* and extend GFAP-labeled processes through L1 that
164 terminate before reaching L2. An image of a marmoset protoplasmic astrocyte located in L3 shows that
165 this astrocyte type does not express the marker gene *GRIK2*. A subset of marmoset fibrous astrocytes
166 located in the white matter (WM) express *GRIK2*, suggesting that fibrous and L1 astrocytes have a

167 shared gene expression signature as shown in human [2]. L1 astrocytes in mouse (bottom) consist of pial
168 and subpial types that differ morphologically but are characterized by their expression of the genes
169 *Aqp4* and *Id3*. Pial astrocytes in mouse extend short Gfap-labeled processes that terminate within L1
170 whereas mouse subpial astrocytes appear to extend processes predominantly toward the pial surface.
171 Protoplasmic astrocytes (example shown in L5) do not express *Id3*, whereas fibrous astrocytes in
172 mouse share expression of *Id3* with L1 astrocyte types. Inset images outlined with white dashed boxes
173 illustrate cells in each of the accompanying images at higher magnification to show RNAscope spots for
174 each gene labeled. Scale bars, 20 μm. **h**, Violin plots of marker genes of oligodendrocyte lineage
175 clusters in human. Transcripts detected in the Oligo L2−6 *OPALIN MAP6D1* cluster include genes
176 expressed almost exclusively in neuronal cells. Scale bars, 20 μm. **i**, Left: Inverted DAPI image
177 showing a column of cortex labeled with markers of the human Oligo L2-6 *OPALIN MAP6D1* type. Red
178 dots show cells triple labeled with *SOX10*, *NPTX1*, and *ST18*. Top right: Examples of cells labeled with
179 marker gene combinations specific for the human Oligo L2-6 *OPALIN MAP6D1* type. Bottom right:
180 Example of a marmoset cell labeled with the marker genes *OLIG2* and *NRXN3*. Scale bars, 20 μm.
181

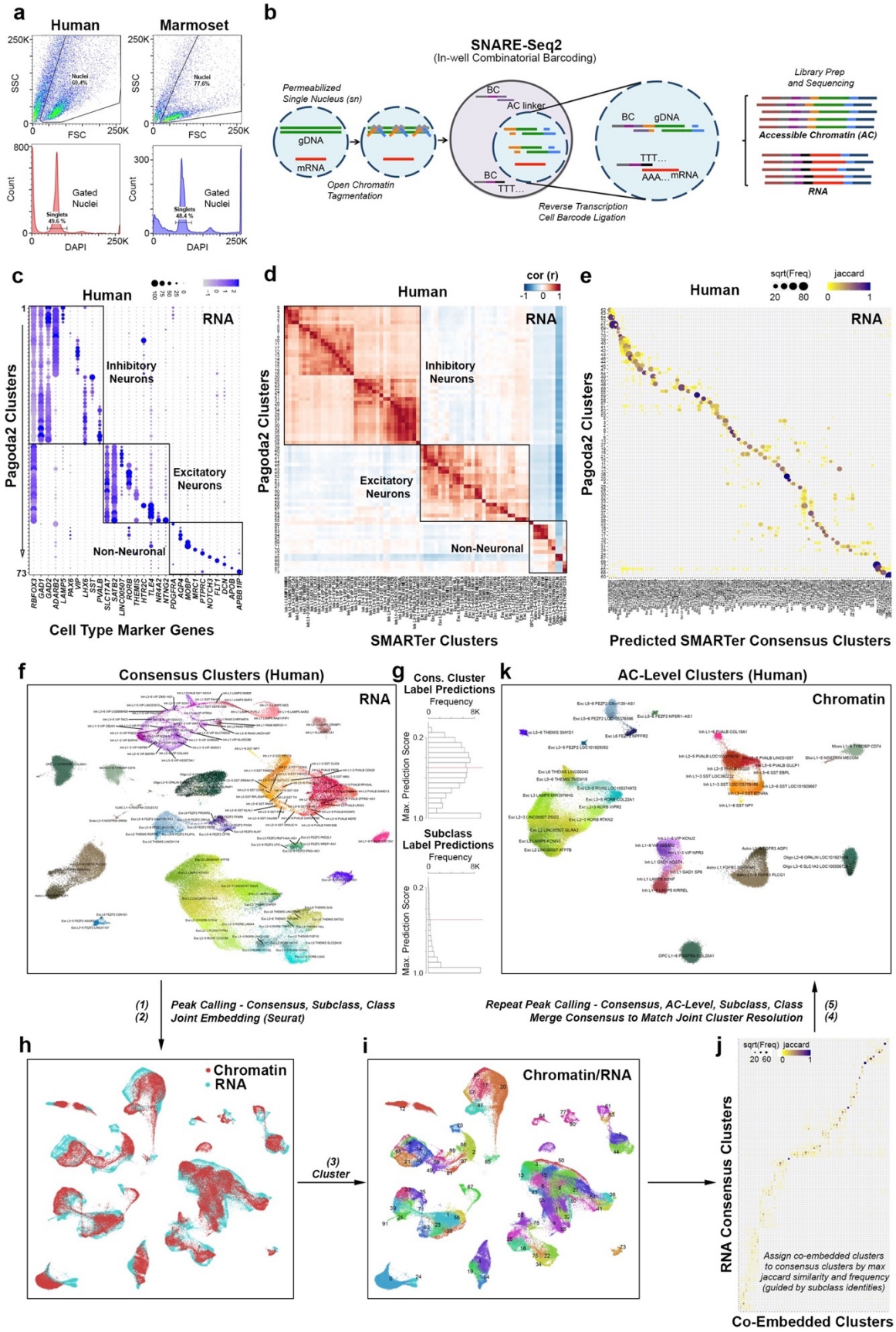
a
Human
Marmoset
SSC
FSC
Nuclei
Count
Gated Nuclei
Singlets
DAPI
b
SNARE-Seq2
(In-well Combinatorial Barcoding)
Permeabilized Single Nucleus (sn)
gDNA
mRNA
Open Chromatin Tagmentation
BC
AC linker
TTT...
Reverse Transcription Cell Barcode Ligation
AAA... mRNA
Library Prep and Sequencing
Accessible Chromatin (AC)
RNA
c
Human
RNA
Pagoda2 Clusters
Inhibitory Neurons
Excitatory Neurons
Non-Neuronal
Cell Type Marker Genes
d
Human
cor (r)
RNA
Pagoda2 Clusters
Inhibitory Neurons
Excitatory Neurons
Non-Neuronal
SMARTer Clusters
e
Human
sqrt(Freq)
jaccard
RNA
Pagoda2 Clusters
Predicted SMARTer Consensus Clusters
f
Consens Clusters (Human)
RNA
g
Cons. Cluster Label Predictions
Frequency
Max. Prediction Score
Subclass Label Predictions
k
AC-Level Clusters (Human)
Chromatin
(1) Peak Calling - Consensus, Subclass, Class
(2) Joint Embedding (Seurat)
Repeat Peak Calling - Consensus, AC-Level, Subclass, Class
Merge Consensus to Match Joint Cluster Resolution
(5)
(4)
h
Chromatin
RNA
(3) Cluster
i
Chromatin/RNA
j
sqrt(Freq)
jaccard
RNA Consensus Clusters
Assign co-embedded clusters to consensus clusters by max jaccard similarity and frequency (guided by subclass identities)
Co-Embedded Clusters

Extended Data Figure 5. SNARE-seq2 transcriptomic profiling resolves M1 cell types. **a-b**, FACS gating parameters used for sorting human and marmoset single nuclei (**a**) that were used for SNARE-seq2 as outlined in (**b**), to generate both RNA and accessible chromatin (AC) libraries having the same cell barcodes. **c**, Dot plot showing averaged marker gene expression values (log scale) and proportion expressed for clusters identified in a preliminary analysis of SNARE-seq2 RNA using Pagoda2. **d**, Correlation heatmap of averaged scaled gene expression values for Pagoda2 clusters against SSv4 clusters from the same M1 region. **e**, Jaccard similarity plot for cell barcodes grouped according to Pagoda2 clustering compared against the predicted SSv4 consensus clustering. **f-k**, Overview of AC-level cluster assignment using RNA-defined clusters indicating the five main steps of the process. **f**, Consensus clusters visualized by UMAP on RNA expression data and that were used to independently call peaks from AC data. **g**, Histograms showing maximum prediction scores for consensus cluster (top) and subclass (bottom) labels from RNA data to corresponding accessibility data (cicero gene activities). **h**, Consensus cluster peaks, as well as those identified from subclass and class level barcode groupings, were combined and the corresponding peak by cell barcode matrix was used to predict gene activity scores using Cicero for integrative RNA/AC analyses. UMAP shows joint embedding of RNA and imputed AC expression values using Seurat/Signac. **i**, UMAP showing clusters identified from the joint embedding (**h**). **j**, Jaccard similarity plot comparing cell barcodes either grouped according to RNA consensus clustering or joint RNA/AC clustering (**i**). RNA consensus clusters were merged to best match the cluster resolution achieved from co-embedded clusters. Chromatin peak counts generated from peak calling independently on consensus, AC-level, subclass, and class barcode groupings were used to generate a final peak by cell barcode matrix. **k**, Final AC-level clusters visualized using UMAP.

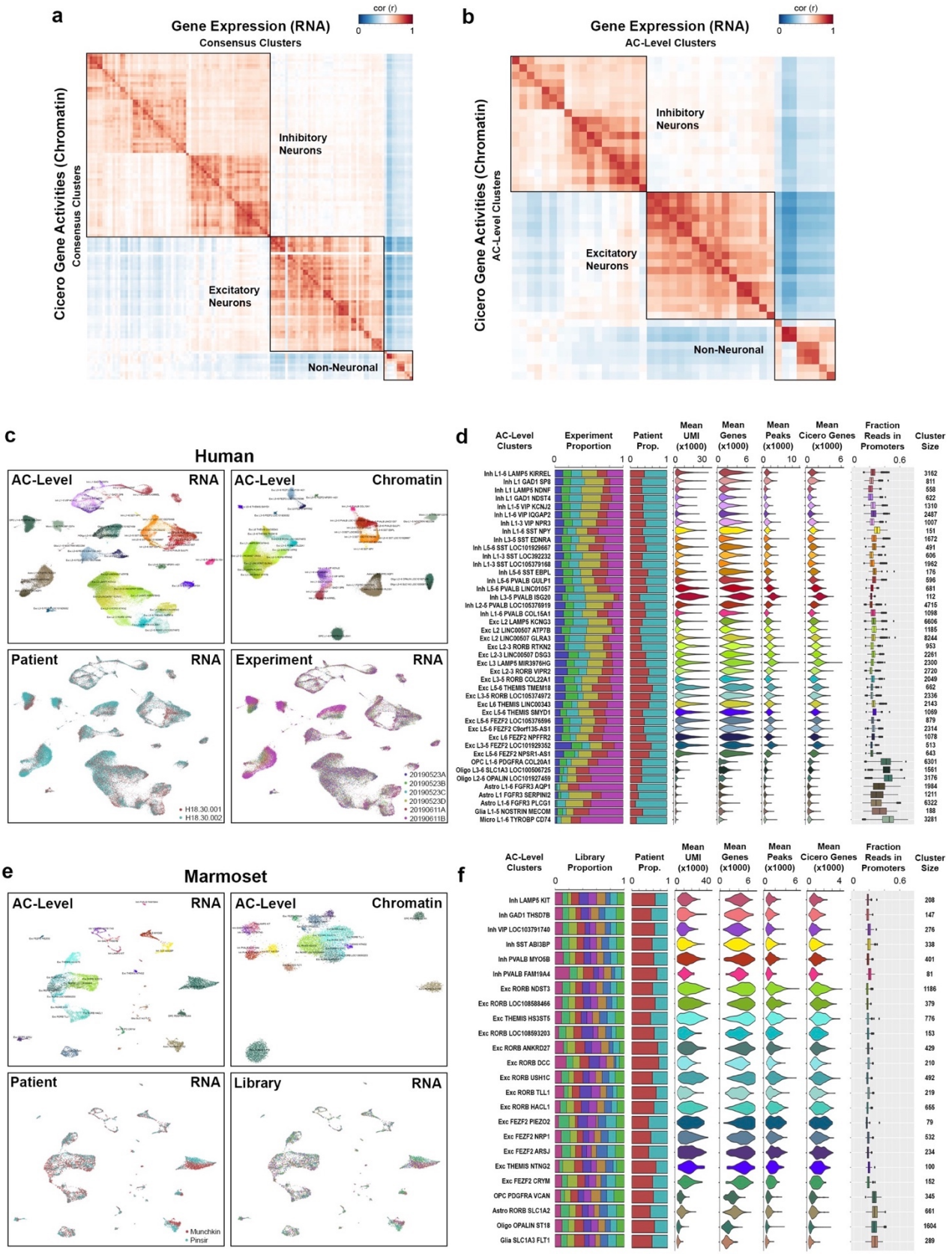
a
Gene Expression (RNA)
Consensus Clusters
cor (r)
0
1
Cicero Gene Activities (Chromatin)
Consensus Clusters
Inhibitory Neurons
Excitatory Neurons
Non-Neuronal
b
Gene Expression (RNA)
AC-Level Clusters
cor (r)
0
1
Cicero Gene Activities (Chromatin)
AC-Level Clusters
Inhibitory Neurons
Excitatory Neurons
Non-Neuronal
c
Human
AC-Level
RNA
AC-Level
Chromatin
Patient
RNA
Experiment
RNA
H18.30.001
H18.30.002
20190523A
20190523B
20190523C
20190523D
20190611A
20190611B
d
AC-Level Clusters
Experiment Proportion
Patient Prop.
Mean UMI (x1000)
Mean Genes (x1000)
Mean Peaks (x1000)
Mean Cicero Genes (x1000)
Fraction Reads in Promoters
Cluster Size
Inh L1-6 LAMP5 KIRREL 3162
Inh L1 GAD1 SP9 811
Inh L1 LAMP5 NDNF 558
Inh L1 GAD1 NDST4 622
Inh L1-5 VIP KCNJ2 1310
Inh L1-6 VIP IQGAP2 2487
Inh L1-3 VIP NPR3 1007
Inh L1-6 SST NPY 151
Inh L3-5 SST EDNRA 1672
Inh L5-6 SST LOC101929667 491
Inh L1-3 SST LOC392232 606
Inh L1-3 SST LOC105379168 1962
Inh L5-6 SST EBPL 176
Inh L5-6 PVALB GULP1 596
Inh L5-6 PVALB LINC01057 681
Inh L3-5 PVALB ISG20 112
Inh L2-5 PVALB LOC105376919 4715
Inh L1-6 PVALB COL15A1 1098
Exc L2 LAMP5 KCNG3 6606
Exc L2 LINC00507 ATP7B 1185
Exc L2 LINC00507 GLRA3 8244
Exc L2-3 RORB RTKN2 953
Exc L2-3 LINC00507 DSG3 2261
Exc L3 LAMP5 MIR3976HG 2300
Exc L2-3 RORB VIPR2 2720
Exc L3-5 RORB COL22A1 2049
Exc L5-6 THEMIS TMEM18 662
Exc L3-5 RORB LOC105374972 2336
Exc L6 THEMIS LINC00343 2143
Exc L5-6 THEMIS SMYD1 1069
Exc L5-6 FEZF2 LOC105376596 879
Exc L5-6 FEZF2 C9orf135-AS1 2314
Exc L6 FEZF2 NPFFR2 1078
Exc L3-5 FEZF2 LOC101929302 513
Exc L5-6 FEZF2 NPSR1-AS1 643
OPC L1-6 PDGFRA COL20A1 6301
Oligo L3-6 SLC1A3 LOC100506725 1551
Oligo L2-6 OPALIN LOC101927459 3176
Astro L1-6 FGFR3 AQP1 1984
Astro L1 FGFR3 SERPINI2 1211
Astro L1-6 FGFR3 PLCG1 6322
Glia L1-5 NOSTRIN MECOM 188
Micro L1-6 TYROBP CD74 3281
e
Marmoset
AC-Level
RNA
AC-Level
Chromatin
Patient
RNA
Library
RNA
Munchkin
Pinsir
f
AC-Level Clusters
Library Proportion
Patient Prop.
Mean UMI (x1000)
Mean Genes (x1000)
Mean Peaks (x1000)
Mean Cicero Genes (x1000)
Fraction Reads in Promoters
Cluster Size
Inh LAMP5 KIT 208
Inh GAD1 THSD7B 147
Inh VIP LOC103791740 276
Inh SST ABI3BP 338
Inh PVALB MYO5B 401
Inh PVALB FAM19A4 81
Exc RORB NDST3 1186
Exc RORB LOC108588466 379
Exc THEMIS HS3ST5 776
Exc RORB LOC108593203 153
Exc RORB ANKRD27 429
Exc RORB DCC 210
Exc RORB USH1C 492
Exc RORB TLL1 219
Exc RORB HACL1 655
Exc FEZF2 PIEZO2 79
Exc FEZF2 NRP1 532
Exc FEZF2 ARSJ 234
Exc THEMIS NTNG2 100
Exc FEZF2 CRYM 152
OPC PDGFRA VCAN 345
Astro RORB SLC1A2 661
Oligo OPALIN ST18 1604
Glia SLC1A3 FLT1 289

Extended Data Figure 6. SNARE-Seq2 quality statistics. a-b, Correlation heatmaps of average scaled gene expression values against average scaled Cicero gene activity values for consensus clusters (**a**) and AC-level clusters (**b**). **c**, UMAP plots showing human AC-level clusters for both RNA and chromatin data, as well as the corresponding patient and experiment identities for the RNA embeddings. **d**, Bar, violin and box plots for human AC-level clusters showing proportion contributed by each experiment or patient, mean UMI and genes detected from the RNA data, the mean peaks and cicero active genes detected from AC data, the fraction of reads found in promoters for AC data, and the number of nuclei making up each of the clusters. **e**, UMAP plots showing marmoset AC-level clusters for both RNA and chromatin data, as well as the corresponding patient and library identities for the RNA embeddings. **f**, Bar, violin and box plots for marmoset AC-level clusters showing proportion contributed by each library or patient, mean UMI and genes detected from the RNA data, the mean peaks and cicero active genes detected from AC data, the fraction of reads found in promoters for AC data, and the number of nuclei making up each of the clusters.

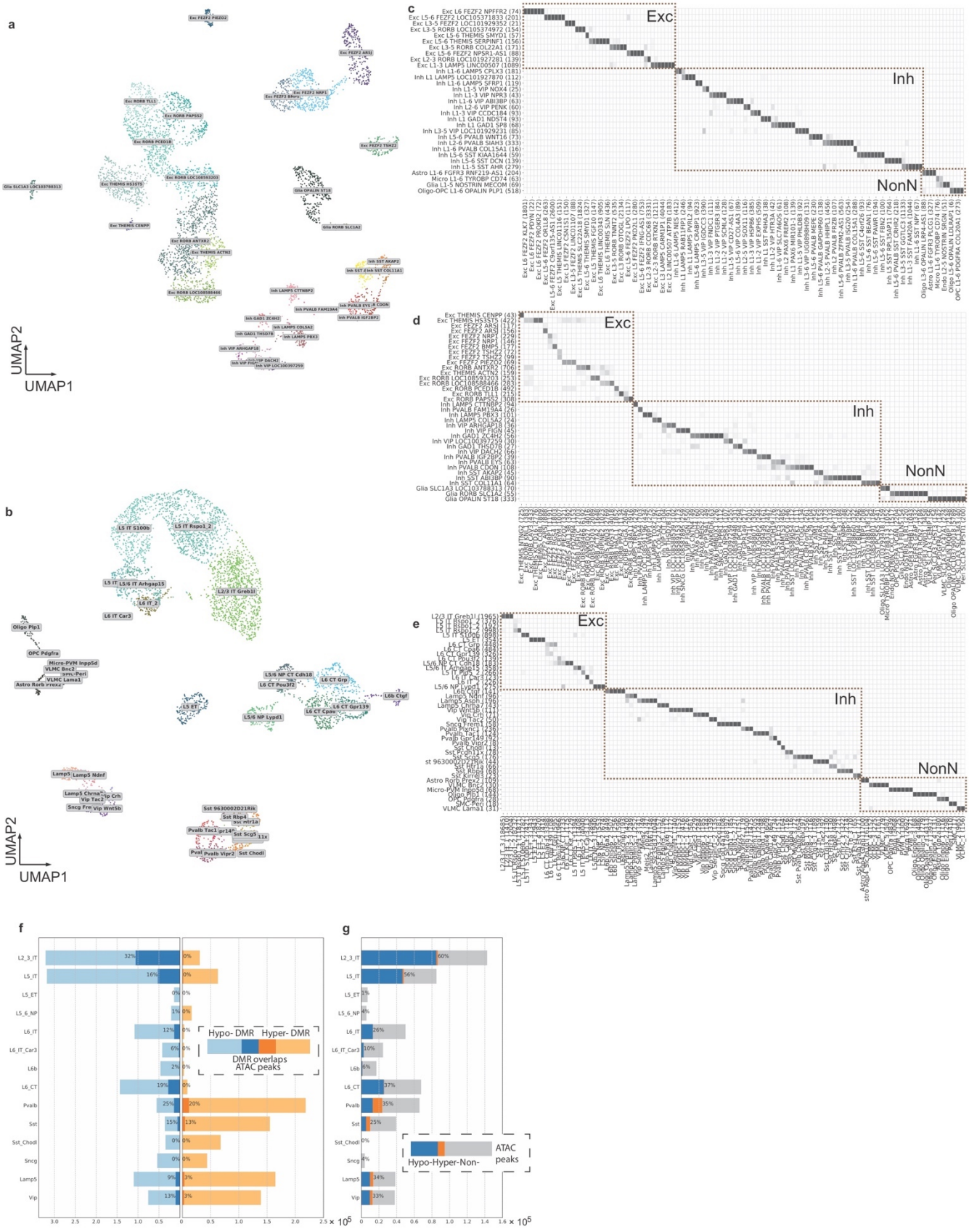
a
UMAP2
UMAP1
b
UMAP2
UMAP1
c
Exc
Inh
NonN
d
Exc
Inh
NonN
e
Exc
Inh
NonN
f
Hypo- DMR
Hyper- DMR
DMR overlaps ATAC peaks
L2_3_IT
L5_IT
L5_ET
L5_6_NP
L6_IT
L6_IT_Car3
L6b
L6_CT
Pvalb
Sst
Sst_Chodl
Sncg
Lamp5
Vip
× 10^5
g
Hypo-Hyper-Non-
ATAC peaks
× 10^5

Extended Data Figure 7. DNA-methylation cell type and integration with RNA-seq data. a-b, UMAP visualization of marmoset M1 and mouse MOp DNA methylation (snmC-seq2) data and cell clusters. **c-e,** Mapping between DNAm-seq and RNA-seq clusters from human (**c**), marmoset (**d**), and mouse (**e**). Number of nuclei in each cluster are listed in parentheses. **f,** Numbers of hypo- and hyper-methylated DMRs and overlap with chromatin accessible peaks in each subclass of human. **g,** Numbers of chromatin accessible peaks and overlap with DMRs in each subclass of human.

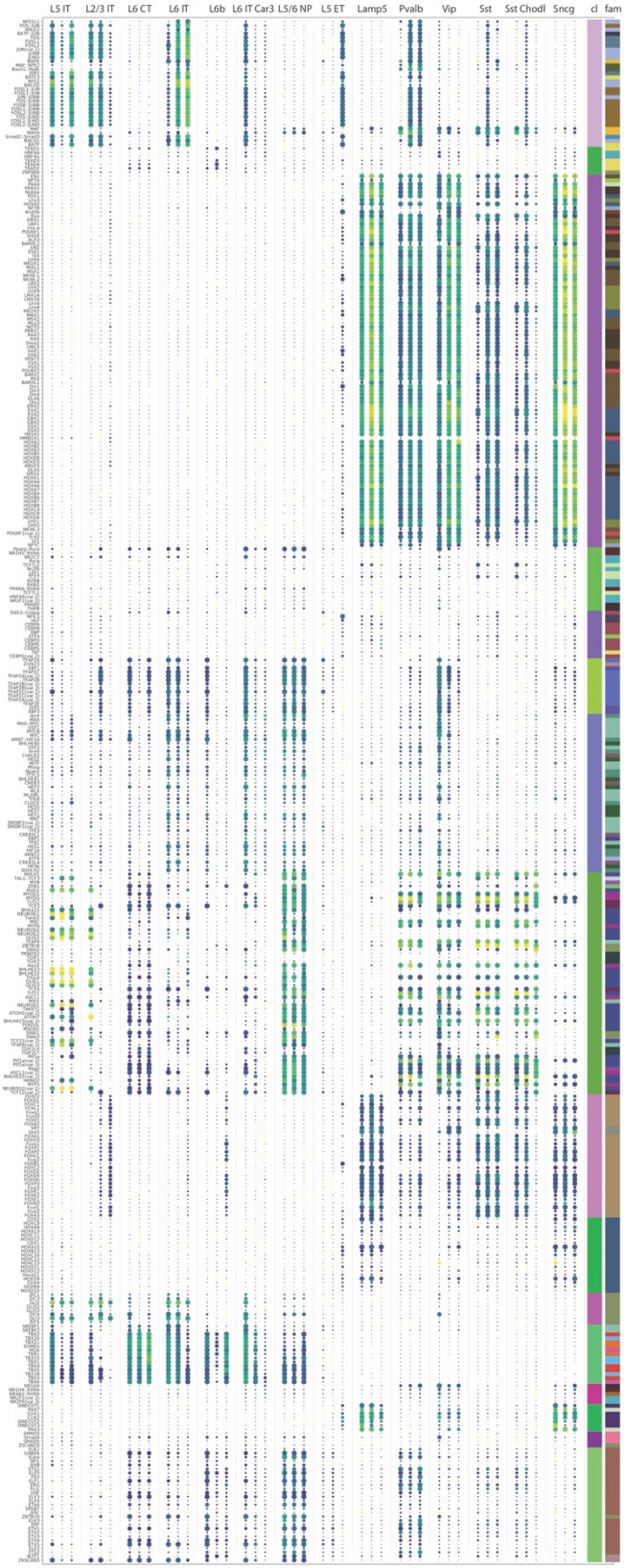
L5 IT
L2/3 IT
L6 CT
L6 IT
L6b
L6 IT Car3
L5/6 NP
L5 ET
Lamp5
Pvalb
Vip
Sst
Sst Chodl
Sncg
cl
fam

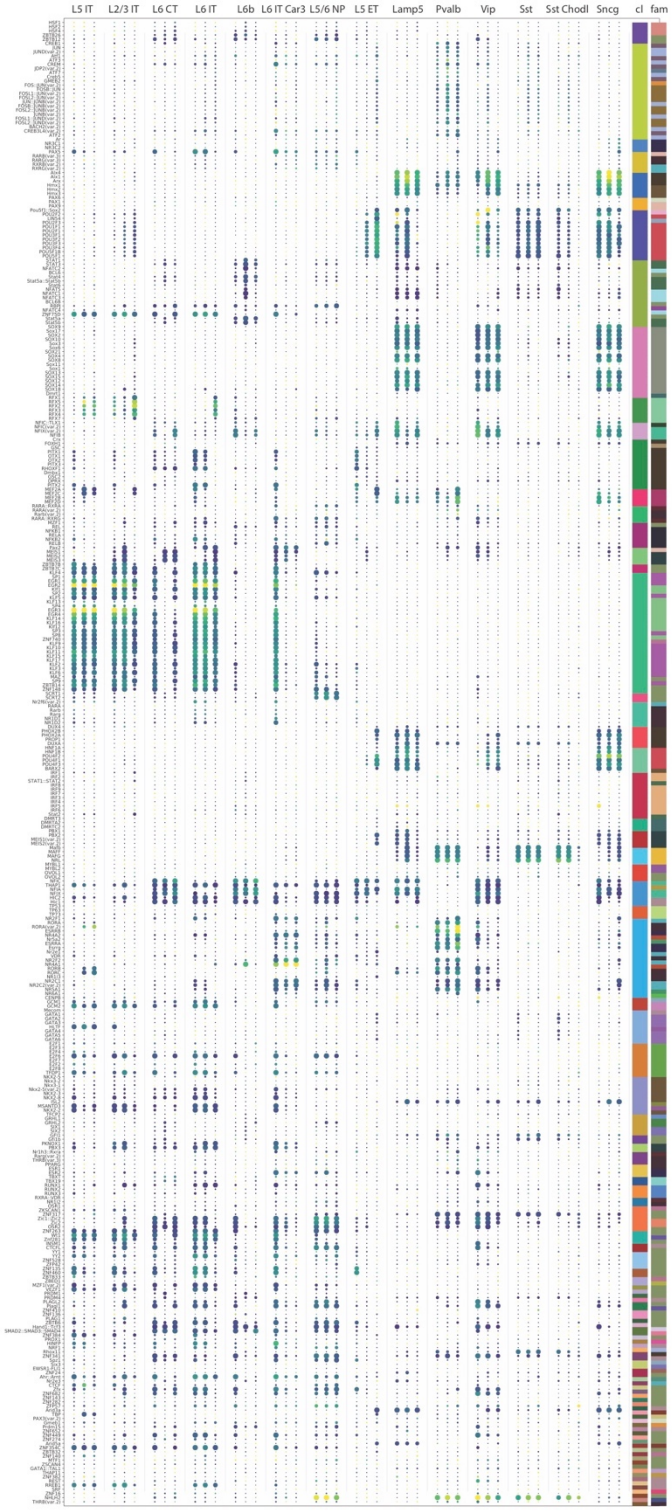
L5 IT
L2/3 IT
L6 CT
L6 IT
L6b
L6 IT Car3
L5/6 NP
L5 ET
Lamp5
Pvalb
Vip
Sst
Sst Chodl
Sncg
cl
fam

230 **Extended Data Figure 8. TFBS enrichment analysis on hypo-methylated DMRs at subclass level**
231 **show conservativity of gene regulation across species.** Motif enrichment analysis of TFBS were
232 conducted using JASPAR's non-redundant core vertebrata TF motifs for neuronal subclasses in each
233 species. Each subclass tri-column shows the results of human, marmoset and mouse, respectively
234 from left to right. The size of a dot denotes the p-value of the corresponding motif, while the color
235 denotes the fold change. The rightmost two columns show TF clusters (cl) identified from motif profiles
236 and TF family (fam) identified from TF structures.
237

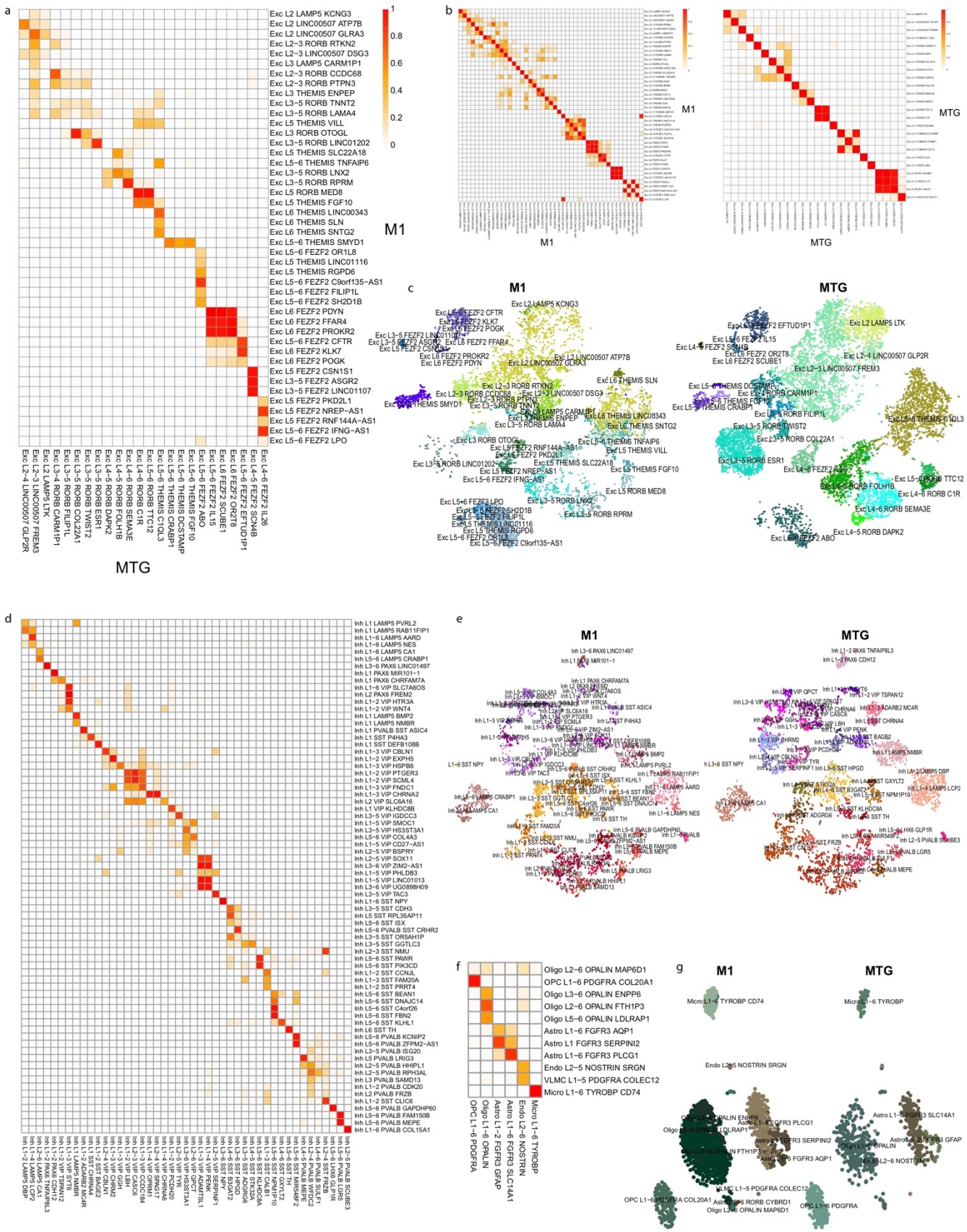
a
M1
MTG
b
M1
MTG
c
M1
MTG
d
e
M1
MTG
f
g
M1
MTG

Extended Data Figure 9. Cell type homologies between human cortical areas based on RNA-seq integration. a, Heatmap of glutamatergic neuron cluster overlap between M1 and MTG. **b**, Heatmaps of glutamatergic neuron cluster overlap for M1 and MTG test datasets. Clusters were split in half and two datasets were integrated using the same analysis pipeline as the M1 and MTG integration. Most clusters mapped correctly (along the diagonal) with some loss in resolution between closely related clusters (red blocks). **c**, tSNE plots of integrated glutamatergic neurons labeled with M1 and MTG clusters. **d-g**, Cluster overlap heatmaps and tSNE plots of integrations of GABAergic neurons (**d**, **e**) and non-neuronal cells (**f**, **g**), as described for glutamatergic neurons.

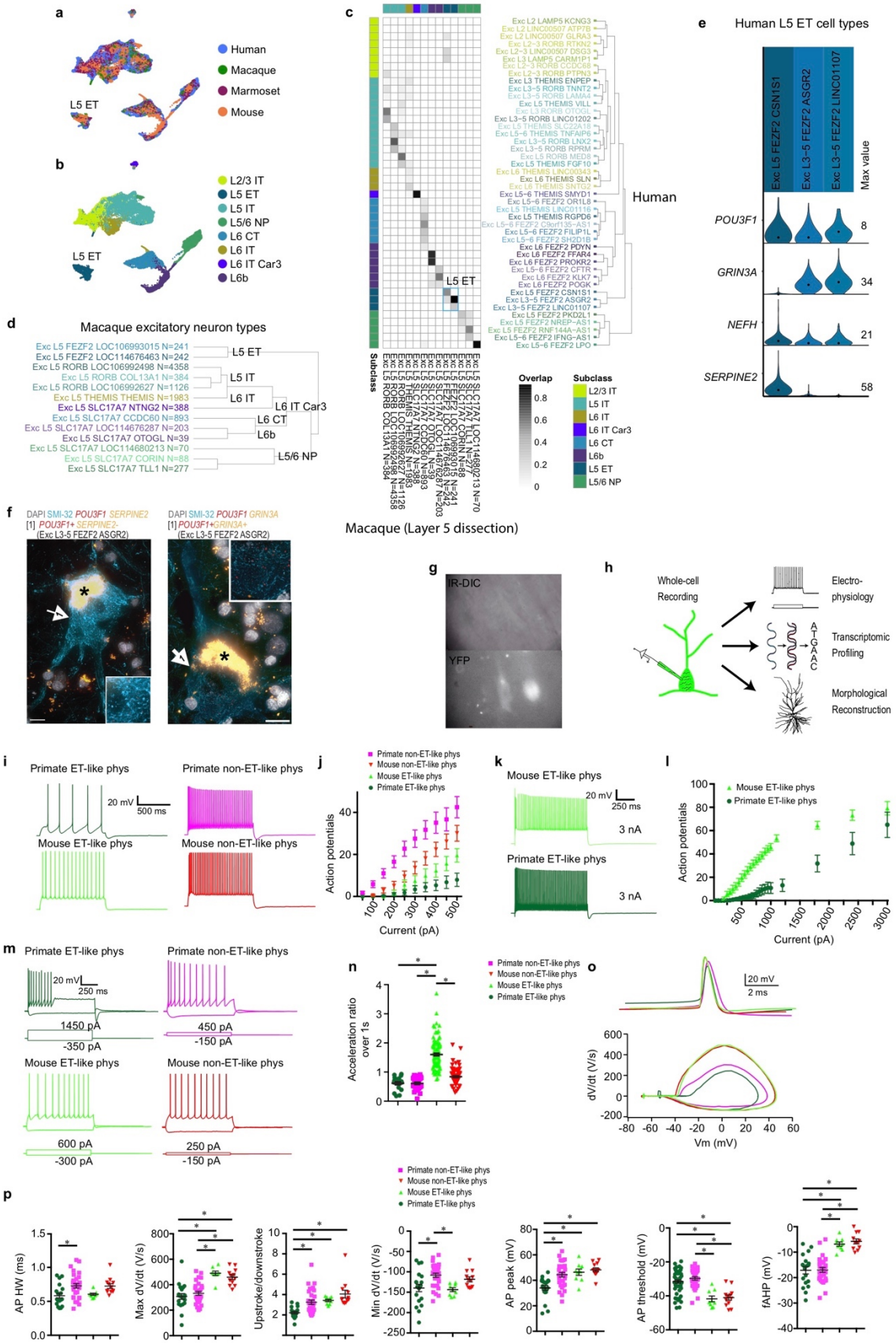
a
Human
Macaque
Marmoset
Mouse
L5 ET
b
L2/3 IT
L5 ET
L5 IT
L5/6 NP
L6 CT
L6 IT
L6 IT Car3
L6b
L5 ET
c
Human
Subclass
Overlap
Subclass
L2/3 IT
L5 IT
L6 IT
L6 IT Car3
L6 CT
L6b
L5 ET
L5/6 NP
Macaque (Layer 5 dissection)
d
Macaque excitatory neuron types
L5 ET
L5 IT
L6 IT
L6 IT Car3
L6 CT
L6b
L5/6 NP
e
Human L5 ET cell types
Exc L5 FEZF2 CSN1S1
Exc L3–5 FEZF2 ASGR2
Exc L3–5 FEZF2 LINC01107
Max value
POU3F1
GRIN3A
NEFH
SERPINE2
f
DAPI SMI-32 POU3F1 SERPINE2
[1] POU3F1+ SERPINE2-
(Exc L3-5 FEZF2 ASGR2)
DAPI SMI-32 POU3F1 GRIN3A
[1] POU3F1+GRIN3A+
(Exc L3-5 FEZF2 ASGR2)
g
IR-DIC
YFP
h
Whole-cell
Recording
Electro-
physiology
Transcriptomic
Profiling
Morphological
Reconstruction
i
Primate ET-like phys
Primate non-ET-like phys
Mouse ET-like phys
Mouse non-ET-like phys
20 mV
500 ms
j
Primate non-ET-like phys
Mouse non-ET-like phys
Mouse ET-like phys
Primate ET-like phys
Action potentials
Current (pA)
k
Mouse ET-like phys
Primate ET-like phys
20 mV
250 ms
3 nA
l
Mouse ET-like phys
Primate ET-like phys
Action potentials
Current (pA)
m
Primate ET-like phys
Primate non-ET-like phys
Mouse ET-like phys
Mouse non-ET-like phys
20 mV
250 ms
1450 pA
-350 pA
450 pA
-150 pA
600 pA
-300 pA
250 pA
-150 pA
n
Primate non-ET-like phys
Mouse non-ET-like phys
Mouse ET-like phys
Primate ET-like phys
Acceleration ratio
over 1s
o
20 mV
2 ms
dV/dt (V/s)
Vm (mV)
p
Primate non-ET-like phys
Mouse non-ET-like phys
Mouse ET-like phys
Primate ET-like phys
AP HW (ms)
Max dV/dt (V/s)
Upstroke/downstroke
Min dV/dt (V/s)
AP peak (mV)
AP threshold (mV)
fAHP (mV)

Extended Data Figure 10. Cross-species alignment of glutamatergic neurons and differences in L5 neuron spike trains and single spike properties. a, b, UMAP visualizations of cross-species integration of snRNA-seq data for glutamatergic neurons isolated from human, macaque (L5 dissection only), marmoset, and mouse. Colors indicate species (**a**) or cell subclass (**b**). **c**, Cluster overlap heatmap showing the proportion of nuclei from within-species clusters that are mixed within the same integrated clusters. Human clusters (rows) are ordered by the dendrogram reproduced from **Figure 1c**. Macaque clusters (columns) are ordered to align with human clusters. Color bars at top and left indicate subclasses of within-species clusters. Blue box denotes the L5 ET subclass. **d,** Dendrogram showing all macaque clusters from L5 dissection with subclasses denoted to the right. **e,** Violin plot showing expression of marker genes for human L5 ET neuron subtypes. **f,** Two examples of ISH labeled, SMI-32 IF stained Betz cells in L5 of human M1 that correspond to the L5 ET cluster Exc L3-5 *FEZF2 ASGR2*. Insets show higher magnification of ISH-labeled transcripts in corresponding cells. Scale bars, 20 µm. Asterisks mark lipofuscin. **g,** Example IR-DIC (top) and fluorescent (bottom) images obtained from a macaque organotypic slice culture. Note the inability to visualize the fluorescently labeled neurons in IR-DIC because of dense myelination. **h**, patch-seq involves the collection of morphological, physiological and transcriptomic data from the same neuron. Following electrophysiological recording and cell filling with biocytin via whole cell patch clamp, the contents of the cell are aspirated and processed for RNA-sequencing. This permits a transcriptomic cell type to be pinned on the physiologically-probed neuron. **i**, Example voltage responses to a 1 s, 500 pA step current injection. **j.** Action potentials as a function of current injection amplitude. Primate ET neurons display shallowest action potential-current injection relationship, perhaps partially because of their exceptionally low input resistance. **k**, Voltage responses to a 1 s, 3 nA step current injection. **l**, Action potentials as a function of current injection for a subset of experiments in which current injection amplitude was increased incrementally to 3 nA. While both mouse and primate ET neurons could sustain high firing rates, primate neurons required 3 nA of current over 1s to reach similar average firing rates as mouse ET neurons. **m**, Example voltage responses to 1 s depolarizing step current injections. The amplitude of

275 the current injection was adjusted to produce ~10 spikes. Also shown are voltage responses to a
276 hyperpolarizing current injection. **n**, The firing rate of primate ET and IT neurons decreased during the 1
277 s step current injection, whereas, the firing rate of mouse ET neurons increased. Acceleration
278 ratio=2nd/last interspike interval. **o**, Example single action potentials (above) and phase plane plots
279 (below). **p**, Various action potential features are plotted as a function of cell type. Notably, action
280 potentials in primate ET neurons were reminiscent of fast spiking interneurons in that they were shorter
281 and more symmetrical compared with action potentials in other neuron types/species. Intriguingly, K^+
282 channel subunits $K_v3.1$ and $K_v3.2$ that are implicated in fast spiking physiology[91] are encoded by highly
283 expressed genes (*KCNC1* and *KCNC2*) in primate ET neurons (Fig. 7c) * $p < 0.05$, Bonferroni
284 corrected t-test.
285

Specimen ID	Age	Sex	Race	Cause of Death	PMI (hr)	Tissue RIN	Hemisphere Sampled	Data Type
H200.1023	43	F	Iranian descent	Mitral valve prolapse	18.5	7.4 ± 0.7	L	SSv4
H200.1025	50	M	Caucasian	Cardiovascular	24.5	7.6 ± 1.0	L	SSv4
H200.1030	54	M	Caucasian	Cardiovascular	25	7.7 ± 0.8	L	SSv4
H18.30.001	60	F	Unknown	Car accident	18	7.9 ± 2.5	R	SSv4, Cv3, SNARE-seq2, sn-methlyome
H18.30.002	50	M	Unknown	Cardiovascular	10	8.2 ± 0.4	R	SSv4, Cv3, SNARE-seq2, snmC-seq2

286 **Extended Data Table 1.** Summary of human tissue donors. RIN, RNA integrity number. Data type:
287 SMART-Seqv4 (SSv4), 10x Genomics Chromium Single Cell 3' Kit v3 (Cv3), Single-Nucleus Chromatin
288 Accessibility and mRNA Expression sequencing (SNARE-seq2), Single-nucleus methylcytosine
289 sequencing (snmC-seq2).

Specimen ID	Age (years)	Sex	Data Type
bi005	2.3	M	Cv3
bi006	3.1	F	Cv3
bi003	1.9	M	FISH

Extended Data Table 2. Summary of marmoset specimens. Data type: 10x Genomics Chromium Single Cell 3' Kit v3 (Cv3). ACD Bio multiplex fluorescent in situ hybridization (FISH).

Supplementary Table legends

Supplementary Table 1. Provisional cell ontology (pCL) terms for human, mouse, and marmoset primary motor cortex cell types. Column headers are described as follows: pCL_id is a unique alphanumeric identifier assigned to each provisional cell type. CL_id is the Cell Ontology (CL) identifier for those parent cell type classes already represented in CL. pCL_name and Transcriptome data cluster are labels given according to each species naming convention that combines information about cortical layer enrichment and genes expressed in data cluster transcriptomes. TDC_id is a unique identifier assigned to the transcriptome data cluster. The part_of (uberon_id) and part_of (uberon_name) columns contain unique identifiers and names for tissue anatomic regions from which the experiment specimen was derived, in this case primary motor cortex. The is_a (CL or pCL_id) and is_a (CL or pCL_name) columns contain parent cell type or provisional cell type identifiers and names, respectively. Cluster_size indicates the number of single-nucleus or cell transcriptomes that were assigned membership to the transcriptome data cluster. Marker_gene_evidence indicates the number of marker genes that are necessary and sufficient to define the transcriptome cell type data cluster with maximal classification accuracy based on the NS-Forest v2.1 algorithm (see Supplementary Tables 4-6). F-measure_evidence is the f-beta score of classification accuracy from the NS-Forest v2.1 algorithm using the marker genes listed. The selectively_expresses column lists the minimum set of marker

genes necessary and sufficient to define the transcriptome cell type data cluster. The definition brings together features to form a data driven ontological representation for each cell type cluster. The pCL annotations are available at https://github.com/mkeshk2018/Provisional_Cell_Ontology and https://bioportal.bioontology.org/ontologies/PCL.

Supplementary Table 2. Cluster annotations for human, marmoset, and mouse in separate worksheets. Cluster_label column identifies the RNA-seq cluster within each species. Cluster_size column denotes the number of nuclei that reside within each cluster (cluster_label). Class column identifies which cell class each cluster belongs to. Subclass column identifies which cell subclass each cluster belongs to. Cross-species cluster column indicates the cross-species consensus cluster taxonomy. DNAm_cluster_label column identifies the transcriptomic cluster (cluster_label) that is aligned to DNAm-determined clusters. ATAC_cluster label column identifies the transcriptomic cluster (cluster_label) that is aligned to ATAC-determined clusters.

Supplementary Table 3. Application of Allen Institute nomenclature schema to mouse, marmoset, and human M1 taxonomies. The “taxonomy_ids” tab lists ids and descriptions for the 11 taxonomies included and which tab those taxonomies are shown on. The “preferred_aliases” tab shows a list of preferred aliases for linking between taxonomies, as well as descriptions for these. The next five tabs show nomenclatures for each of the taxonomies and have the following column headers: “tree_order” is the order shown in the tree (if any); “cell_set_alias”, “cell_set_label”, and “cell_set_accession” are unique identifiers, as described in the Allen Institute nomenclature page (https://portal.brain-map.org/explore/classes/nomenclature), with “cell_set_alias” including the names used in this manuscript; “cell_set_preferred_alias” indicates which clusters correspond to the “preferred_alias”es from the previous tab, if any; “cell_set_alias_integrated” shows linkages between single species transcriptomics taxonomies and the integrated taxonomy; “cell_set_labels_CS191213#" columns indicate linkages between cell sets in the transcriptomics and other modalities within a single species;

337 “cell_set_descriptor” shows the type of cell set (or level of ontology); and “taxonomy_id” links to the
338 “taxonomy_id” tab. Finally, the “Cell class hierarchy” tab shows the ordered class, level2, and subclass
339 hierarchy and associated colors used as cell sets in previous tabs.
340
341 **Supplementary Table 4.** NS-Forest v2.1 was used to determine cell type cluster marker genes for all
342 annotated levels of the human primary motor cortex cell type taxonomy defined by RNA-seq (Cv3).
343 “clusterName” corresponds to the annotation label, either a cell type cluster name or a parent cell type
344 class in the taxonomy. “markerCount” gives the optimal number of marker genes in the set that best
345 discriminates the label. The “f-measure” column gives the f-beta score for classification using the set of
346 markers. The next four columns “True Negative”, “False Positive”, “False Negative”, “True Positive” give
347 the confusion matrix for the label given the set of markers. Finally, “Marker 1-5” lists the gene symbols
348 corresponding to the optimal set of markers.
349
350 **Supplementary Table 5.** NS-Forest v2.1 was used to determine cell type cluster marker genes for all
351 annotated levels of the mouse primary motor cortex cell type taxonomy defined by RNA-seq (Cv3).
352 “clusterName” corresponds to the annotation label, either a cell type cluster name or a parent cell type
353 class in the taxonomy. “markerCount” gives the optimal number of marker genes in the set that best
354 discriminates the label. The “f-measure” column gives the f-beta score for classification using the set of
355 markers. The next four columns “True Negative”, “False Positive”, “False Negative”, “True Positive” give
356 the confusion matrix for the label given the set of markers. Finally, “Marker 1-5” lists the gene symbols
357 corresponding to the optimal set of markers.
358
359 **Supplementary Table 6.** NS-Forest v2.1 was used to determine cell type cluster marker genes for all
360 annotated levels of the marmoset primary motor cortex cell type taxonomy defined by RNA-seq (Cv3).
361 “clusterName” corresponds to the annotation label, either a cell type cluster name or a parent cell type
362 class in the taxonomy. “markerCount” gives the optimal number of marker genes in the set that best

363 discriminates the label. The “f-measure” column gives the f-beta score for classification using the set of
364 markers. The next four columns “True Negative”, “False Positive”, “False Negative”, “True Positive” give
365 the confusion matrix for the label given the set of markers. Finally, “Marker 1-5” lists the gene symbols
366 corresponding to the optimal set of markers.
367
368 **Supplementary Table 7.** DEGs determined by ROC test between each GABAergic neuron subclass
369 and all other GABAergic nuclei within each species. Columns are labeled myAUC, which contains AUC
370 scores > 0.7; avg_diff, which contains difference in expression between target subclass and all other
371 GABAergic neurons; power; pct.1, which indicates the percent of nuclei that express the gene in the
372 target cluster; pct.2, which indicates the percent of non-target nuclei that express the gene; cluster,
373 which denotes the target cluster; gene, indicating the gene that was identified as DE; and species,
374 which indicates the species the test was performed in.
375
376 **Supplementary Table 8.** List of DEGs (from Supplementary Table 7) that is sorted according to the
377 order the genes appear within the heatmap.
378
379 **Supplementary Table 9.** Supervised MetaNeighbor results, within- and across-species. Each row
380 corresponds to a unique entry for a given gene set and a given cell class, either Glutamatergic or
381 GABAergic. The first five columns provide information about the gene sets, namely their provenance
382 (SynGO or HGNC); numerical IDs; descriptive labels; manual classifications for plotting and
383 interpretation; and finally the number of genes included in the analysis (after subsetting to genes with 1-
384 1 orthologs across all three species). The sixth column indicates cell class. The remaining columns
385 contain MetaNeighbor AUROCs for various analyses: within_species_meanROC (column 7) provides
386 the mean of within-mouse (column 8), within-marmoset (column 9) and within-human (column 10)
387 performance. For each species, tests were run with random 3-fold cross-validation, and the average

388 across folds is reported. Columns 11 and 12 contain results from cross-species analyses, detailed in
389 the methods. Results are sorted by their AUROC across primates (column 12).
390
391 **Supplementary Table 10.** DEGs determined by ROC test between each glutamatergic neuron
392 subclass and all other glutamatergic nuclei within each species. Columns are labeled myAUC, which
393 contains AUC scores > 0.7; avg_diff, which contains difference in expression between target subclass
394 and all other glutamatergic neurons; power; pct.1, which indicates the percent of nuclei that express the
395 gene in the target cluster; pct.2, which indicates the percent of non-target nuclei that express the gene;
396 cluster, which denotes the target cluster; gene, indicating the gene that was identified as DE; and
397 species, which indicates the species the test was performed in.
398
399 **Supplementary Table 11.** List of DEGs (from Supplementary Table 10) that is sorted according to the
400 order the genes appear within the heatmap.
401
402 **Supplementary Table 12**. Average expression of isoforms in human and mouse subclasses and
403 estimates of isoform genic proportions (P) based on the ratio of isoform to gene expression. Isoforms
404 were included if they had at least moderate expression (TPM > 10) and P > 0.2 in either human or
405 mouse and at least moderate gene expression (TPM > 10) in both species.
406
407 **Supplementary Table 13.** SNARE-Seq2 metadata, cluster annotations and quality statistics. Tab 14a
408 indicates SNARE-Seq2 experiment level metadata (experiment name, library, patient, species,
409 purification, age, sex) and mapping statistics for RNA (mean UMI detected, mean genes detected) and
410 AC (mean fraction of reads in promoters or FRiP, mean uniquely mapped fragments grouped by 5000
411 base pair chromosomal bins, mean unique fragment counts per final peak locations, total number of
412 final nuclei). Tab 14b indicates the SNARE-Seq2 local RNA clusters for human M1 generated using
413 Pagoda2 (local cluster, annotated cluster name, broad cell type and abbreviation, k value used for

414 Pagoda2 clustering, broad cell type markers, level 1 and level2 classes and associated markers,
415 unique cluster markers). Tabs 14c-d indicates SNARE-Seq2 consensus or harmonized RNA and AC-
416 Level cluster annotations for human and marmoset M1, respectively, including annotated cluster name,
417 cluster order, associated subclass and class, and the number of datasets making up the clusters. Tabs
418 14e-f lists all metadata outlined in tabs 14a-d for all SNARE-Seq2 cell barcodes from human and
419 marmoset M1 samples, respectively.
420
421 **Supplementary Table 14.** SNARE-Seq2 differentially accessible regions for human and marmoset M1.
422 Tabs 15a and 15b show SNARE-Seq2 differentially accessible regions (DARs, q value < 0.001, log-fold
423 change > 1) identified by AC-Level clusters (15a) or subclass level (15b) for human M1, indicating for
424 each chromosomal location the p value (hypergeometric test), q value (Benjamini-Hochberg adjusted p
425 value), log-fold change and associated cluster or subclass. Tab 15b shows subclass DARs (q value <
426 0.001, log-fold change > 1) for marmoset subclasses as in tab 15b. Tab 15d shows a summarization of
427 human and marmoset DARs detected by matched subclasses, indicating actual number of DARs
428 detected (tabs 15b and 15c) and the values normalized to cluster size and total number of DARs
429 detected per species.
430
431 **Supplementary Table 15.** Cis-co-accessible sites, TF motif enrichments and differential TFBS
432 activities for human and marmoset M1. Tab 16a (human M1) and 16b (marmoset M1) show cis-
433 coaccessible network (CCAN) sites for subclass distinct markers genes (Wilcoxon Rank Sum test,
434 adjusted P < 0.05, average log-fold change > 0.5). pct.1 indicates the percent of nuclei that express the
435 gene in the target cluster, pct.2 indicates the percent of non-target nuclei that express the gene. For
436 each cluster and marker gene, corresponding motif enrichment values (hypergeometric test) for gene-
437 associated CCAN sites are shown ("observed" indicates number of features containing the motif,
438 "background" indicates the total number of features from a random selection of 40000 features that
439 contain the motif), and the motif associated differential chromVAR activity values identified using

440 logistic regression. The full list of chromVAR differentially active TFBS activities are also provided. Tab
441 16c summarizes the number of CCAN-associated marker genes, associated TFBSs enriched and or
442 active by subclass for both human and marmoset M1. Tabs 16d and 16e show cis-co-accessible sites,
443 TFBS enrichments and differential activities by AC-level clusters for human and marmoset M1,
444 respectively, similar to that provided in tabs 16a and 16b. Tab 16f shows chromVAR differentially active
445 TFBS activities by consensus or harmonized cluster using logistic regression. Tabs 16g, 16h, and 16i
446 show cis-co-accessible sites, TF motif enrichments and differential TFBS activities for human,
447 marmoset and mouse M1 ChCs compared against BCs.
448
449 **Supplementary Table 16**. snmC-seq2 metadata. The table shows experiment level metadata,
450 including species, sample name, gender, purification information, experiment nuclei numbers and pass-
451 QC nuclei numbers.
452
453 **Supplementary Table 17**. Subclass TFBS enrichment results. TFBS enrichment analysis was done
454 with AME [78] using JASPAR2020 motifs . Within a species, hypo-methylated DMRs in each subclass
455 were tested against hypo-methylated DMRs of all the other subclasses (background). DMRs and 250bp
456 around regions were used in the analysis. This table includes p-values and effect sizes (log2(TP/FP)) of
457 the analysis results.
458
459 **Supplementary Table 18**. Subclass TFBS enrichment at TF cluster level. TFs in SI Tab 18 were
460 grouped using clusters defined in Ref [42]. The table lists the most significant p-values and the largest
461 effect size of each TF cluster group.
462
463 **Supplementary Table 19.** DEGs determined by ROC test between chandelier cells and basket cells
464 within each species. Columns are labeled as species, with true/false values indicating if a gene was
465 enriched in chandelier cells for that species.

466

467 **Supplementary Table 20.** DEGs determined by ROC test between L5 ET subclass and L5 IT subclass
468 within each species. Columns are labeled as species, with values of 1 indicating a gene was enriched
469 in the L5 ET subclass for that species. A value of 0 indicates that the gene was not enriched in the L5
470 ET subclass for that species.

471

472 **Supplementary Table 21.** Genes with expression enrichment in L5 ET versus L5 IT that decreases
473 with evolutionary distance from human (human > macaque > marmoset > mouse). Columns are labeled
474 by species, and values indicate the log-fold change between L5 ET and L5 IT for that species. Genes
475 were included if they had a minimum log-fold change equal to 0.5 in human.